The silica/water interface

Water-mineral interactions studied with surface-specific vibrational spectroscopy

Dissertation

zur Erlangung des Grades

“Doktor der Naturwissenschaften”

Im Promotionsfach Chemie

Am Fachbereich Chemie, Pharmazie und Geowissenschaften
der Johannes Gutenberg-Universität Mainz

Jan Schäfer

geb. in Weilburg

Mainz, 2019

1. Berichterstatter: Prof. Dr. Mischa Bonn
2. Berichterstatter: Prof. Dr. Thorsten Hoffmann

Tag der mündlichen Prüfung:

Contents

1 Introduction ... 1

1.1 Overview ... 1

1.2 Sum Frequency Generation Spectroscopy ... 2

1.2.1 Theoretical Background ... 3

1.2.2 Normalization and Local Field Correction ... 8

1.2.3 Experimental Setup ... 11

1.3 Non-linear Spectroscopy of the Silica/Water Interface ... 14

1.3.1 A Model Picture ... 15

1.3.2 Experimental Review ... 18

1.3.3 Summary of the pH- and electrolyte-concentration-dependent silica/water interface ... 31

1.3.4 Application to Chemistry ... 32

1.4 Outline of this Thesis ... 33

2 The O-H stretch vibrational coupling of surface water ... 35

2.1 Introduction ... 35

2.2 Results and Discussion ... 37

2.3 Conclusion ... 42

2.4 Further Experimental Details ... 43

2.4.1 Chemicals ... 43

2.4.2 SFG spectroscopy ... 43

2.4.3 Bulk IR and Raman measurements ... 43

2.4.4 Simulation Protocols ... 44

2.5 Additional Data ... 45

2.5.1 Decomposition of the instrumental response into bulk optical properties and surface-specific orientational effects ... 45

- 2.5.2 Smoothing procedure applied on SFG spectra 48
3 The vibrational response of water at a charged surface: screening and interference 49
- 3.1 Introduction....49
- 3.2 Results and Discussion 52
- 3.3 Conclusion....58
- 3.4 Further Experimental Details 59
  - 3.4.1 Spectroscopy....59
  - 3.4.2 Sample Preparation....59
- 3.5 Additional Data 60
  - 3.5.1 Normalized SFG spectra of water at the silica surface....60
  - 3.5.2 Expression for the potential, Debye length and wave-vector mismatch....60
  - 3.5.3 Uncertainty on the non-linear susceptibility ratio 61

4 Understanding dissolution processes from an interfacial perspective....63
- 4.1 Introduction....63
- 4.2 Results and Discussion 64
- 4.3 Conclusion....71
- 4.4 Further Experimental Details 72
  - 4.4.1 Sum Frequency Generation Spectroscopy 72
  - 4.4.2 Sample preparation 72
  - 4.4.3 Model 72
- 4.5 Additional Data 73
  - 4.5.1 Center of mass frequency shift along dissolution....73
  - 4.5.2 Conversion function between the SFG signal and interfacial ionic strength 73
  - 4.5.3 Time-dependent diffusion coefficient 74
  - 4.5.4 Dissolution kinetics at pH 9....75
  - 4.5.5 Time-dependent dissolution rate....75

4.5.6 Stability of the IR power 76
5 Specific ion-dependent crowding at a charged mineral/water interface 77
5.1 Introduction 77
5.2 Results and Discussion 78
5.3 Conclusion 84
5.4 Additional Data 85
5.4.1 Modified Poisson-Boltzmann model and SFG 85
5.4.2 The Gouy Chapman-based SFG model 87
Summary 91
Zusammenfassung 93
Acknowledgments 95
Bibliography 97

1 Introduction

1.1 Overview

Mineral/water interfaces are relevant for a wide range of geological and electrochemical problems. For example, the ability of water to dissolve and precipitate minerals, thus driving their distribution on earth through rivers and oceans is obvious. But even within the earth's crust that has long been considered as dry, the role of (interfacial) water to drive geological processes has recently been emphasized.[1] In this work, we study the physical properties of aqueous media at such a mineral surface and their role for mineral dissolution. To get microscopic-level insight, second-order non-linear spectroscopy techniques like Sum Frequency Generation (SFG) spectroscopy have increasingly been used due to their surface sensitivity. In this work, we focus on water in contact with silica, an abundant and prototypical mineral system which has been extensively studied with non-linear spectroscopy techniques since the early 1990s. A theoretical and experimental review on the progress of this field over the past 30 years is provided in chapter 1.3. The scientific contributions resulting from this work are summarized below:

(1) O-H stretch vibrations in H-bonded environments are often coupled. We demonstrate the presence of vibrational coupling in interfacial and bulk water, and disentangle intra- from intermolecular contributions to the corresponding vibrational spectra.

(2) The surface-sensitivity of SFG at charged interfaces varies substantially depending on the charge distribution in the near-surface region. We found that for silica/water, it can vary between almost monolayer sensitivity at very high and very low electrolyte concentration, while in the intermediate regime (~mM) SFG probes roughly 100 nm of water layers.

(3) By using this correlation, we have shown that SFG can be used to study dissolution kinetics from a direct interfacial perspective. We found that silica dissolves through an autocatalytic mechanism and generates roughly a millimole of charged dissolution products in the near-surface region within a timescale of a day. Comparing our results to corresponding bulk studies revealed that the dissolution process is diffusion-limited.

(4) We studied the ion-specificity of the interfacial charge distribution at the silica/water interface and the associated electrochemical properties such as the decay of the

surface potential. Our results show that surface charges are screened more efficiently with increasing ion size which has implications for the validity of traditionally used electric double layer models that assume point charges.

1.2 Sum Frequency Generation Spectroscopy

Sum Frequency Generation (SFG) is a 2nd order non-linear optical process, increasingly used as a non-invasive spectroscopy technique to study interfacial systems with a unique surface selectivity. It may provide detailed insight not only into the composition of interfaces but also the molecular interactions and resulting relative orientations.[2,3] In principle, SFG involves the interaction of two photons (of any frequency ω_1 and ω_2) with the sample that consequently emits a photon at the sum of the two frequencies $(\omega_3 = \omega_1 + \omega_2)$. In this work, we employed vibrational SFG spectroscopy (V-SFG) which requires one photon with a frequency in the infrared regime and the other one in the visible range. As sketched in Figure 1, the first photon (ω_{IR}) is used to vibrationally excite the sample, the second one (ω_{VIS}) upconverts it into a virtual electronic state which then emits at $\omega_{SFG} = \omega_{IR} + \omega_{VIS}$.

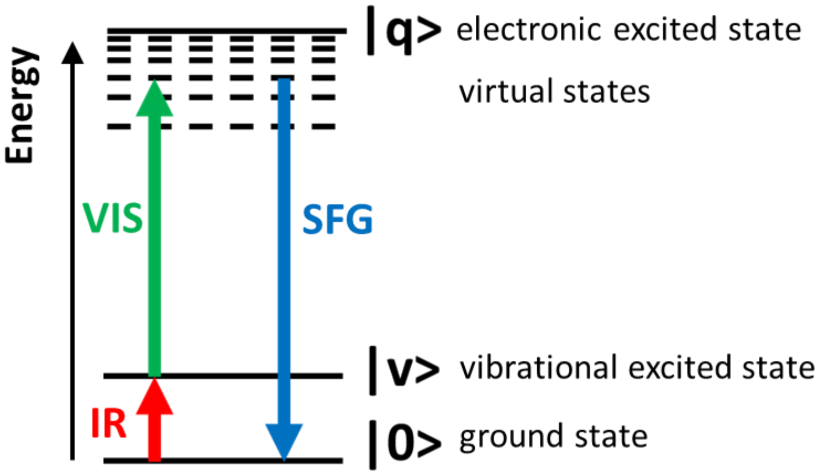

Figure 1: Energy diagram of the V-SFG process employing a broad band IR pulse (~450 cm^{-1}) and a comparably monochromatic VIS pulse (~20 cm^{-1})

This coherent optical process can be considered as a coupled IR-Anti-Stokes Raman transition that allows probing vibrational states of the system that are both IR and Raman active. The resulting SFG signal is enhanced, only if the IR frequency is in resonance with a vibrational state. In addition to the number of SFG active molecules, also their relative orientation determines the overall signal, since SFG is a 2nd order process. The responses of oppositely oriented molecules cancel each other out which gives rise to a net-zero signal for centro-symmetric media. In contrast, only at interfaces of such media, where centro-symmetry is broken, and a net orientation is present, the net SFG response is non-zero. Alternative versions of this method involving a variation of excitation energies $(\omega_1 + \omega_2)$ may be used to deduce additional information about interfacial systems by probing vibrationally and/or electronically off- and/or on-resonant. The most prominent example is Second Harmonic Generation (SHG) spectroscopy in which the excitation energies are equal $(\omega_1 = \omega_2)$ and commonly used as an off-resonant probe. The following section introduces SFG spectroscopy with a focus on V-SFG from both, a theoretical and experimental perspective. The theoretical part is based on the tutorial reviews by Wang[2] and Lambert[3] for the sake of simplicity assumes the electric dipole approximation, hence neglects multipole effects.

1.2.1 Theoretical Background

Light may interact with matter through oscillation of its associated electric field, distorting the molecular electron clouds. This distortion gives rise to an induced electric dipole of the molecules $\boldsymbol{\mu}$ which oscillate at the same frequency as the incoming electric field and in turn emit light at that frequency.

$$\boldsymbol{\mu} = \boldsymbol{\mu}_0 + \alpha \mathbf{E} \tag{1}$$

Here, $\boldsymbol{\mu}_0$ denotes the permanent (static) dipole and α the polarizability which contributes linearly with the imposed electric field $\mathbf{E}$. The overall polarization $\mathbf{P}$ of the material scales linearly with the macroscopic average of the molecular dipoles $\chi^{(1)}$ which, in the condensed phase, are additive.

$$\mathbf{P} = \varepsilon_0 \chi^{(1)} \mathbf{E} \tag{2}$$

$\chi^{(1)}$ is also known as the 1st order susceptibility and contributes to the macroscopic polarization together with the vacuum permittivity ε_0 and the electric field. As the light-induced electric field reaches strengths comparable to the internal molecular field, the polarization of the material becomes non-linear,

$$\mathbf{P} = \varepsilon_0 \left(\chi^{(1)}\mathbf{E} + \chi^{(2)}\mathbf{E}^2 + \chi^{(3)}\mathbf{E}^3 + \ldots \right) \tag{3}$$

with $\chi^{(2)}$ and $\chi^{(3)}$ being the 2nd and 3rd order non-linear susceptibilities which are substantially smaller than $\chi^{(1)}$ and require high field strengths as typically provided by pulsed laser beams to contribute significantly to the total polarization.

The SFG process involves simultaneous interaction with two photons and therefore relies on the second order non-linear susceptibility $\chi^{(2)}$. Invoking the time-dependence of the associated oscillating electric fields of frequency ω

$$\mathbf{E}(t) = \mathbf{E}_1 \cos \omega t \tag{4}$$

allows to derive the allowed SFG transitions. Since with SFG, we mostly consider interactions with photons of different energy, the time-dependence of the incoming field can be expressed as the sum of two independent electric fields.

$$\mathbf{E} = \mathbf{E}_2 \cos \omega_2 t + \mathbf{E}_2 \cos \omega_2 t \tag{5}$$

Recalling equation 2 for the optically induced polarization allows to rewrite the 2nd order contribution as

$$\mathbf{P}^{(2)} = \varepsilon_0 \chi^{(2)} \left[\mathbf{E}_1 \cos \omega_1 t + \mathbf{E}_2 \cos \omega_2 t \right]^2 \tag{6}$$

which can be rearranged to

$$\mathbf{P}^{(2)} = \frac{1}{2} \varepsilon_0 \chi^{(2)} \begin{bmatrix} \mathbf{E}_1^2 + \mathbf{E}_2^2 \\ +\mathbf{E}_1^2 \cos 2\omega_1 t + \mathbf{E}_2^2 \cos 2\omega_2 t \\ +2\mathbf{E}_1\mathbf{E}_2 \cos\left(\omega_1 + \omega_2\right) t + 2\mathbf{E}_1\mathbf{E}_2 \cos\left(\omega_1 - \omega_2\right) t \end{bmatrix} \tag{7}$$

and reveals that the response to two incident fields of different frequencies consists of two frequency-independent DC fields which act as constant bias polarization to the sample and four frequency-dependent transitions, sketched in Figure 2: Two Second Harmonic (SHG) transitions for each of the incident fields, one Sum Frequency (SFG) transition $\omega_1 + \omega_2$ and one Difference Frequency (DFG) transition $\omega_1 - \omega_2$.

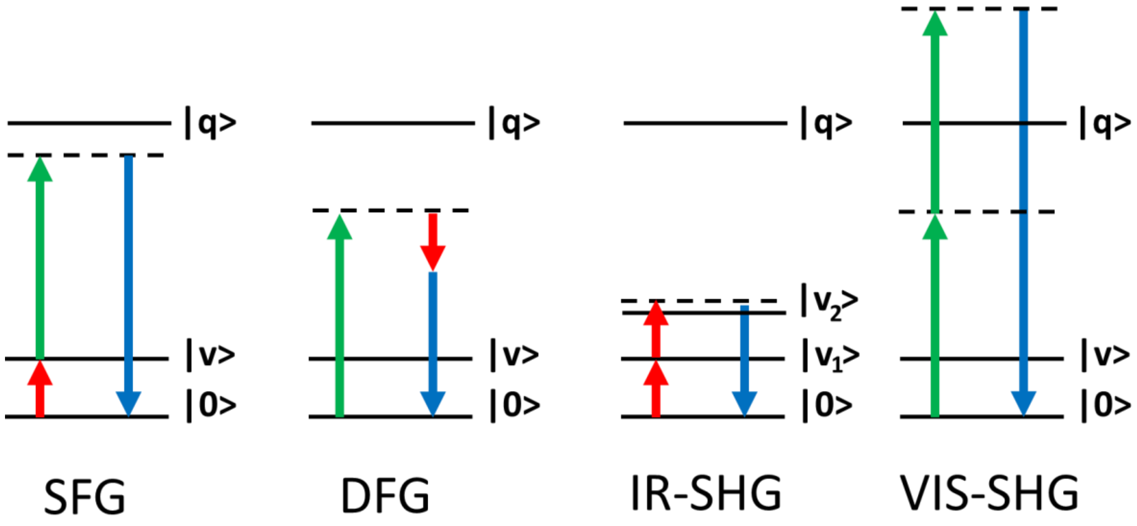

Figure 2: Energy diagram for all frequency-dependent components to the second-order polarization generated by two oscillating electric fields of infrared (red arrow) and visible (green arrow) frequency, respectively. The blue arrows denote the resulting SFG, DFG and SHG response, respectively.

Inserting the electric fields with visible and infrared frequency into the SFG contribution to the second order polarization given in equation 7 yields:

$$\mathbf{P}_{SFG}^{(2)} = \varepsilon_0 \chi^{(2)} \mathbf{E}_{VIS} \mathbf{E}_{IR} \cos\left(\omega_{VIS} + \omega_{IR}\right) t \qquad (8)$$

Physically, $\chi^{(2)}$ is a macroscopic property that indicates how susceptible the material is to interact with both incident electric fields, here of frequency ω_{VIS} and ω_{IR}. Mathematically, it can be expressed as a third rank tensor with 27 elements that relates the two electric field vectors $\mathbf{E}_{VIS}$ and $\mathbf{E}_{IR}$ to the generated vector $\mathbf{P}_{SFG}^{(2)}$. In cartesian coordinates, $\mathbf{P}_{SFG}^{(2)}$ can be expanded into all possible vector components of $\chi^{(2)}$

$$\mathbf{P}_{SFG}^{(2)} = \sum_{i}^{x,y,z} \mathbf{P}_{i,SFG}^{(2)} = \varepsilon_0 \sum_{i}^{x,y,z} \sum_{j}^{x,y,z} \sum_{k}^{x,y,z} \chi_{ijk}^{(2)} \mathbf{E}_{j,VIS} \mathbf{E}_{k,IR} \qquad (9)$$

which, if considering both bulk media to be isotropic, reduce to seven unique $\chi^{(2)}$ components for their interface. If the probed interface is symmetric about its surface normal (i.e. non-chiral, C_∞-symmetry) four of those seven elements are independent and may generate an SFG response:

$$\chi^{(2)}_{zxx}\left(\equiv \chi^{(2)}_{zyy}\right);\chi^{(2)}_{xzx}\left(\equiv \chi^{(2)}_{yzy}\right);\chi^{(2)}_{xxz}\left(\equiv \chi^{(2)}_{yyz}\right);\chi^{(2)}_{zzz} \tag{10}$$

Since SFG is a coherent process, the beam direction has to fulfill the phase matching condition which accounts for the conservation of momentum parallel to the interface of all beams as sketched in Figure 3a and given by:

$$n_{SF}k_{SF}\sin\theta_{SF} = n_{VIS}k_{VIS}\sin\theta_{VIS} + n_{IR}k_{IR}\sin\theta_{IR} \tag{11}$$

with *n* being the refractive index of the propagation medium at the corresponding frequency, *k*, the wavevector, given by the corresponding frequency divided by the speed of light, and *θ*, the beam angle relative to the surface normal. The polarization of electric fields may be uni-directional which is characterized to be p-polarized if it is parallel to the plane of incidence (x,z-directional) and s-polarized if it is perpendicular to that (y-directional). A simplified illustration is provided for an incident electric field in Figure 3c and d.

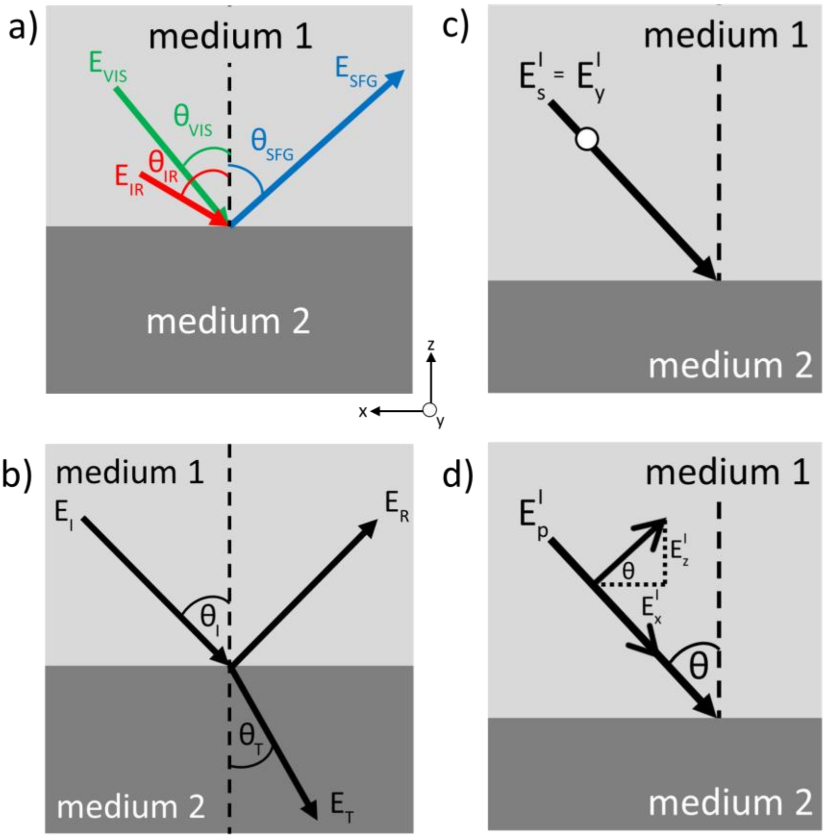
a)
medium 1
E_{VIS}
E_{SFG}
θ_{VIS}
θ_{SFG}
θ_{IR}
E_{IR}
medium 2
c)
medium 1
$E^{I}_{s} = E^{I}_{y}$
medium 2
z
x
y
b)
medium 1
E_{I}
E_{R}
θ_{I}
θ_{T}
medium 2
E_{T}
d)
medium 1
E^{I}_{p}
E^{I}_{z}
θ
E^{I}_{x}
θ
medium 2

Figure 3: SFG in reflection geometry at an interface. a) Angle of the emitted SFG beam as given by the phase matching condition. b) Reflected and transmitted component of the incident electric field c) and d) Polarization of incident electric fields: c) s-polarized, d) p-polarized.

Based on Figure 3c and d, the Cartesian components of the incident electric field can be expressed in terms of s- and p-polarization contributions as

$$\begin{aligned} \mathbf{E}_x^I &= -E_p^I \cos\theta_I \hat{x} \\ \mathbf{E}_y^I &= E_s^I \hat{y} \\ \mathbf{E}_z^I &= E_p^I \sin\theta_I \hat{z} \end{aligned} \tag{12}$$

with $\mathbf{E}_i^I$ representing the incident field in directional component *i* and θ_I the angle of that field with respect to the surface normal.

So far, we have exclusively invoked the reflection component of an electric field hitting the interface between two uniform media. However, light propagating from one medium into another is also partially transmitted as indicated in Figure 3b. The balance between reflection and transmission is given by the Fresnel coefficients. The coefficients for the reflective part are presented below.

$$\begin{aligned} r_p &= \frac{E_p^R}{E_p^I} = \frac{n_T \cos\theta_I - n_I \cos\theta_T}{n_I \cos\theta_T + n_T \cos\theta_I} \\ r_s &= \frac{E_s^R}{E_s^I} = \frac{n_I \cos\theta_I - n_T \cos\theta_T}{n_I \cos\theta_I + n_T \cos\theta_T} \end{aligned} \tag{13}$$

They depend on incident θ_I and transmissions θ_T angles (sketched in Figure 3b) as well as the refractive index of the two media denoted as n_I and n_T for medium 1 and 2, respectively. As a consequence, the magnitude of the incident field is modulated locally at the interface which can be expressed for each directional component as the sum of the corresponding incident and reflected field

$$\begin{aligned} E_x &= E_x^I + E_x^R = -E_p^I \cos\theta_I \left(1 - r_p\right) \equiv -K_x E_p^I \\ E_y &= E_y^I + E_y^R = E_s^I \left(1 + r_s\right) \equiv K_y E_s^I \\ E_z &= E_z^I + E_z^R = E_p^I \sin\theta_I \left(1 + r_p\right) \equiv K_z E_p^I \end{aligned} \tag{14}$$

with K_i denoting the non-linear SFG Fresnel factors for the incident field. The SFG polarization, induced in the material by that modified field, can now be re-written as:

$$\mathbf{P}^{(2)}_{i,SFG} = \varepsilon_0 \chi^{(2)}_{ijk}\, \hat{\mathrm{j}}\, K_j E^I_{p/s,VIS}\, \hat{\mathrm{k}}\, K_k E^I_{p/s,IR} \tag{15}$$

The frequency-dependent emission, resulting from that SFG polarization is also affected by the Fresnel factors, [4–7]

$$\mathbf{E}_{i,SFG} = K_i \mathbf{P}^{(2)}_{i,SFG} \tag{16}$$

Recalling equation 15-16 provides the full description of the SFG response with their directional components contributing as follows to the intensity of the emitted p- and s-polarized light:

$$\begin{aligned}
I_{s,SF} &\propto \left|\mathbf{E}_{y,SF}\right|^2 \\
&\propto \left|K_y \mathbf{P}^{(2)}_{y,SF}\right|^2 \\
&\propto \left|\varepsilon_0 K_y \sum_{j}^{x,y,z} \sum_{k}^{x,y,z} \chi^{(2)}_{yjk} K_j E^I_{s,VIS} K_k E^I_{s,IR}\right|^2 \\
I_{p,SF} &\propto \left|\mathbf{E}_{x,SF}\right|^2 + \left|\mathbf{E}_{z,SF}\right|^2 \\
&\propto \left|K_x \mathbf{P}^{(2)}_{x,SF}\right|^2 + \left|K_y \mathbf{P}^{(2)}_{y,SF}\right|^2 \\
&\propto \left|\varepsilon_0 K_x \sum_{j}^{x,y,z} \sum_{k}^{x,y,z} \chi^{(2)}_{xjk} K_j E^I_{p,VIS} K_k E^I_{p,IR}\right|^2 \\
&+ \left|\varepsilon_0 K_z \sum_{j}^{x,y,z} \sum_{k}^{x,y,z} \chi^{(2)}_{zjk} K_j E^I_{p,VIS} K_k E^I_{p,IR}\right|^2
\end{aligned} \tag{17}$$

1.2.2 Normalization and Local Field Correction

In order to deduce molecular-level information about interfaces from V-SFG spectra, an accurate determination of corresponding line shapes is crucial. However, compared to bulk-techniques it is much more challenging to achieve that for interfacial spectra. The current section summarizes how physically meaningful V-SFG spectra can be retrieved from recorded raw spectra and how to relate them to the interfacial structure.

As introduced in the previous section, V-SFG spectroscopy can be used to probe molecular vibrations in the form of a non-linear process that couples IR with Anti-Stokes Raman transitions. It relies on the second order susceptibility $\left(\chi^{(2)}\right)$ which is the macroscopic average of the first non-linear contribution to the molecular dipole (μ), which is called the first order hyperpolarizability (β).

$$\boldsymbol{\mu} = \boldsymbol{\mu}_0 + \alpha\mathbf{E} + \beta\mathbf{EE} \tag{18}$$

Intrinsically, $\chi^{(2)}$ is non-zero only for anisotropic systems, requiring a net dipole (i.e. preferential molecular order) as an additional symmetry selection rule. For most liquids, this can only be fulfilled at the surface which makes SFG sensitive to the first few molecular layers. $\chi^{(2)}$ is a third rank tensor with seven non-zero elements $\chi_{ijk}{}^{(2)}$ for azimuthally symmetry systems, arising from a permutation of lab frame axes (x, y and z). By varying the polarization and incident angle of the IR, VIS and SFG beams, different elements of the $\chi_{ijk}{}^{(2)}$ tensor can be interrogated. $\chi_{ijk}{}^{(2)}$ is connected to its molecular analog $\beta_{i'j'k'}$ by the number of contributing molecules (N) and their orientation defined by Euler angles ψ, θ and ϕ.[8] Accurate orientation distributions of surface molecules can be deduced using the Polarization Null Angle (PNA) method which involves tuning of polarization and incident beam angles. However, this requires a series of angular scans and the interpretation is not always trivial.[9]

Alternatively, molecular tensor elements $\beta_{i'j'k'}$ are, in principle accessible from bulk spectroscopic techniques as they are defined by the overlap integrals of the involved transition moments. Considering vibrational and electronic transitions to be decoupled, allows for construction of β by simple multiplication of bulk Raman (α) and IR (μ) spectra.[2,3]

$$\left|\chi_{ijk}{}^{(2)}\right|^2 \propto \left|N\sum_{i'j'k'}\left\langle\beta_{i'j'k'}\right\rangle_{\psi,\theta,\phi}\right|^2 \propto \left|\left\langle\alpha_{i'j'}\right\rangle\left\langle\mu_{k'}\right\rangle\right|^2 \cong \left|\left\langle\alpha_{i'j'}\right\rangle\right|^2\left|\left\langle\mu_{k'}\right\rangle\right|^2 \tag{19}$$

By comparison of those constructed spectra $\left|\left\langle\alpha_{i'j'}\right\rangle\left\langle\mu_{k'}\right\rangle\right|^2$ with the measured $\left|\chi_{ijk}{}^{(2)}\right|^2$, the relative weighting of the $\beta_{i'j'k'}$ transition moments due to their interfacial orientation can be deduced. At the same time, surface related changes of intermolecular structure can be accessed directly in terms of central frequencies and linewidths which requires accurate determination of $\left|\chi_{ijk}^{(2)}\right|^2$, or the imaginary part of $\chi_{ijk}^{(2)}$, $\mathrm{Im}\left(\chi_{ijk}^{(2)}\right)$, which allows for a direct comparison with $\langle\alpha_{i'j'}\rangle\langle\mu_{k'}\rangle$.

In this work, broadband femtosecond IR pulses were used for generation of the SFG electric field. In principle, such a system generates an SFG spectrum with a spectral window of ~450 cm^{-1} at each shot which are in practice accumulated in time. The detected spectrum which reports on $\left|\chi_{ijk}^{(2)}\right|^2$ thus not only depends on the vibrational properties of the probed material. It is also determined by the spectral shape of the incident IR pulse which is not uniform but shows a Gaussian intensity distribution that has to be corrected for by normalization. In order to determine the spectral shape of the IR beam at the interface, reference surfaces like z-cut quartz or gold coating can be used to measure the non-resonant SFG response.

An additional variability in SFG spectra stems from its modulation of the local electric fields (Fresnel factors) which depend on the beam angles, polarization and refractive indices of involved media. The frequency-dependent modulation of the IR field is elaborated in detail in refs. [4,7] and needs to be corrected for in order to extract molecular information $\chi_{ijk}^{(2)}$ from the V-SFG spectra. For ssp polarization combination, for example, the yyz tensor element is probed which is affected by the K_y and K_z Fresnel factors,[6]

$$\begin{aligned} K_y(\omega_i) &= \frac{2n_I(\omega_i)\cos\theta_i^T}{n_I(\omega_i)\cos\theta_i^T + n_T(\omega_i)\cos\theta_i^I} \\ K_z(\omega_i) &= \frac{2n_T(\omega_i)\cos\theta_i^T}{n_I(\omega_i)\cos\theta_i^I + n_T(\omega_i)\cos\theta_i^T}\left[\frac{n_I(\omega_i)}{n'(\omega_i)}\right]^2 \end{aligned} \tag{20}$$

with $\omega_i, \theta_i^I, \theta_i^T$, the frequency and incidence/transmittance angles of the corresponding beam, n_I, n_T, n', the refractive indices in the corresponding media. n' denotes the interfacial refractive index which is difficult to access and therefore often simplified as the bulk refractive index of medium 2 or 1 for the IR/VIS and SFG beams, respectively. A theoretical approximation to n' has been derived by Shen and coworkers.[5] The frequency-dependent part of the absolute-squared first order hyperpolarizability $\left|\chi_{yyz}^{(2)}\right|^2$, which is probed using s-polarized SFG, s-polarized VIS and p-polarized IR (ssp polarization combination), can thus be written as

$$\left|\chi_{yyz}^{(2)}\right|^2 \propto \frac{I(\omega_{SFG})}{I(\omega_{IR})\left|K_y(\omega_{SFG})K_y(\omega_{VIS})K_z(\omega_{IR})\right|^2} \tag{21}$$

However, $\chi_{yyz}^{(2)}$ is not necessarily purely resonant but may also contain a non-resonant background due to the electronic part of the SF transition.

$$\left|\chi_{yyz}^{(2)}\right|^2 = \left|\chi_{NR,yyz}^{(2)}(A_{NR},\phi_{NR}) + \sum_R \chi_{R,yyz}^{(2)}(A_R,\omega_R,\Gamma_R)\right|^2 \tag{22}$$

Depending on the proximity of the non-resonant transition to an electronic level, $\chi_R^{(2)}$ and $\chi_{NR}^{(2)}$ interfere with a different relative phase (ϕ_{NR}) which may cause spectral distortion of the SF resonances. Therefore, comparing homodyne SFG to bulk spectra directly may still be misleading for unknown systems since amplitude and relative phase of the non-resonant background may have a substantial impact and often remains unknown. For such cases, phase-resolved V-SFG an advanced version of this technique demonstrated first by the Shen group,[10] can be employed to reduce the non-resonant contribution and may provide further insight into the spectral details.

1.2.3 Experimental Setup

As noted in the previous sections, Vibrational Sum Frequency Generation, as a non-linear optical process, requires strong electric fields which involves pulsed laser beams of high power with spatial and temporal overlap at the sample. In order to generate the required infrared and visible laser beams, a Ti:sapphire regenerative amplifier (Solstice® Ace™ , Spectra Physics) is used to first generate pulses at λ≈800 nm, with ~40 fs duration and 1 kHz repetition rate. Roughly 1.7 mJ of that output is used to pump a commercial optical parametric amplifier (TOPAS Prime, Spectra Physics), together with a non-collinear difference frequency generation (NDFG) scheme which generates broadband (~450 cm^{-1})

infrared pulses with ~5 µJ. Further optical treatments of the corresponding beams in the SFG setup are illustrated in Figure 4 and summarized below.

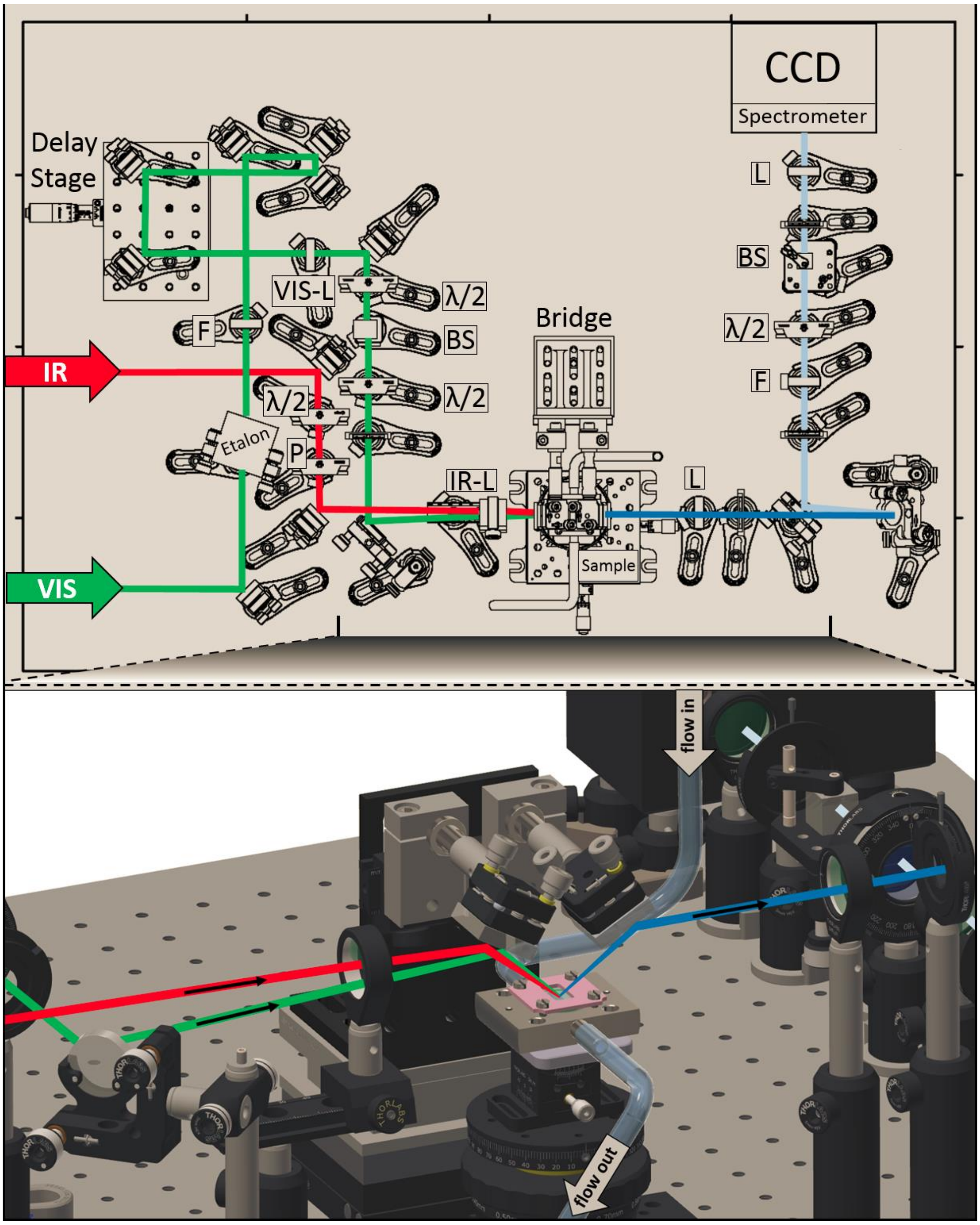
CCD
Spectrometer
Delay Stage
L
BS
λ/2
F
VIS-L
λ/2
F
BS
Bridge
IR
λ/2
λ/2
Etalon
P
IR-L
L
Sample
VIS
flow in
flow out

Figure 4: a) Schematic overview of the V-SFG setup with pathways of the IR (red), VIS (green) and SFG (blue) beams. Legend: P = Polarizer, L = Lens, BS = Cube Polarizing Beam Splitter, F = Filter, λ/2 = λ/2-plate, CCD = Charge-Coupled Device camera. The IR-lens is cut horizontally in order to guide the VIS beam as close as possible to the IR beam and overlap them at the sample. b) 3D rendering of the optical setup close to the sample stage, kindly provided by Marc-Jan van Zadel.

The infrared beam is separated from signal and idler spatially, residual signal and idler contributions are filtered out with a longpass filter (Spectrogon LP 2440 nm), omitted in Figure 4). The polarization of the infrared beam is controlled by a λ/2 plate (3000 nm, Altechna 2-IRPW-ZO-L/2-3000-C) together with a grid polarizer (Specac GS57501). Subsequently, the beam is focused on the sample using a lens with a focal length of 7.5 cm. This lens is cut horizontally in order to allow close alignment of the infrared and visible beam that yields spatial overlap at the sample. The visible beam is guided through a Fabry-Perot etalon (SLS Optics Ltd.), in order to spectrally narrow the upconverting pulse to a FWHM of ~20 cm^{-1} with ~20 μJ. The residual satellites are filtered out using an 800 nm bandpass filter (Semrock FF01-800/12). Additionally, the visible beam passes a delay stage for fine-tuning the temporal overlap between the two beams at the sample position. Afterward, it is focused by a lens with a 30 cm focal length and polarization-controlled with a cube polarizing beam splitter (780 nm, Eksma 430-0152) that is followed by a λ/2 plate (800 nm, Eksma 460-4215). An additional λ/2 plate is installed in front of the beam splitter in order to reduce the beam power if needed. Both beams hit the sample at incident angles of roughly 30° - 40°. The SFG signal is collimated (focal length = 15 cm) and subsequently filtered from potential visible reflections with two shortpass filters (775 nm, Semrock FF01-775/SP and 760 nm, Laser Components LC-760AGSP-25). For simplicity, only one is shown in the sketch of Figure 4. The polarization contributions of the SFG signal are separated by using a λ/2 plate (633 nm, Eksma 460-4225) together with a cube polarizing beam splitter (633 nm, Eksma 430-0154). The resulting SFG signal is focused by a lens with a 5 cm focal length before it is spectrally resolved by a spectrograph (Acton Spectro Pro® SP-2300, Princeton Instruments) and detected by an electron-multiplied charged-coupled device (emCCD) camera (ProEM 1600, Roper Scientific).

The sample cell depicted in Figure 4b is the one that was used in the experiments for the studies of the silica/water interface presented in chapter 3-5. It is made of stainless steel with a flow channel of Ø = 500 μm and with in- and outlets for a 4.8 mm tube that can be flushed with a peristaltic pump (Masterflex L/S 7523-80, Cole-Parmer®). On top, it is covered with a (parallel faced) fused silica window (Korth Kristalle GmbH Infrasil® 302, s/d: 60/40).

1.3 Non-linear Spectroscopy of the Silica/Water Interface

In this work, we aim at understanding the physical and chemical properties of mineral/water interfaces from a molecular level perspective. For doing so we study silica, one of the most abundant minerals on earth, with vibrational SFG spectroscopy. Surface-specific non-linear spectroscopy techniques, like SFG, have been extensively used over the past decades to study this system. A review of the theoretical and experimental progress is provided in this section.

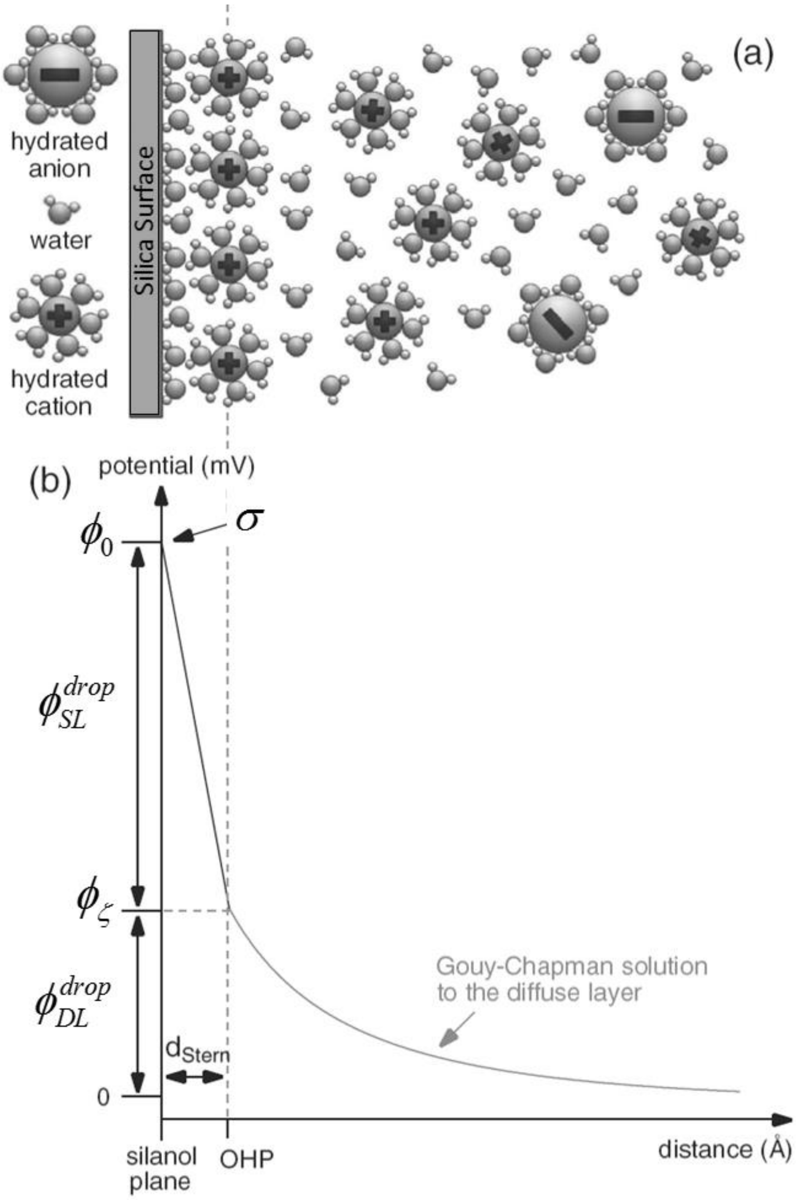
(a)
hydrated anion
water
hydrated cation
Silica Surface
(b)
potential (mV)
ϕ_0
σ
ϕ_{SL}^{drop}
ϕ_ζ
ϕ_{DL}^{drop}
d_{Stern}
0
Gouy-Chapman solution to the diffuse layer
silanol plane
OHP
distance (Å)

Figure 5: (a) Ion and water distribution of an aqueous electrolyte in front of a (negatively) charged surface. (b) The associated surface potential decay predicted by the Gouy-Chapman-Stern model of the electric double layer for such a system. Figure adapted from ref. [11].

In contact with water, silica, like most minerals, is known to be charged which gives rise to physical phenomena as the surface potential. As a consequence of the surface charge, the composition and structure of the water layers in proximity to this surface are different from that of bulk water. This interfacial region is referred to as the Electric Double Layer (EDL) which is commonly described by versions of the so-called Gouy-Chapman model, schematically presented in Figure 5. The nature of the EDL does not only determine the physical properties of the surface but also controls its reactivity. Therefore, microscopic insight is required to get a fundamental understanding of these physical and chemical phenomena on macroscopic scales. The advantage of employing non-linear spectroscopy compared to traditional methods like potentiometric titration is that it may access molecular-level information on the entire EDL, in contrast to single surface-representative observables like the zeta potential. Based on the traditional picture (GC model), the following section elaborates the molecular composition of EDLs, the resulting physical properties, and how they are reflected by non-linear spectroscopy.

1.3.1 A Model Picture

As introduced above, the surface of silica is charged which results from deprotonation of silanol groups upon contact with water. The water layers interacting with the surface charges or the electric field $\mathbf{E}_0$ associated with it, differ from bulk water and represent the EDL. The decay of the corresponding surface potential $\left(\phi_0\right)$, reports on two regimes of the EDL, namely the surface-close region, in which the potential drops linearly, similar to what is known for capacitors, and the more distant region that shows a gradual decay of the potential (Figure 5b). The surface-close part is often referred to as the Stern layer (SL)[12] or also Bonded Interfacial Layer (BIL)[13], depending on the definition. The outer region is called the Diffuse Layer (DL).

Roughly speaking, surface-close water may get reoriented by the surface field while with increasing distance, the water molecules preferentially get polarized. Both give rise to a broken centro-symmetry which is required for SFG-activity. Thus, the decay of the surface electric field, i.e. the thickness of the EDL, is related to the SFG intensity and determines the SFG probing depth for a charged interface. For taking the potentially long-ranging surface electric field $\mathbf{E}_0$ into account, the 2nd order optical description of 2nd order non-linear spectroscopy has to be extended. For doing so, an additional 3rd order term has been invoked to describe the decay of $\mathbf{E}_0$ with distance to the surface. The pioneering work in this field has been presented by Eisenthal and coworkers,[14] in which they deduced surface potentials (ϕ_0) of the silica/water interface from SHG intensities at different bulk pH conditions. For this purpose, they expressed the 2nd order non-linear response $\left(I_{\omega_1,\omega_2} \propto \left|\mathbf{E}_{\omega_1,\omega_2}\right|^2\right)$ of a charged surface as a sum of a 2nd (surface close) and 3rd order (distant) terms,

$$\mathbf{E}_{\omega_1,\omega_2} \propto \mathbf{P}^{(2)}_{\omega_1,\omega_2} = \chi^{(2)}\mathbf{E}_{\omega_1}\mathbf{E}_{\omega_2} + \chi^{(3)}\mathbf{E}_0\mathbf{E}_{\omega_1}\mathbf{E}_{\omega_2} \tag{23}$$

for which $\mathbf{E}_0$ can be rewritten as the bare surface potential ϕ_0 by assuming an isotropic field that is zero far away from the surface.

$$\mathbf{E}_0 = \int_0^\infty E_0(z)\,dz = \int_0^\infty \left(-\frac{d}{dz}\phi(z)\right)dz = \phi_0 \tag{24}$$

In this framework, the neat $\chi^{(2)}$ interfacial response results from the surface-close water layers which are reoriented by the surface charges, accounting for the SL. An additional third order term $\chi^{(3)}$ accounts for the more outer water layers (DL) that are reoriented and/or polarized due to interaction with the long persisting charge-induced surface-electric field $\mathbf{E}_0$.

Hore and coworkers presented an experimental work to disentangle those two contributions to the SFG response of water in front of a silica surface. By varying the ionic strength and thereby tuning the decaying length of $\mathbf{E}_0$, they were able to deduce the relative $\chi^{(2)}$ and $\chi^{(3)}$ contributions to the total SFG signal.[15] In the course of another SFG study of water in front of a charged fatty acid monolayer, Tian and coworkers realized that with increasing probing depth, the generated SFG light is decreasingly phase-matched which affects shape and intensity of the resulting spectrum.[13] Mathematically, this phase mismatch for SFG photons generated at different probing depths (z) was accounted for by considering the difference between the z-components of the corresponding wave vectors $(\mathbf{k}_i)$:

$$\Delta k_z = \left|\mathbf{k}_{VIS,z} + \mathbf{k}_{IR,z} - \mathbf{k}_{SFG,z}\right| = k_{VIS,z} + k_{IR,z} + k_{SFG,z} \tag{25}$$

with $k_{i,z} = {}^{\omega_i}\!\big/_{c}\,\sqrt{n(\omega_i)^2 - \sin(\theta_i)^2}$, related to the refractive indices and beam angles as introduced in section 1.2.

Using this scheme, Gonella et al. developed a general model to describe the second-order non-linear response of an aqueous solution with varying ionic strength in front of a surface with constant charge.[12] In the original model, they invoked the approximate solution of the Debye-Hückel theory to describe the decay of the surface potential that is associated with the surface electric field $\mathbf{E}_0$,

$$\phi(z) = \phi_0 e^{-\kappa z} \tag{26}$$

with κ^{-1} being the ionic-strength-dependent Debye length. As a consequence, κ^{-1} can be used to relate the ionic strength to the resulting SFG probing depth. In combination with the z-dependent phase mismatch introduced above, their proposed model predicts the variation of the non-linear response as a function of ionic strength:

$$\begin{aligned} I_{\omega_o} &\propto I_{\omega_1} I_{\omega_2} \left|\chi^{(2)} + \chi^{(3)} \int_0^{\infty} \left(-\frac{d}{dz}\phi(z)\right) e^{i\Delta k_z z} dz\right| \\ I_{\omega_0} &\propto I_{\omega_1} I_{\omega_2} \left|\chi^{(2)} + \chi^{(3)} \phi_0 \frac{\kappa}{\kappa - i\Delta k_z}\right|^2 \end{aligned} \tag{27}$$

The result is presented schematically in Figure 6, showing the SFG intensity (red) along with the underlying variation of the integrated surface potential (green) and the optical interference term (blue). The associated Debye screening lengths are presented in the upper axis. It predicts that at a given surface charge, the non-linear response increases with increasing screening length, i.e. decreasing ionic strength. However, at very low (sub-mM) ionic strengths, this trend is reversed due to increasing destructive interference of the emitted SFG/SHG light for Debye lengths exceeding 10s of nanometers. Experimental evidence for the applicability of this model is presented in chapter 3 of this thesis, also published as ref. [16].

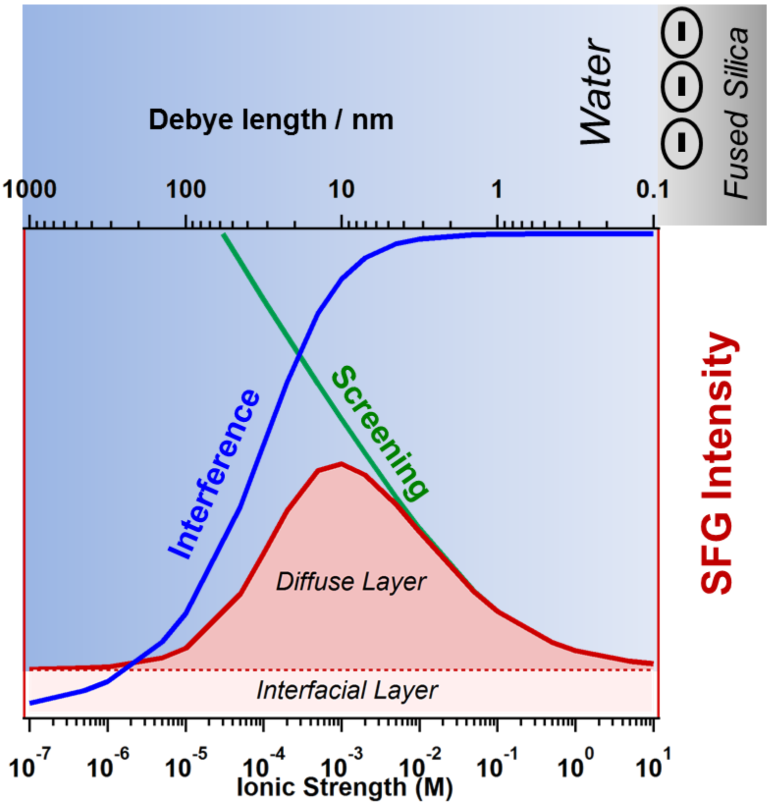

Figure 6: Theoretical SFG (SHG) response of a charged mineral surface in contact with water resulting from the model derived by Gonella et al.[12] Figure adapted from ref. [16].

1.3.2 Experimental Review

Experimentally, two strategies have been pursued to study the electric double layer of buried silica/water interfaces with non-linear spectroscopy:

(1) Tuning the ion concentration varies the screening of surface charges which alters the decaying length of the surface potential. Therefore, salt-dependent studies potentially provide insight into the charge distribution across the entire EDL and the surface potential decay associated with it. This approach has been used with both SFG[14–20] and SHG[21] methods.

(2) Trough varying the pH at fixed, rather high electrolyte concentration (> 0.1 M), the non-linear response is mostly sensitive to changes in the surface-close layers which may report on the surface charge density and associated surface potential either at the surface plane $\left(\phi_0\right)$ or at the outer Helmholtz plane $\left(\phi_\zeta\right)$, depending on the background electrolyte concentration. ([14,22–25], SHG and [26–29], SFG)

The following two sections present the recent progress from both strategies. In both, the type of non-linear spectroscopy employed as well as the optical geometry under which they are performed are important for the analysis of the reported results: While SHG is a non-resonant 2nd order process, non-selective to particular molecular or atomic species, SFG is aimed to probe specific vibrational resonances, here O-H stretch vibrations of water. This may give rise to different physical mechanisms underlying the corresponding non-linear responses. Additionally, the optical limit to the probing depth critically depends on the geometry of the involved beams. In steep angle (SA) reflection geometry, it is determined by absorption of the IR beam which, for the O-H stretch of water, results in penetration depths on the micrometer range. In evanescent wave (EW) geometry on the other hand, the optical fields are enhanced in the surface-close region but die off exponentially with distance from the surface. This gives rise to 10s of nanometers penetration depths which may be exceeded by the Debye length of the probed interface. As a result, EW-SFG is more surface-sensitive than the SA analog and changes the relative signal contributions from the individual layers in favor of the surface-close response.

1.3.2.1 Ion-dependence

The pioneering work in the field of non-linear spectroscopy of the silica/water interface was presented by Eisenthal and coworkers in 1993.[14] In this work, they studied the silica surface in contact with lithium and sodium chloride solutions using SHG spectroscopy under EW geometry. They observed that, independent of the cationic species, the SHG intensity decreases with increasing the ion concentration from 0.01 to 0.1 M. Since the SHG signal reflects the number of polarized and reoriented water molecules induced by the electric field, associated to the surface potential, this observation was opposite to what they expected based on the prior assumption that salt promotes silanol deprotonation and thus increases the silica surface charge. By contrast, the observed relation between ion concentration and SHG response was rationalized with the Gouy-Chapman equation for the surface potential $\left(\propto \sinh^{-1}\left(c^{-1/2}\right)\right)$ which predicts a decrease with increasing ion concentration, as detailed in chapter 3.

An SFG study by Chou and coworkers shows a similar trend for the O-H stretch vibrational response of aqueous alkali chloride solutions in ssp polarization combination. They interpreted the results as an ion-induced perturbation of the interfacial water network.[17] Based on the observed concentration sensitivity of the SFG signal in the order $K^+ > Li^+ > Na^+$, they concluded corresponding ion-dependent degrees of perturbation. Since this trend is not monotonic with ion size, they interpret this observation as a combination of two counteracting effects associated with the hydration radii of the different cations: Hydration water may replace interfacial water but also promote silanol dissociation which de- and increases the SFG response, respectively. Additionally, they realized that the SFG response consists of two spectroscopic features in the H-bonded O-H stretching region (at ~3200 cm^{-1} and ~3400 cm^{-1}). Independent of the salt species, the low-frequency band showed to be more affected by variation of the salt concentration. Based on α-quartz/water studies,[30–32] they argued that the low-frequency band is associated with water at (coupled) vicinal silanol groups that, when dissociated, generate a higher local surface charge density and therefore high SFG intensity. They conclude that both bands stem from the surface-close region but the stronger concentration dependency of the low-frequency band reflects preferential ion-induced perturbance of the areas of high surface charge density.

Next, Hore and coworkers performed an SFG study under EW geometry with NaCl solutions in ssp and sps polarization combination.[18] They found 2-3 features in the H-bonded O-H stretching region with different relative intensities for ssp and sps, respectively. They argued that with decreasing frequency, the O-H stretching band reflects more strongly H-bonded (i.e., higher coordinated) water molecules and more symmetric over asymmetric stretching modes. In support of previous work by Chou and coworkers,[17] they found that with increasing NaCl concentration, the overall SFG response and the ratio between low- and high-frequency band decreases. Add to this, the sps/ssp ratio of the two main features decreases as well. In contrast to the previous interpretation,[17] they concluded that two main species of interfacial water exist, one close to the interface and lower coordination and the other further away from the interface and being higher coordinated. They argued that with increasing salt concentration, the surface charge gets screened which results in a thinner surface layer accompanied by a relative reduction in the number of highly coordinated water further away from the surface. Based on the polarization ratios, they additionally concluded that with increasing concentration, the average tilt angle changes from 70° to 55°, thus from out-of-surface-plane towards interfacial alignment.

In 2011, Hore and coworkers performed additional SFG experiments of that system with a systematic approach in changing the ionic strength over a broad range from sub-mM up to the dissolution limit.[15] Similar to the previous results, they found an overall monotonically decreasing signal for increasing NaCl concentration. However, they were then able to distinguish between four different concentration regimes, which are presented in Figure 7 and briefly summarized below, together with the provided conclusion:

A) c < 0.5 mM: The SFG response is insensitive to the variation of the salt concentration: Ions may promote silanol deprotonation but also screen that charge from affecting the further distant water layers. This may give rise to a balance between an increase of the SL response $\left(\chi^{(2)}\right)$ and the decrease of the DL response $\left(\chi^{(3)}\right)$ at this low concentration.

B) 0.5 mM < c < 100 mM: The SFG signal decreases upon adding salt: The ions increasingly screen the surface charges which gives rise to a decreasing $\chi^{(3)}$ contribution.

C) 0.1 M < c < 1 M: A second plateau reflects the insensitivity of the SFG response towards increasing salt concentration which is interpreted as a $\chi^{(2)}$-dominated signal with both $\chi^{(2)}$ and $\chi^{(3)}$ contributions remaining constant. In the physical model, this regime represents the transition from the Gouy-Chapman to the Stern description of the interface.

D) c > 1 M: The SFG signal continues to decrease: In this high concentration regime, the interfacial H-bonding environment gets disturbed by the ions, inducing a less ordered interfacial water structure.

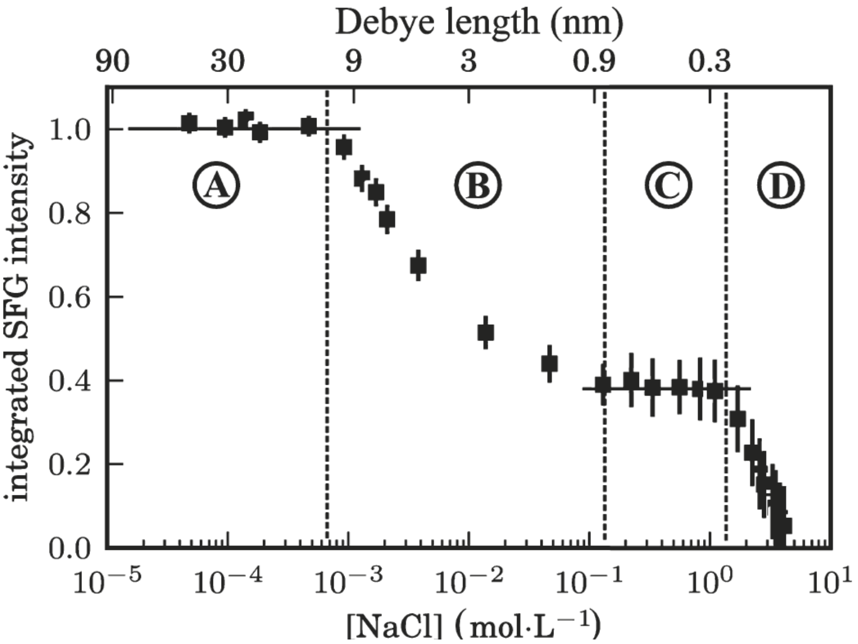

Figure 7: Integrated O-H stretch (ssp) SFG signal of the silica/water interface as a function of NaCl concentration. The top axis presents the theoretical Debye length, calculated based on the Gouy-Chapman model. Figure reprinted (adapted) with permission from ref. [15]. Copyright (2018) American Chemical Society.

Overall, this work highlights the role of the $\chi^{(3)}$ contribution to the non-linear response of water at charged interfaces. It shows that, depending on the salt concentration, the (long-ranging) field-induced reorientation and polarization of water may be dominating. On the basis of their findings, we present a follow-up study in chapter 3 of this thesis. It demonstrates that the SFG signal is not constant across regime A but, in contrast to regime B-D, decreases with decreasing salt concentration which becomes evident especially when using the SA geometry. This trend was predicted by Gonella and coworkers who elaborated a model that invokes charge screening and optical interference to determine the SFG response (detailed in chapter 1.3.1). In an SHG study under EW geometry by Eisenthal and coworkers, a similar trend was observed which was found to be independent of the polarization combination or the ion size.[21] However, to achieve decent agreement between their experiments and the model mentioned above, a drastic adjustment of the relative permittivity from 80 for bulk water to 30 for the diffuse layer was necessary. Additionally, further changes in the surface charge and / or Stern layer charge were also necessary.

In 2018, Tahara and coworkers performed phase-resolved measurements of the silica/water interface under high surface charge conditions (pH 12), in which they observed similar dependence on the ion concentration.[20] Additionally, they were able to disentangle the contribution form DL and SL water species to the overall ion-dependent SFG response. As illustrated in Figure 8, they observed that between 10 mM and 1 M NaCl the signal decreases with ionic strength and is saturated between 2 M and 5 M. As a consequence, they considered the difference spectrum between 10 mM and 1 M to represent the DL part and the high concentration spectra as the SL part. The DL spectrum consists of two broad features at around 3200 and 3400 cm^{-1}. Since the 3200 cm^{-1} part vanished upon isotopic dilution, which is an indicator for vibrational coupling, the DL response was characterized to be bulk-like. In contrast, the SL spectrum was insensitive to isotopic dilution which suggested water species that are not bulk-like. Furthermore, the SL spectrum consists of two features: One pronounced positive band at 3200 cm^{-1} indicating H-up orientation with strong H-bonds to the silica surface and one weak negative one at 3500 cm^{-1} suggesting H-down pointing with weak H-bonds. Based on that observation, they concluded that the topmost water layer oriented with one hydrogen binding to the surface and the other one pointing down towards the bulk water.

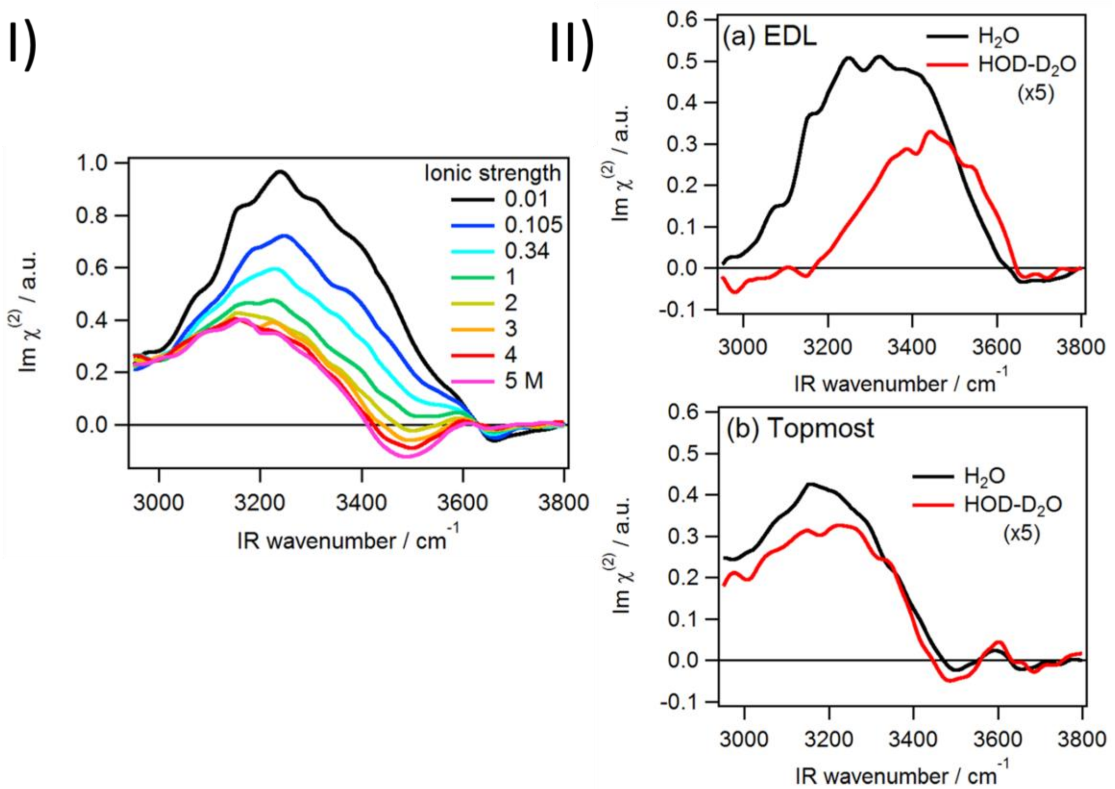

Figure 8: I) Phase-resolved SFG spectrum of silica/water at pH 12 as a function of salt concentration, II a) Difference spectrum between 0.01 M and 1 M for H_2O and isotopic diluted water, II b) 2 M spectrum with H_2O and isotopic diluted water; Figures reprinted (adapted) with permission from ref. [20]. Copyright (2018) American Chemical Society.

1.3.2.2 pH-dependence

The work presented by Eisenthal and coworkers in 1992 was also the first attempt to further the understanding of the acid/base chemistry of the silica/water interface using non-linear optical spectroscopy.[14] By employing SHG spectroscopy under EW geometry, they recorded a surface titration curve with 0.5 M NaCl background electrolyte. As depicted in Figure 9, they observe a monotonic increase of the SHG response with increasing pH from 2 to 14. The titration curve consists of two turning points at pH 4.5 and 8.5 for which the authors provide a two-site silica surface model with different acidity and predominant presence of the less acidic site (81%). The origin of the two sites is proposed to stem from different H-bonding environments of the two: The more acidic silanol species is considered to interact with water directly, i.e. pointing towards the solution. The less acidic species is thought to interact with another silanol group, i.e., lying in the surface plane. Elsewhere, these two species are also referred to as geminal and vicinal silanol groups, respectively.[25]

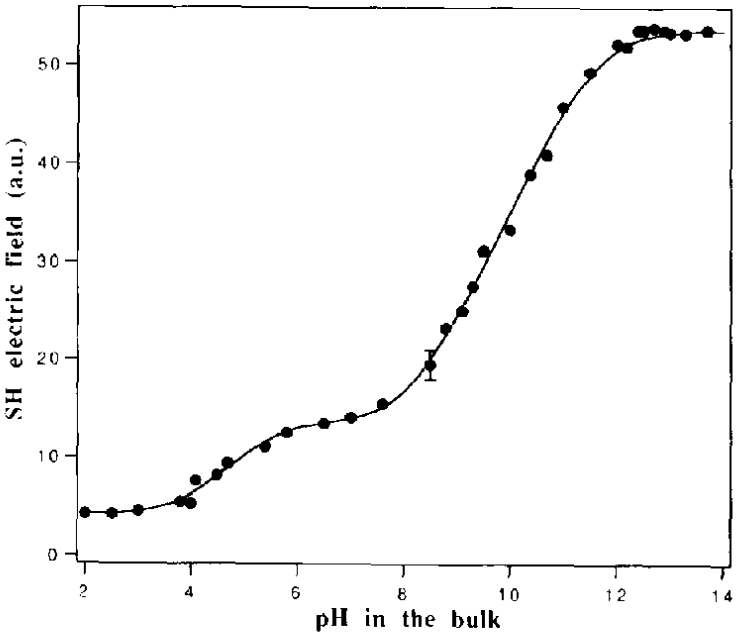

Figure 9: Variation of the SH electric field of the silica/water interface with changing bulk pH at constant electrolyte concentration (c(NaCl) = 0.5 M), Figure reprinted from ref. [14], Copyright (2018), with permission from Elsevier.

Based on calculations of the surface potential using the Gouy-Chapman model, which assumes low electrolyte concentration, the $\chi^{(3)}$ term was deduced and used to infer the pH dependence of the surface potential at high concentration where Gouy-Chapman actually is not valid. The result suggested that with 0.5 M salt, the maximal surface potential for silica/water is 140 mV at pH 12.

2004, Shen and coworkers performed the first pH-dependent SFG study of the silica/water interface by measuring the O-H stretch vibrational response under SA geometry.[31] For all spectra, they observed two broad-band features at around 3200 cm^{-1} and 3400 cm^{-1} for more and less strongly H-bonded water, respectively. However, they realized that compared to α-quartz, the low-frequency band of fused silica appeared broader and shifted to slightly higher frequencies, suggesting that water at crystalline surfaces is more structured. For tuning the pH between 1.5 and 11 without adding any background electrolyte they observed an overall monotonic increase of the SFG signal with increasing pH which is in line with previous SHG results by the Eisenthal group.[14] However, they observed that the intensity of the low-frequency band varies with pH in a manner similar to that of the SHG signal, while the high-frequency feature hardly shows any pH-sensitivity at all.

A whole series of pH-dependent studies of silica/water was performed by the Gibbs group, starting with work from 2012,[22] that presents pH scans with SHG under EW geometry under s-in/all-out polarization combination. In this work, they studied the impact of the cation size on the pH-dependence by using 0.5 M of 4 different alkali salts as background electrolytes. For all alkali salts, they observed a bimodal titration curve as presented by the Eisenthal group.[14] However, the inflection point for the high pK_a species varied substantially depending on the chosen salt (from 8.3 (NaCl) to 10.8 (LiCl), see Figure 10) which suggested that the stability of the less acidic silanol groups depend on the local ion identity. Also, the relative ratio of the two silanol species also seemed to depend on the salt: From the 20/80 ratio under NaCl electrolyte that has been proposed in the Eisenthal work presented above, the relative abundance of the more acidic site can increase to 60% by using LiCl instead. Since the ion-specific surface acidity does not scale with the ionic radius but increases in the series of $Na^+ < K^+ < Cs^+ < Li^+$, they concluded that several effects contribute.

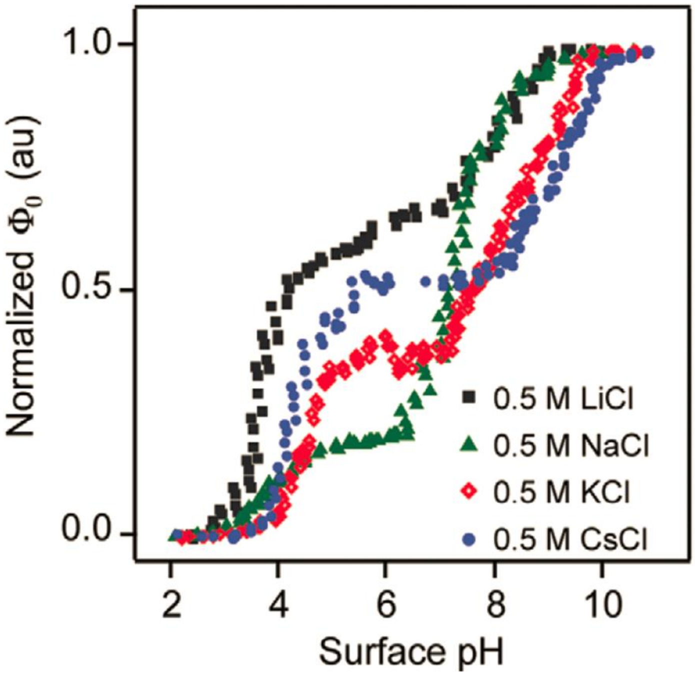

Figure 10: pH-dependent surface potential of silica/water deduced from SHG titration experiments using 0.5 M of different alkali chlorides, Figure reprinted (adapted) with permission from ref. [24]. DOI: https://doi.org/10.1088/0953-8984/26/24/244107, © IOP Publishing. Reproduced with permission. All rights reserved.

After all, cations may perturb the interfacial water structure and/or stabilize siloxide which is why all interactions, i.e. ion-surface, ion-water and water-surface have to be regarded:

(1) Small, hard ions such as Cs^+ interact more strongly with (i.e. stabilize) the hard siloxide
(2) More hydration leads to more acidic sites, which holds true except for Na^+
(3) Matching water affinities can lead to shared hydration shell ion paring which in this case means that Na^+ and siloxide match better than Li^+ and siloxide

Next, they studied the impact of different halides anions on the pH-dependence by employing the same experimental conditions.[23] They observed that with increasing halide size:

(1) The pK_A of the more acidic silanol species shifts to lower pH and that of the less acidic ones shifts to higher pH.
(2) The titration curve gets sharper which suggests increasing positive cooperativity between the larger (less hydrated) halides together with the cation and the surface: They concluded that large anions promote deprotonation of the more acidic species through acid-base coupling between silanol neighbors.
(3) The fraction of acidic sites increases (20% to 86% for sodium halides and 45% to 91% for potassium halides) which means an increase of the surface charge at neutral pH.
(4) The effective acidity of the less acidic sites decreases, suggesting that a high surface charge makes it more difficult for the less acidic sites to deprotonate.

Additionally, they concluded that the less acidic silanol sites show negative cooperativity: The more of this species is present at the surface, the more deprotonation of one silanol group inhibits deprotonation of the next one.

A complementary SFG experiment of this work interrogated the pH dependence of the O-H stretch vibrational response with 0.5 M NaI background electrolyte. Under ppp polarization combination and EW geometry, they observed an intensity increase not only from neutral to high pH but also from neutral to low pH which differs from all the SHG results reported about this system. They concluded that the cooperative structure between the surface, the cation and the anion that stabilizes one silanol species dissociated and the other protonated at neutral pH, displaces more interfacial water molecules than the structures formed at low or high pH which gives rise to a minimum in the SFG signal. Without providing an interpretation, they noted that they found a ~30-40-fold decrease of the SFG response from pure water to 0.5 M NaI, much higher than reported by the Hore group for

NaCl (in ssp)[15] and opposite to their own findings employing SHG which showed a 2.5-fold increase.

In another work, the same group studied the impact of salt concentration on the previously discussed cation- and anion-specific effects by comparing 0.5 M with 0.1 M solutions.[24] They observed that the cation-specific effects essentially vanish upon dilution to 0.1 M while the anion-induced changes in pH-dependence remain almost unaffected by dilution. They concluded that the alkali chlorides, except for NaCl, stabilize the less acidic silanol species in the protonated form which stems from surface-water-electrolyte interactions. This cation-specific interfacial distribution becomes more similar for different alkali chlorides at a lower concentration. The halide-surface structure, on the other hand, seems to be so stable for the large anions that it already forms at 0.1 M.

Next, they reported a work which demonstrates that silica undergoes substantial hysteresis.[25] By titrating from different starting pHs, they observed that the titration curve may show 2 or 3 inflection points which indicates the presence of 3 differently acidic silanol sites with changing relative abundance depending on the surface history. They further argued that the acidity is related to different H-bonding environments of the protonated silanol with increasing acidity in the series:

(1) Isolated (hydrophobic) species
(2) Geminal species that interact with water
(3) Vicinal species that interact with neighboring silanols

With 10 mM NaCl background electrolyte and using a under p-in/all-out polarization combination, they deduced pK_a values of 3.8, 5.2 and ~9 which are all present if the starting pH was 12, while from pH 7 species (1) + (3) and from pH 2 species (2) + (3) were present. The presence of hydrophobic silanol groups was later supported by an SFG work reporting an additional free-O-H stretching band at roughly 3750 cm^{-1} that was even enhanced when pre-treating the silica surface with heat.[33] However, the interpretation of this free-O-H band was questioned in a follow-up study involving phase-resolved experiments that pointed to the presence of a hydrophobic water species, instead.[34]

In 2013, Borguet and coworkers presented work studying the salt sensitivity of the SFG response over the pH range of 2 to 12.[26] Under ssp polarization combination and EW geometry, they found that upon adding 0.1 M NaCl to pure water, the SFG response changes most dramatically around neutral pH while it is mostly insensitive to the addition of salt at low and high pH: With salt they observed a monotonic increase of the SFG signal from pH 2 to pH 12. Without adding salt however, they found a maximal response at around pH 8. The provided interpretation suggested that the interfacial water is most structured at neutral pH. Please note that in this study the ionic strength of the pure water system is not kept constant across the investigated pH-window which varies between 10^{-7} for neutral and 10^{-2} for pH 2 or 12. Therefore, the Debye lengths of “pure water” and 0.1 M NaCl vary dramatically around neutral pH but get very similar for low and high pH which may distort the actual ratio of the compared systems.

In 2016, Chou and coworkers presented an SFG study with ssp polarization combination, using neutral pH solutions of high ionic strengths (6 and 12) of different chloride solutions, namely NaCl, LiCl, $MgCl_2$, $CaCl_2$.[19] They found that divalent ions show a single low intensity, high-frequency water band at around ~3500 cm^{-1} suggesting that for these salts the interfacial water order is almost lost. They conclude that in contrast to alkali ions, the local electric field of divalent ions is strong enough to polarize, reorient or displace water interacting with the surface silanol groups.

2016, Tahara and coworkers presented a phase-resolved SFG study on the silica/water interface under neutral (pH 7.2), acidic (pH 2.1) and basic (pH 12.1) conditions.[27]

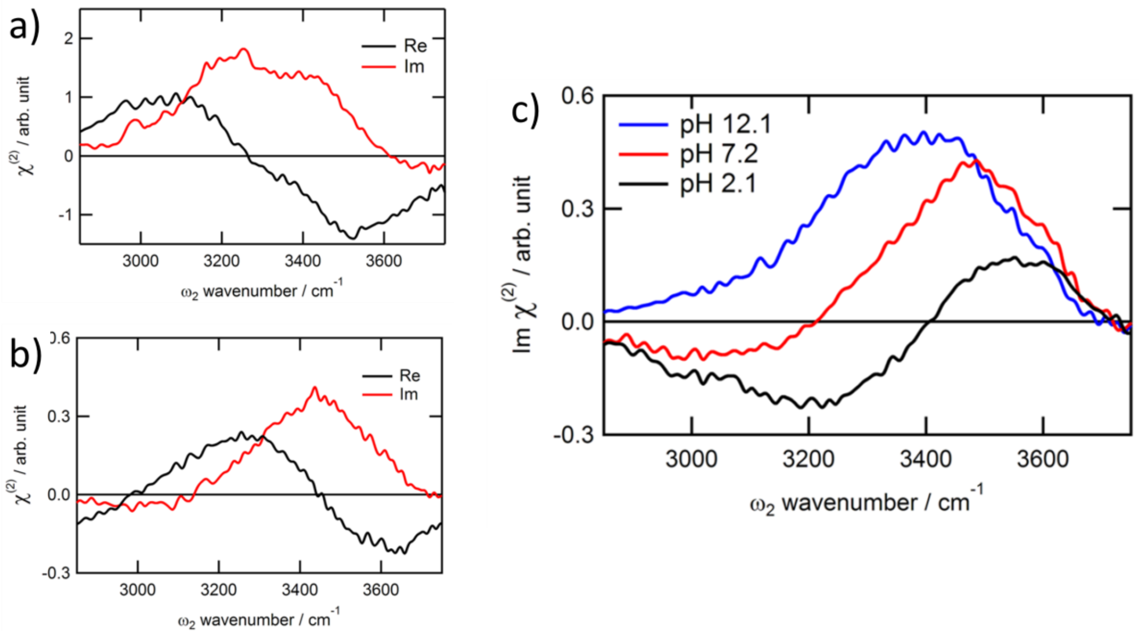

Figure 11: Phase-resolved SFG spectra of silica/water with 10 mM background electrolyte, (a) for H_2O at neutral pH, (b) for isotopically diluted water at neutral pH and (c) for isotopically diluted water at three different pH conditions. Figures reprinted (adapted) with permission from ref. [27]. Copyright (2018) American Chemical Society.

As shown in Figure 11, they observed that at neutral pH and 10 mM background electrolyte, the low-frequency part of the prominent O-H stretch double feature disappears upon isotopic dilution. Therefore, they concluded that the 3200 cm^{-1} band, known to be the salt-sensitive part (in ssp), is largely caused by intra- and/or intermolecular vibrational coupling. They further noticed that the uncoupled spectrum still varies in shape and intensity with pH, owing to positive and negative contributions at high and low frequency, respectively. The low-frequency part appeared to be negative at low pH, positive at high pH and with a negligible contribution at neutral pH. These contributions are interpreted as a convolution of 3 different water species:

(1) H-up, bonded to the siloxide
(2) H-up, bonded to the silanol oxygen
(3) H-down, bonded to the DL water

According to their interpretation, tuning the pH from basic to acidic conditions increases the number of species 2 and 3 present at the interface. They noted that in particular the spectral component of species 3 shows a broad continuum of strong H-bonds.

In 2017, the Gibbs group presented two related SFG studies on the silica/water interface. The first one compared the pH dependence of the SFG response under ssp vs. pss polarization combination, reproduced in Figure 12.[28] For pss, they observed a monotonic signal increase with increasing pH, very similar to what is known from SHG studies of the same system. Based on this finding they concluded that pss is more surface-sensitive and provides direct insight into the SL which appears to be more ordered with increasing pH. In contrast, the SFG intensity measured using ssp experiments shows a minimum signal at neutral pH and an increase when tuning to more basic or acidic conditions. This trend got even more pronounced when increasing the background electrolyte (NaCl) from 10 to 100 mM. They concluded that ssp provides a larger probing depth than pss and reports on the more outer water layers that in contrast to the topmost waters seem to flip around neutral pH. They rationalized the findings with two possible scenarios, both being in line with the net water flip observed with phase resolved SFG by Tahara.[27] One scenario considers a pH-induced distortion of the SL hydration shells, the other considers EDL overcharging at low pH which usually is only expected to occur for multivalent ions.

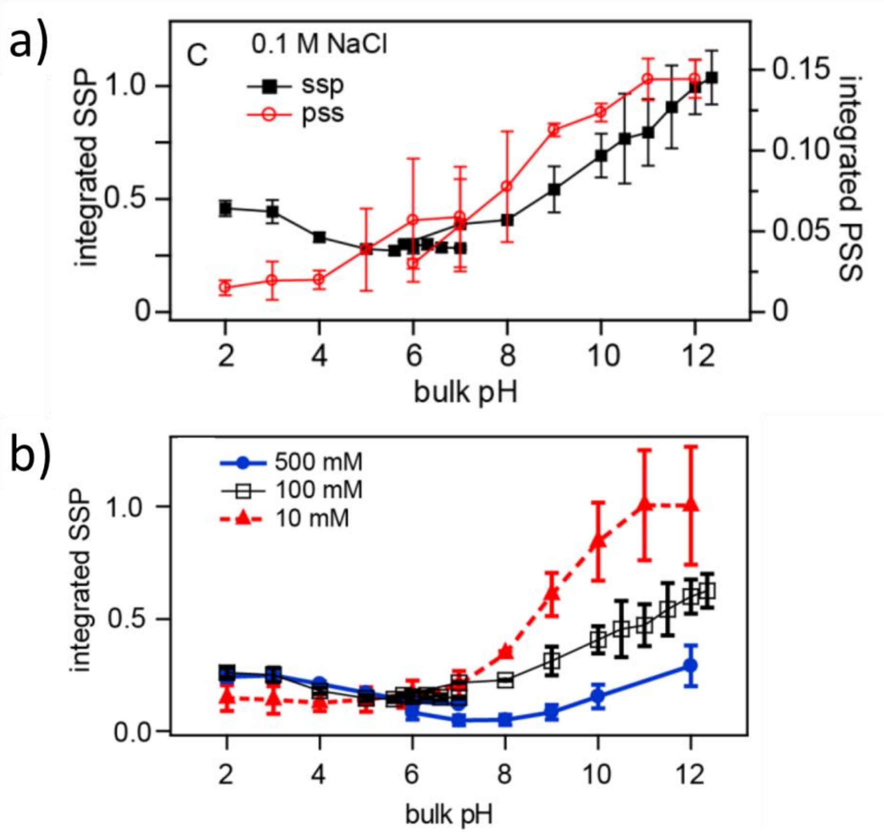

Figure 12: Integrated O-H stretch SFG signal (EW geometry) as a function of pH. a) ssp vs pss polarization combination in the presence of 100 mM background electrolyte (NaCl), b) ssp polarization combination at three different background concentrations of electrolyte. Figures reprinted (adapted) with permission from ref. [28]. Copyright (2018) American Chemical Society.

In the second work, they tested this non-monotonic pH-dependence of the SFG response with respect to the cation species of highly concentrated electrolyte solution (500 mM).[29] At neutral pH, hence the minimum of the titration curve, they observe slight differences in the signal intensity in the series $Cs^+ < K^+ < Na^+ < Li^+$, interpreted to report on the surface propensities increasing with $Li^+ < Na^+ < K^+ < Cs^+$. At low and high pH, they observed inversion of this series from which they conclude that the EDL model is only valid for a narrow range around neutral pH. For high pH, they reason that the cation adsorption is mediated by hydration water which may result in the expulsion of Cs^+ ions but specific adsorption of hydrated Li^+. The inversion at low pH is attributed to a combination of EDL overcharging and asymmetric dehydration.

1.3.3 Summary of the pH- and electrolyte-concentration-dependent silica/water interface

The previously reviewed studies demonstrated that the non-linear response of silica/water is sensitive towards changes in the interfacial charge distribution. By adjusting the experimental conditions, it has thus been used as a reporter of both, the effective surface charge as well as the local concentration of ions that screen these charges. The O-H stretch vibrational response of water in front of a silica surface has been shown to consist of the typical double band, peaked at around 3200 and 3400 cm^{-1},[15,17–19,26,28,29,31] that is also known from bulk water[35] and the air/water interface,[36]. As indicated by isotopic dilution experiments, the low-frequency part of this band is substantially affected by vibrational coupling.[20,27]

Based on the concentration-dependent studies, following consistent conclusions have been drawn: In general, the non-linear response increases with decreasing salt content of the solution,[12,14–17,20,21,37] which can be assigned to a concentration-dependent decaying length of the surface potential, qualitatively understood with the Gouy-Chapman theory of interfaces.[12,14–16,20,21,37] The concentration-dependence of the non-linear response seems not only to be affected by the ion valence but also its size.[16,17] At very low salt content (sub-mM), the non-linear response has an inverse concentration-dependence, i.e. decreasing signal with further decreasing concentration. This has been assigned to optical interference which contributes to the signal for probing depths larger than 10s of nanometers.[12,16,21] Under EW geometry, the relative contribution of surface close-layers to the total non-linear response is increased compared to SA geometry. This is evidenced by comparably high signals at high ionic strength, and the impact of interference shifted to lower concentration.[15,16,21] The low-frequency part of the O-H stretch SFG band is more sensitive to the variation of salt concentration and is thus preferentially resulting from the field-induced contribution $\left(\chi^{(3)}\right)$,[15–17,20,37] reporting on the more distant water layers.[15,16,20,37] At high salt concentration ($c \geq 0.1$ M), the spectral weight of the band shifts to lower frequencies, independent of the salt species,[16,17] and is less affected by vibrational coupling.[20]

The following findings are based on the pH-dependent studies: The non-linear response of silica/water is lowest at pH 2 and increases monotonically upon increasing the pH, interpreted as a corresponding increase of the surface charge.[14,22–25,31] Depending on the cation and anion species, the concentration and the titration direction, the titration curve shows 2 or 3 inflection points at different pH values. This is interpreted to reflect the presence and ratio of different types of surface silanol groups contributing with acidity to the overall surface charge.[14,22–25] More precisely, it was concluded that there are isolated, geminal and vicinal species with pK_a values that increase in this order.[25] The SFG studies provided further insight and demonstrated that the interfacial water structure is more complex than assumed based on the SHG results.[19,23,26–29,31,38] In contrast to SHG, the pH-dependent trend of the (ssp) SFG response is not monotonic in the presence of salt but shows a minimum around neutral to slightly acidic pH.[28,29,38] This suggests a net water flip at this pH range which was supported by phase-resolved SFG results.[27] Possible scenarios giving rise to this flip are a pH-induced distortion of SL hydration shells, EDL overcharging,[28,29,38] and different types of water present at the surface.[27] The SFG response in pss polarization combination shows a monotonic trend,[28] similar to what is observed in SHG studies with the analogical polarization combination, s-in/all-out. [22–25] In pss polarization combination, the spectral weight of the O-H stretch response of silica/water is more on the high-frequency band compared to ssp.[28] Together with the found pH-dependent trends, it was concluded that the two polarization combinations are sensitive to different types of water, probably at different distance to the surface.[28,29,38]

1.3.4 Application to Chemistry

As discussed above, non-linear spectroscopy techniques have provided copious studies with in-depth insight into the electrochemical and acid-base properties of the silica/water interface. Yet only a few works have started to focus on the kinetic behavior of these interfaces which ultimately determines the chemistry of these kinds of systems. In 2008, Geiger and coworkers reported an SFG work in EW geometry, where they temporally resolved the pH titration of silica/water in the presence of 10-500 mM of salt.[39] They found that the surface lags spatially and temporally the bulk pH, which, in case of the temporal delay, increased with increasing ionic strength and halide polarizability up to 4.5 h. Another study by the Bonn group highlighted the effect of flow on the silica/water interface which seemed to reversibly alter the balance between the dissolution of silica and deprotonation surface silanol groups.[40] Under neutral conditions and 10 mM background electrolyte, they observed a drop of the SFG intensity upon flow which recovered on a timescale of 30 minutes. They assigned this drop to a lowering in the effective surface charge resulting from a fast hydrolysis reaction of silica compared to slower deprotonation of the silanol groups under these conditions. As a follow-up of that work, chapter 4 of this thesis aims at quantifying the dissolution products accumulating at the silica surface and understanding the kinetics behind it.

1.4 Outline of this Thesis

The current section summarizes the scientific contributions resulting from the experimental and theoretical studies performed in this work. It has been realized that the spectral response of water in front of a silica surface is substantially affected by vibrational coupling.[20,27] In chapter 2 we try to disentangle possible inter- from intra-molecular coupling mechanisms of bulk and surface water in general. This work was published in *The Journal of Physical Chemistry Letters*. In chapter 3, we present how the O-H stretch vibrational response of the silica/water interface depends on the ionic strength of the aqueous medium. This work elaborates the relation between interfacial charge distribution and surface specificity of SFG and was published in *Physical Chemistry Chemical Physics*. In chapter 4, we use this relation to study the dissolution kinetics of silica in water and provide a possible underlying mechanism, insights that are not accessible by bulk techniques. This work showed that SFG spectroscopy can be used to study interfacial reactions directly and was published in *Nature Communications*. In chapter 5, we address the question of how unique the charge distribution of monovalent ions is at the silica/water interface and what implications this has for interfacial water structure as well as surface potential, commonly described by invoking point charge models. This manuscript is under preparation.

2 The O-H stretch vibrational coupling of surface water

Copyright: Reprinted (adapted) with permission from Jan Schaefer, Ellen H. G. Backus, Yuki Nagata, and Mischa Bonn 2016. Both Inter- and Intra-molecular Coupling of O-H Groups Determine the Vibrational Response of the Water / Air Interface. *The Journal of Physical Chemistry Letters.* Copyright 2016 American Chemical Society

Acknowledgment: The molecular dynamics simulations in this work were performed and analyzed by Dr. Yuki Nagata. My contribution to this work was the acquisition and analysis of SFG data.

2.1 Introduction

Vibrational coupling is relevant not only for dissipation of excess energy after chemical reactions but also for elucidating molecular structure and dynamics. It is particularly important for O-H stretch vibrational spectra of water, for which it is known that, in bulk, both intra- and intermolecular coupling alter the intensity and lineshape of the spectra. In contrast to bulk, the unified picture of the inter- / intra-molecular coupling of O-H groups at the water-air interface has been lacking. Here, combining sum-frequency generation experiments and simulation for isotopically diluted water and alcohols, we unveil effects of inter- and intra-molecular coupling on the vibrational spectra of interfacial water. Our results show that both inter- and intra-molecular coupling contribute to the O-H stretch vibrational response of the neat H_2O surface – with intramolecular coupling generating a double-peak feature, while the intermolecular coupling induces a significant red-shift in the O-H stretch response.

Vibrational spectroscopy techniques are widely used to obtain structural and dynamic insight into macroscopic ensembles.[41,42] Local vibrational modes are probed to extract molecular-level information about the structure and dynamics of liquids, such as the intermolecular interaction strengths between solute and solvent, and the binding sites of biomolecules.[43] However, the vibrational response of molecules often deviates from their vibrational density of states due to mode coupling, complicating the interpretation of the vibrational responses. Connecting the vibrational spectra to molecular-level information on the structures requires an understanding of these coupling effects. Vibrational coupling relies on interactions between different vibrations and requires a close proximity of the atoms involved. The coupling becomes strongest when the different modes are energetically (nearly-) degenerated. For instance, fundamental and overtone states of different modes with similar energy levels can be coupled with each other, leading to population of the (optically generally dark) overtone and an energy splitting, known as Fermi Resonance (FR). Moreover, coupling between different molecules of the same species can occur, giving rise to mode delocalization, often resulting in a broadened and / or enhanced response.[42]

The O-H stretch mode of condensed (H-bonded) water is a typical case for which coupling is known to critically affect the vibrational spectra. As has been shown theoretically[44–48] and inferred from time-resolved vibrational measurements,[49–51] vibrational mode coupling can occur between O-H stretch-oscillators of both the same and different water molecules and thus in an intra- and intermolecular fashion. These couplings enhance the speed of spectral diffusion through intermolecular vibrational energy transfer[50,52] and vibrational energy transfer from the O-H stretch mode to the H-O-H bend mode.[53–56] This characterizes the unique vibrational dynamics of water such as a marked frequency dependence of the vibrational relaxation time,[57] and ultrafast anisotropy decay on a time scale of ~100 fs.[49,50,58]

For interfacial water, the situation is different than for bulk water since the hydrogen bonding network is interrupted at the interface causing reorganization of water molecules. The structure of interfacial water has been studied using vibrational sum-frequency generation (V-SFG)-spectroscopy.[59–61] V-SFG is a surface-specific vibrational technique that provides the vibrational response of the outermost few water layers at an interface. This technique has revealed the presence of the dangling O-H group at the water / air interface[36] and similar hydrogen bond structure to that in the bulk.[57,60–62] Different reports exist on the effects of the intra- / inter-molecular couplings of water; so far, the experimentally determined response of the O-H stretch vibration at the water/air interface has been extensively discussed in terms of anharmonic FR coupling of intramolecular nature,[62–64] while the effects of intermolecular couplings on the O-H stretch SFG feature has been theoretically proposed.[65–68] A systematic discussion of, and a decomposition into, intramolecular and intermolecular couplings of interfacial water has not been reported, to the best of our knowledge.

In this work, we elucidate the role of inter- and intra-molecular vibrational couplings of the O-H stretch mode at the water/air, methanol/air and ethanol/air interfaces. Since ethanol and methanol cannot have intramolecular coupling between OH groups, the variation of the SFG spectra of these liquids and their isotopically diluted versions can be ascribed solely to intermolecular coupling. The SFG spectra of these alcohols show the impact of the intermolecular coupling of the O-H stretch mode on the SFG spectra, while the presence of a double-peaked feature in the response of the water/air SFG spectra indicates that the water O-H stretch spectra cannot be explained solely by intermolecular coupling. This suggests competing effects of the FR and intermolecular couplings. Molecular dynamics (MD) simulation support these experimental observations; the computed SFG spectra illustrate that the O-H stretch SFG feature is red-shifted due to the intermolecular couplings and reveals that a splitting of the energy level occurs due to the intramolecular coupling, which generates a double-peaked feature.

V-SFG spectroscopy was employed, combining a broadband femtosecond infrared laser pulse with a narrowband visible pulse. All spectra presented here were carried out in ssp polarization combination (*s*-polarized SFG, *s*-polarized visible and *p*-polarized IR) and at incident angles of 35° (SFG), 34° (VIS) and 36° (IR) with respect to the surface normal. Each spectrum results from averaging six 10-minute spectral accumulations, normalized by a non-resonant sum frequency signal from a *z*-cut quartz crystal and Fresnel-corrected using refractive indices reported elsewhere.[35,69] Details of the experimental SFG spectroscopy as well as the IR and Raman VV measurements are given in chapter 2.4 and 2.5, respectively. For the calculated SFG spectra based on the MD simulation, we ran a total of 10 ns MD trajectories with the POLI2VS force field.[70] The 26.6 Å × 26.6 Å × 100 Å simulation cell contained 500 water molecules. The spectra were computed based on the dipole moment-polarizability correlation function,[71] within the truncating response function scheme.[65] The details of the simulations are given in chapter 2.4.4.

2.2 Results and Discussion

First, we measured the V-SFG responses of C-H and O-H stretch modes of neat ethanol and methanol as well as the O-H stretch mode of neat H_2O. The spectra are displayed in Figure 13. The SFG spectral features are consistent with previous studies[6,72–75] (see chapter 2.4 for a more detailed discussion). The V-SFG spectra result from a combined infrared-Raman transition. As such, to examine the spectral features of the interfacial molecules with those of the bulk molecules, we obtained the IR and Raman (VV) spectra (I_{IR} and $I_{\mathrm{Raman(VV)}}$, respectively) and constructed the IR*Raman(VV) spectra from $I_{\mathrm{IR}} \times I_{\mathrm{Raman(VV)}}$. The SFG spectral shapes of neat water, methanol, and ethanol are well-captured by the corresponding IR*Raman(VV) spectra. This indicates that the spectral features of the interfacial molecule are similar to those in the bulk. Furthermore, one can see that the C-H stretch mode peaks are much larger than those from O-H stretch modes. This causes the large interference of the C-H stretch peak of methanol and ethanol and the non-resonant background generating a tilted off-resonant contribution in the O-H stretch region, shown in Figure 14.

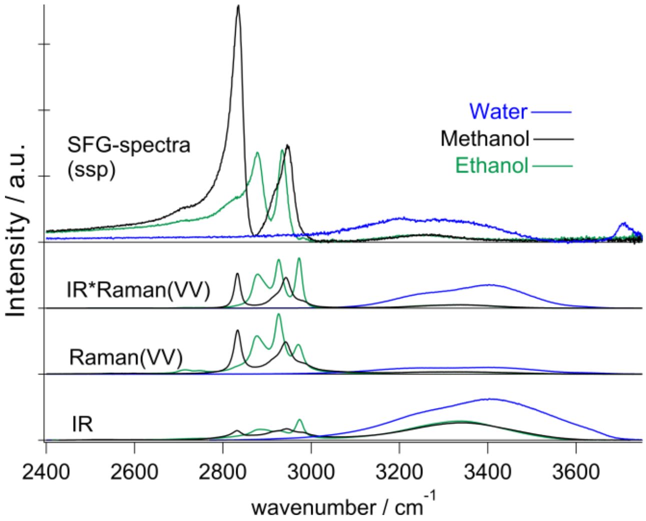

Figure 13: The measured bulk IR, Raman(VV) and constructed IR*Raman(VV) spectra of water (blue), methanol (black) and ethanol (green) as well as the Fresnel-corrected SFG(ssp) $\left(=\left|\chi^{(2)}_{yyz}\right|^2\right)$ spectra of corresponding liquid/air interfaces. For the SFG spectra, each tick represents ~1*10^{-42} m^4/V^2, based on a bulk $\chi^{(2)}$ value for Quartz of 8.0*10^{-13} m/V.[76]

Figure 14 shows the O-H-stretch SFG spectra of isotopically diluted water, methanol and ethanol, where the O-H group of these molecules are (partly or completely) replaced with O-D groups. Comparison of the SFG spectra of neat water, methanol, and ethanol with those of isotopically diluted spectra provides information about the impact of intermolecular coupling on the vibrational response of these interfacial H-bonded structures. The underlying idea is that the variation of the O-H stretch SFG features for the neat and isotopically diluted methanol and ethanol can be uniquely linked to the intermolecular coupling of the O-H stretch mode, since there is no intramolecular OH-coupling, unlike for water. Therefore, we first focus on the SFG spectra of these alcohols. The SFG spectra are depicted in 14A and 2B. The disappearance of vibrational intensity on the red side of the O-H stretch peak upon isotopic dilution indicates that the O-H stretch modes of both alcohols are coupled intermolecularly with other O-H vibrational chromophores at the liquid/air interface; the intermolecular coupling of the O-H stretch mode broadens the O-H stretch peak and red-shifts the peak frequency. The variation of the SFG spectra closely resembles that of the constructed IR*Raman(VV) spectra (bottom panel in Figure 14), indicating that this coupling is commonly found both, at the interface and in the bulk.

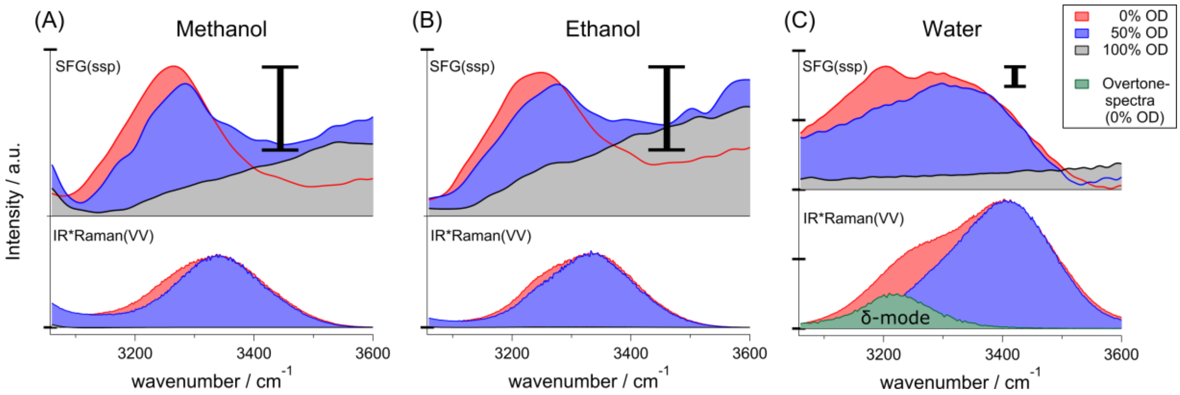

Figure 14: Fresnel-corrected SFG (ssp) $\left(=\left|\chi_{yyz}^{(2)}\right|^{2}\right)$ and bulk IR*Raman(VV) spectra of Methanol (A), Ethanol (B) and Water (C) for 100% OH (red), 50% OH / 50% OD (blue) and 100% OD (black). For comparison, each 50% OH dilution spectrum is scaled up with its maximum to match the corresponding 100% OH spectrum. For the alcohol spectra, the absolute scale is zoomed by a factor of 4, indicated by the scalebars. The slope in the background arising from interference between the large CH-resonances and the non-resonant contribution is explained in detail in the SI. For the constructed IR*Raman(VV) spectra of bulk water, the water bending mode overtone spectrum is also plotted with 4% anharmonicity[77] and multiplied in amplitude by a factor of 10. Original spectra and smoothing method are presented in the SI.

Figure 14 shows corresponding spectra of neat, and isotopically diluted water. The double-peak feature of the hydrogen-bonded O-H stretch SFG spectra for neat H_2O is merged into a single peak for the isotopically diluted H_2O. This trend is consistent with previous observations.[60,78] Although this isotopic dilution approach itself cannot disentangle the influence of intra- and intermolecular couplings on the O-H stretch SFG spectra, the comparison of the SFG spectra variation of water with those of methanol / ethanol gives a hint for the effects of the intra- and inter-molecular couplings. The SFG spectra of all three liquids exhibit an enhanced SFG intensity around ~3200 cm^{-1}; this seems to originate from intermolecular interactions of O-H groups. For water, moreover a double-peak feature is apparent, which cannot be observed in the SFG spectra of methanol or ethanol. So far, this double-peak feature in the water SFG spectrum has been ascribed to the anharmonic FR coupling of the O-H stretch mode and H-O-H bending overtone.[64] The response of the H-O-H bending overtone in bulk water is also depicted in Figure 14C (bottom panel).

To experimentally explore whether the anharmonic FR can generate such a double-peak feature of the O-H stretch mode, we compare the O-H stretch features with the O-D stretch features of neat methanol and isotopically diluted methanol in the constructed IR*Raman(VV) spectra. The spectra are presented in Figure 1515. For methanol, the O-H stretch region is decoupled from the overtone of the H-O-C bending mode. Therefore, the variation of the O-H stretch spectra must arise solely from the intermolecular coupling, as is illustrated in Figure 14A. In contrast, the overtone of the bending mode overlaps with the O-D stretch band (2200-2600 cm^{-1}), which results in an FR. As such, the variation of the O-D stretch spectra of deuterated methanol will be affected by both the FR and intermolecular coupling. Remarkably, while the O-H stretch spectrum looks smooth, the O-D stretch spectrum of methanol exhibits a double-peak feature, much like that observed for the pure water spectrum. This demonstrates that the FR is a very likely candidate to explain the double-peak feature of the SFG spectra of water.

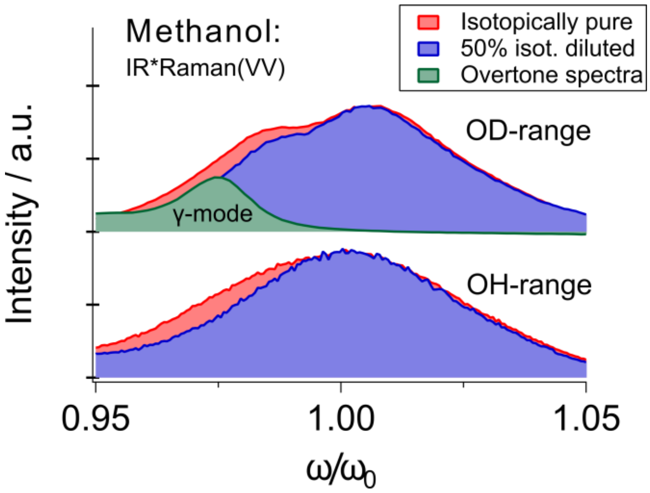

Figure 15: Constructed IR*Raman(VV) spectra of methanol within the OH- and OD-stretching region, normalized to their central frequencies and scaled to equal intensity. For both ranges, the isotopically pure (100% OH or OD, red), the 50% dilution (blue) and the overtone spectrum ($\omega_{ov}=\omega_{fundamental}*1.96$) are plotted. The overtone spectrum is multiplied by a factor of 10.

Above, our experimental observations show that the intermolecular coupling between O-H stretch modes red-shifts the O-H stretch SFG peak, while the FR with the bending mode overtone can generate the double-peak feature in the SFG spectra of neat H_2O at the water/air interface. To verify these conclusions, we performed MD simulations at the neat H_2O/air and neat HDO/air interface and computed the O-H stretch SFG spectra of H_2O and HDO. The SFG spectrum calculated with the autocorrelation (AC) term for neat HDO (HDO (AC) spectrum) corresponds to the spectrum of an isolated O-H group in D_2O. The SFG spectrum with the cross-correlation (CC) term for neat H_2O corresponds to the neat H_2O SFG spectrum (H_2O (AC+CC) spectrum). The difference between the spectra calculated with the autocorrelation (AC) terms of neat H_2O (H_2O (AC) spectrum) and the H_2O (AC+CC) spectrum is the contribution of the intermolecular O-H stretch mode couplings. The difference between the H_2O (AC) and HDO (AC) spectra can be considered as the contribution of intramolecular coupling, including the FR contribution, to the overall response. The imaginary part of the SFG response for HDO (AC), H_2O (AC), and H_2O (AC+CC) are shown in Figure 16A.

The difference between the HDO (AC) and H_2O (AC) spectra indicates the intramolecular couplings including the FR can enhance the spectral amplitude at 3300 cm^{-1} and 3440 cm^{-1}, causing a vibrational energy splitting by 140 cm^{-1}: the intramolecular coupling of the O-H stretch chromophores does not uniformly enhance the H-bonded O-H stretch band. This illustrates that the intramolecular coupling causes energy splitting, generating the double-peak feature, consistent with the experimental observation. However, the difference between the H_2O (AC) and HDO (AC) spectra is relatively small compared with the difference between the H_2O (AC+CC) and H_2O (AC) spectra. This indicates that the intermolecular coupling strongly affects the SFG spectra of water and red-shifts the H-bonded O-H stretch band.

For comparison, the experimentally determined $\mathrm{Im}\left(\chi^{(2)}\right)$ spectra[79] of neat H_2O and that of HDO are presented in panel B of Figure 16. The HOD response was obtained from the response of a 3:1 D_2O:H_2O mixture, correcting for the statistically present H_2O molecules in such a mixture[60,78]. These $\mathrm{Im}\left(\chi^{(2)}\right)$spectra are slightly different from literature spectra,[60,78] which is probably caused by uncertainties in correcting for the phase in the heterodyne experiments.[80,81] Qualitatively, the experimental spectra agree with the simulated ones, as they show a decrease of intensity on the low-frequency side of the absorption band upon isotopic dilution associated with involved coupling mechanisms discussed above.

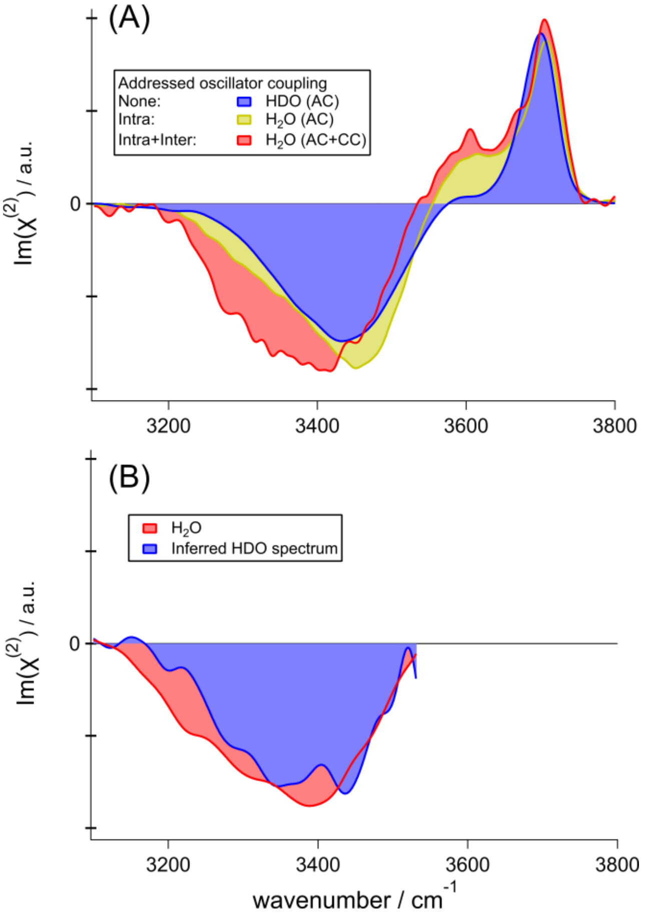

Figure 16: Imaginary part of $\chi^{(2)}$ for the water/air interface. (A): Spectra derived from AIMD simulations of HDO and H_2O. To address inter- and intra-molecular coupling separately, auto- (AC) and cross- (CC) correlation terms are calculated for both systems. (B): Smoothed measured spectra $\left(=\mathrm{Im}\left(\chi^{(2)}_{yyz}\right)\right)$ of neat H_2O and H_2O isotopically diluted with 75% OD.[79]

2.3 Conclusion

In conclusion, our results illustrate that, at the surface as in the bulk, intermolecular coupling results in red-shifted and broadened absorption bands of H-bonded O-H stretches. For O-H groups of short-chain alcohols, we find experimentally that there is a substantial contribution of intermolecular coupling to the vibrational SFG response of H-bonded O-H groups at the surface, similarly to responses in the bulk. A comparison between O-H- and O-D-bands revealed that anharmonic FR coupling results in energy splitting of these broad absorption bands while the major broadening effect is of intermolecular nature. MD simulations of the water/air interface agree with our experimental findings and further demonstrate that for the broadening of the H-bonded O-H stretching band, the difference spectra of neat H_2O and isotopically diluted water arises more from inter- rather than intramolecular couplings. Our results provide experimental evidence for the impact of the delocalized character in H-bonded O-H structures on their vibrational responses.

2.4 Further Experimental Details

2.4.1 Chemicals

Methanol(-d) and Ethanol(-d) (99.5% D) as well as the non-deuterated analogs (CHROMASOLV®, ≥99.8%) were purchased from Sigma Aldrich. D_2O was obtained from Euriso-Top (99.85% D) and H_2O was demineralized and filtered with a Millipore unit (Resistivity = 18 MΩ cm).

2.4.2 SFG spectroscopy

All spectra presented in this work were carried out in ssp polarization combination (*s*-polarized SFG, *s*-polarized visible and *p*-polarized IR) and at incident angles (θ_1) of 35° (SFG), 34° (VIS) and 36° (IR). The frequency-dependent IR field was determined from a non-resonant sum frequency signal from a *z*-cut quartz crystal. To avoid changing sample height due to evaporation, the sample temperature was adjusted to 5°C with the help of a commercial chiller (Lauda RCS6) connected to a copper plate and controlled by a probe PT100 resistance thermometer. Samples were prepared in a trough made from stainless steel (approximately 5 mL). Fresnel correction was carried out based on refractive indices (n) at 25°C (n(H_2O), n(D_2O)[35] for water and n(MeOH), n(MeOD)[69] for Methanol and Ethanol).

2.4.3 Bulk IR and Raman measurements

The IR spectra were recorded with a Nicolet 730 FTIR spectrometer with each sample being sandwiched between two CaF_2 windows. The resulting spectra of isotopically pure samples were scaled according to absolute absorption coefficients published in previous works[35,69]. Since ATR-FTIR gives equal OH absorption bands for ethanol and methanol, ethanol spectra were also scaled according to the methanol reference. Raman spectra were taken with a Nikon eclipse Ci Micro Raman Microscope System 633-CiL. For each IR and Raman spectrum, 100*1 second spectra were averaged. All IR, Raman and (IR*Raman) spectra were arbitrarily intensity scaled but with the same factor for each method.

2.4.4 Simulation Protocols

We used the POLI2VS force field model for a water molecule. Since the original force field model was designed to simulate the H_2O system, we modified this POLI2VS force field model[82] to simulate the HDO and D_2O systems as follows. The mass of the H atom was changed for HDO which affects the velocity Verlet algorithm for integrating the equations of motion, while the center of mass position for calculating the damping function (equation (28) of Ref. [70]) was calculated based on the H_2O geometry over the HDO molecule. The time step for integrating equations of motion was set to 0.4 fs. We recorded the trajectories of water molecules, molecular dipole moment, and polarizability every 4 fs (every 10 MD steps). The simulations were performed in the canonical ensemble. The temperature was set to 300 K and was controlled with the Nose-Hoover thermostat. The cell size was 26.6 Å × 26.6 Å × 100 Å. This cell contains 500 water molecules. Note that this cell size and the number of water molecules were the same as our previous studies at the water-air interface.[68,83] We ran the 1 ns MD simulations for the H_2O and HDO systems for equilibrating the systems. Subsequently, we ran over 15 ns MD simulations for recoding the trajectories, dipole moment, and polarizability.

The methodology to compute the SFG susceptibility from the simulation has been reported in Refs [68,83]. Here, we describe the simulation details briefly. The resonant part of the second-order susceptibility at the *xxz* direction (*x*: SFG, *x*: visible, *z*: IR) can be calculated with the truncating response function formalism as [65,83]

$$\chi_{xxz}^{\mathrm{res},(2)}(\omega; r_t) = iQ(\omega)\int_0^{\tau} dt R_{xxz}^{(2)}\left(t; r_t\right) f(t) e^{-i\omega t} \tag{28}$$

where the *z*-axis denotes the surface normal and the *xy* plane denotes the interface. Q(ω) is the quantum correction factor,[68] $\beta = 1/kT$ is the inverse temperature of the system. *f*(*t*) is the Hann window function and *τ* is the limit of the time for Fourier transformation. We used *τ* = 1 ps. The truncated time correlation function $R_{xxz}^{(2)}(t; r_t)$ is given by

$$\begin{aligned} R_{xxz}^{(2)}(t; r_{\mathrm{t}}) = \Bigg\langle & \sum_i g_{sc}^3(z_i(0))\mu_{zi}(0)\alpha_{xxi}(t) \\ & + \sum_i \sum_{j\neq i} g_{sc}(z_i(0)) g_{sc}^2(z_j(0))\mu_{zi}(0)\alpha_{xxj}(t) g_t(r_{ij}(0); r_t) \Bigg\rangle \end{aligned} \tag{29}$$

where $\mu_{a,i}(t)$ ($\alpha_{ab,i}(t)$) is the *a* component of the molecular dipole moment (the *ab* component of the molecular polarizability) of water molecule *i* at time *t*. $g_t(r; r_t)$ is the function to control the cross-correlation terms with the cross-correlation cutoff of r_t and is given by

$$g_t(r;r_t) = \begin{cases} 1 \ \text{ for } \ r \le r_t \\ 0 \ \text{ for } \ r > r_t \end{cases} \tag{30}$$

To avoid the cancellation of the molecular dipole moments at the two interfaces where the net orientation of the water molecules are exactly opposite, we multiplied the dipole moment by the screening function of

$$g_{sc}(z) = \mathrm{sign}(z) \times \begin{cases} 0 \ \text{ if } \ |z| \le z_{\mathrm{c1}} \\ \cos^2\left(\dfrac{\pi(|z| - z_{\mathrm{c2}})}{2(z_{\mathrm{c1}} - z_{\mathrm{c2}})}\right) \ \text{ if } \ z_{\mathrm{c1}} < |z| \le z_{\mathrm{c2}} \\ 1 \ \text{ if } \ z_{\mathrm{c2}} < |z| \end{cases} \tag{31}$$

where *z* denotes the *z*-coordinate of the center of mass of a water molecule.[65] Here, we set z_{c1} = 3 Å and z_{c2} = 4 Å, where the origin point was set to the center of mass of the system.

We do not include the nuclear quantum effects in the present MD simulation. The nuclear quantum effects lead to the red shift of vibrational signatures.[70,84] Because the simulated IR peak frequency of bulk H_2O is blue shifted by ~4 % compared with the IR experimental spectra,[70] we multiplied the frequency by 0.96 in order to reproduce the corresponding vibrational SFG signature.[83]

2.5 Additional Data

2.5.1 Decomposition of the instrumental response into bulk optical properties and surface-specific orientational effects

Figure 17 shows Fresnel-corrected SFG spectra of the methanol/air interface in ssp polarization combination compared to IR, Raman(VV) and constructed IR*Raman(VV) spectra of the two methanol isotopologues, CH_3OH and CH_3OD. As can be inferred, the relative SFG intensity of the CH-stretching modes is higher by about one order of magnitude than the resonances originating from OH (or OD) stretches. This can be qualitatively explained by the bulk optical properties of those functional groups, i.e. from the IR- and

Raman(VV)- spectra. While the OH (OD)-stretching band is limited by its Raman cross-section, the CH-stretching bands are restricted by the IR cross-section. This indicates a higher permanent dipole but lower polarizability of the OH (OD)-bond compared to the CH-bond.

However, the symmetric CH_3-stretching band at the surface (2835 cm^{-1}) is about 4-times higher in the recorded SFG-spectra compared to the constructed ones. This suggests particular high order of involved transition moments which agrees with orientational studies done before. As discussed extensively, surface Methanol appears to show high order of CH_3-groups pointing into the gas phase with the C-O axis being oriented orthogonal to the surface plane (± 1°).[2,82,85]

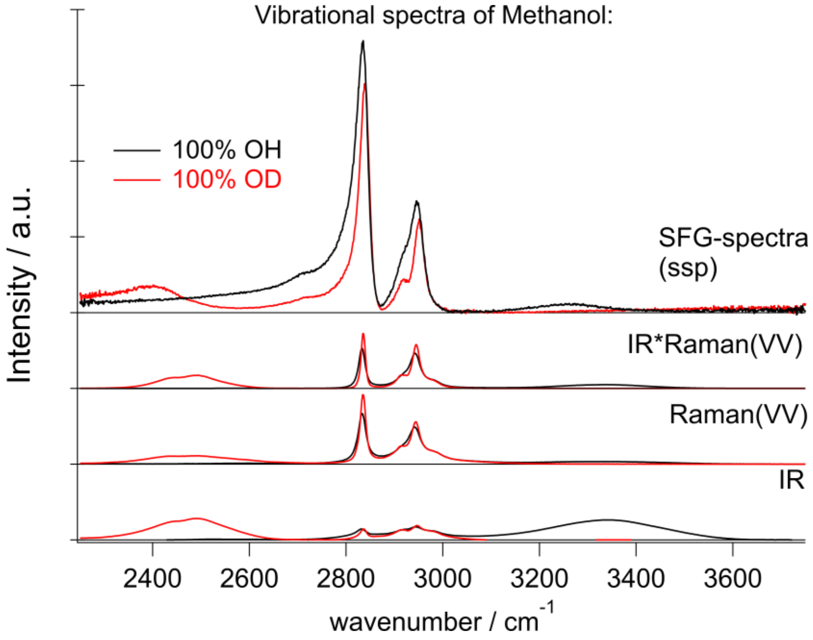

Figure 17: Vibrational spectra of Methanol and the Methanol/air interface given by the Fresnel-corrected SFG (ssp), the IR, Raman(VV) and constructed IR*Raman(VV) spectra within the OD-, CH- and OH-stretching region. For each method, both isotopologues, 100% OH (black) and 100% OD (red), are presented.

In contrast to the bulk spectra, resonances in the SFG spectra are distorted with a tail towards their low-frequency side which is due to mixing of resonant and non-resonant contributions. Therefore, the OD-band interferes with the CH_3-tail which complicates the analysis of corresponding isotopic dilution experiments. As shown in Figure 18, the same is true for ethanol even though the CH_3-band is not as pronounced, indicating a more tilted orientation at the surface (~ 40°).[86] From bulk spectra, an intense resonance of ethanol is additionally expected at around 2973 cm^{-1} which has been assigned to an asymmetric CH_3-stretching mode being silent in ssp but appearing in ppp polarization spectra.[86] Here, we can conclude that this band originates from the $\chi_{zzz}^{(2)}$ tensor which is not addressed in ssp polarization spectra but necessarily included in the (IR*Raman(VV)) constructed ones.

A comparison between the SFG spectra of water and the alcohols further reveals that the OH-signal is about 3-times higher in the case of water which also agrees with corresponding bulk cross-sections indicating a higher polarizability of OH-groups in water. Compared to water, the SFG spectra of methanol and ethanol do not show the high-frequency resonance at around 3700 cm^{-1} suggesting that there is no free OH present at the surface, which confirms the orientational analysis performed previously.[2,82,85,86]

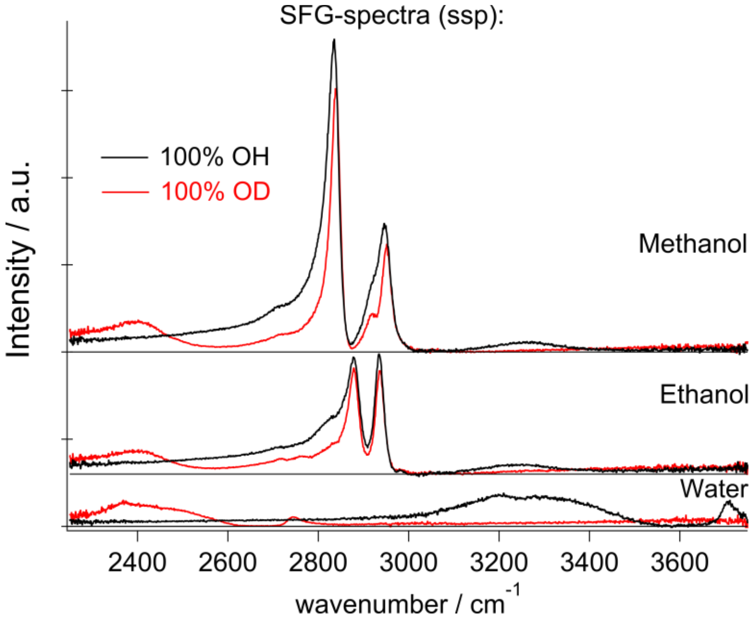

Figure 18 Fresnel-corrected SFG (ssp) spectra for Water, Methanol and Ethanol within the OD-, CH- and OH- stretching region. For each system, both isotopologues, 100% OH (black) and 100% OD (red), are presented.

As mentioned in the main text, the alcohol SFG spectra show a tilted background which arises from interference between the high CH-vibrational resonances and the non-resonant contribution. Figure 19 provides a detailed view of this interference.

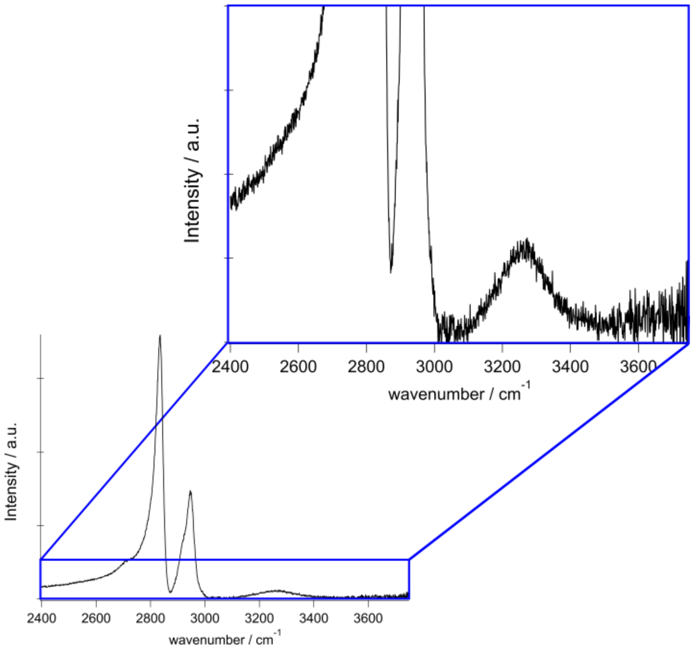

Figure 19: Fresnel-corrected SFG (ssp) spectrum of Methanol (100% OH) and the same spectrum zoomed along the Intensity axis.

2.5.2 Smoothing procedure applied on SFG spectra

For the analysis done by means of Figure 14, the SFG spectra were smoothed with a Gaussian filter. The smoothed spectra are presented in Figure 20 together with their raw data (already normalized and Fresnel corrected). Due to different signal / noise ratio for water and the alcohols a smoothing factor off 100 and 500 was applied, respectively.

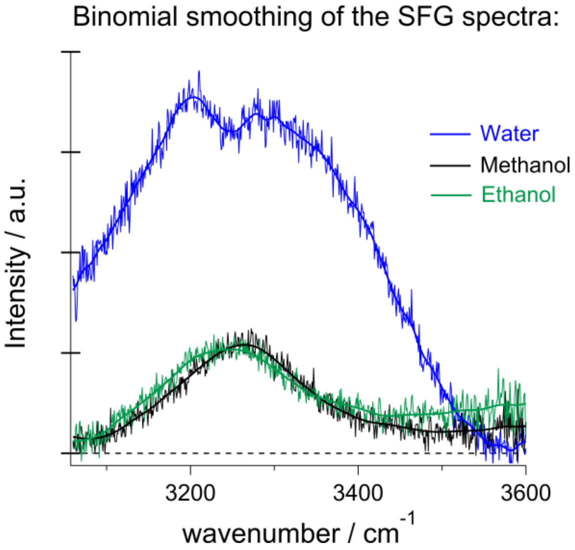

Figure 20: Fresnel-corrected SFG (ssp) spectra of the water / air, methanol / air and ethanol / air interface. The raw data are depicted together with the smoothed spectra as used in Figure 14.

3 The vibrational response of water at a charged surface: screening and interference

Copyright: This work is based on Jan Schaefer, Grazia Gonella, Mischa Bonn, and Ellen H. G. Backus 2017. Surface-specific vibrational spectroscopy of the water/silica interface: screening and interference. *Physical Chemistry Chemical Physics.* 2017 Royal Society of Chemistry. Open Access as stated under the Creative Commons license: http://creativecommons.org/licenses/by/4.0/

Acknowledgment: The Gouy-Chapman-based SFG model used in this work was provided by Dr. Grazia Gonella. My contribution to this work was the acquisition and analysis of the SFG data.

3.1 Introduction

Surface-specific vibrational sum-frequency generation spectroscopy (V-SFG) is frequently used to obtain information about the molecular structure at charged interfaces. Here, we provide experimental evidence that not only screening of surface charges but also interference limits the extent to which V-SFG probes interfacial water at sub-mM salt concentrations. As a consequence, V-SFG yields information about the ~single monolayer interfacial region not only at very high ionic strength, where the surface charge is effectively screened, but also for pure water due to the particularly large screening length at this low ionic strength. At these low ionic strengths, the large screening lengths cause destructive interference between contributions in the near-surface region. A recently proposed theoretical framework near-quantitatively describes our experimental findings by considering only interference and screening. However, a comparison between NaCl and LiCl reveals ion-specific effects in the screening efficiency of different electrolytes. Independent of electrolyte, the hydrogen bonding strength of water right at the interface is enhanced at high electrolyte concentrations.

In contact with water, mineral surfaces may accumulate an excess of positive or negative charges, which in turn affects the arrangement of interfacial water molecules. Through interaction with the associated DC electric field, interfacial water layers form the so-called electric double layer (EDL) which consists of the near-surface, highly ordered Stern layer, and the more diffuse outer water layers. It is clear that interfacial chemistry, relevant for many geological and industrial processes, is affected by the reaction of dipolar interfacial molecules, in particular water, to the surface field. The distance-dependent potential associated to such an electric field is typically described by the Gouy-Chapman-Stern model, assuming an exponential decay of the potential away from the surface through the diffuse layer, while the Stern layer is characterized by a linear drop in analogy to a dielectric capacitor.

Associated parameters such as surface potential, surface charge density and Debye screening length are challenging to access experimentally. Besides potentiometric titration,[87,88] Atomic Force Microscopy[89] and X-ray Photoelectron Spectroscopy[11,90], also non-linear spectroscopy techniques have been demonstrated to be a useful tool for studying these kind of interfaces.[12,14,15,18,21–25,32,33,91,92] As such, we employed Vibrational Sum Frequency Generation (V-SFG) spectroscopy for interrogating those interfacial properties, since it allows for probing vibrational states of interfacial molecules with sub-micrometer sensitivity and selectivity towards the symmetry-broken interfacial layers (given by the additional symmetry selection rule underlying V-SFG processes). Using this technique, we study how the presence of ions changes the composition of the EDL for water at a mineral surface. Specifically, we aim to understand to which depth water interacts with the surface electric field and if the intermolecular structure of interfacial water is affected differently by the presence of ions than that of bulk water. For this purpose, we investigated the silica/water interface with varying electrolyte content. Around neutral pH, the silica surface is covered by silanol groups which are mostly deprotonated, generating a negatively charged surface as the point of zero charge (pzc) is pH 2.[25,87]

V-SFG spectra of neutral interfaces are commonly discussed by invoking the second-order non-linear susceptibility $\chi^{(2)}$ of involved media. Based on symmetry arguments, $\chi^{(2)}$ is zero for centro-symmetric materials. This makes V-SFG a sensitive probe for the first few molecular layers of e.g. water at interfaces, as only at the interface centro-symmetry is broken. Moreover, $\chi^{(2)}$ is proportional to molecular order and molecular number density. However, as discussed previously,[13–15,93,94] this description does not suffice in the presence of charged interfaces since surface charges may induce an extra DC electric field E_{DC} which, in addition to the IR- and VIS- fields E_{IR} , and E_{VIS} , also act on non-linear active molecules in the proximity of the surface. This gives rise to an additional third order ($\chi^{(3)}$) contribution to the V-SFG response which depends on the penetration depth of the

DC field and may even exceed the $\chi^{(2)}$-response. As a consequence, the generated V-SFG signal contains a $\chi^{(2)}$ contribution from directly bonded interfacial molecules and a $\chi^{(3)}$ contribution from up to ~1 µm away from the surface for low ion concentrations.[12] In contrast to $\chi^{(2)}$, not only oriented but also isotropic water may contribute to $\chi^{(3)}$ signal, i.e. $\chi^{(3)}_{aniso}$ and $\chi^{(3)}_{iso}$. As such, the V-SFG intensity of charged interfaces does not purely reflect the degree of interfacial order but is a convolution of field-induced reorientation and polarization: [14,15,95]

$$I(SFG) \propto \left| E_{VIS} E_{IR} \chi^{(2)} + \int_0^{+\infty} E_{VIS} E_{IR} E_{DC}(z) \chi^{(3)} dz \right|^2 \tag{32}$$

$$\chi^{(3)} = \chi^{(3)}_{aniso} + \chi^{(3)}_{iso} \tag{33}$$

It is clear from equation 32 that the V-SFG intensity of such systems depends strongly on the number of molecules interacting with the DC electric field. That number is determined by the strength and decay length of that field, which, in turn, are defined by the charge density at the surface and the Debye screening length of the solution. With increasing bulk ion concentration, the surface charges are increasingly shielded, resulting in reduced penetration depths of the DC field. Conversely, with increasing Debye length (i.e. decreasing bulk ion concentration) an increasing number of molecules contribute, resulting in a higher V-SFG signal. For a given surface charge, the probing depth can thus be tuned by varying the ionic content in the solution.

As the V-SFG signal of charged interfaces is thus composed of a complex interplay between the bonded interfacial layer $\left(\chi^{(2)}\right)$ and the diffuse layer $\left(\chi^{(3)}\right)$ response, it is a priori not clear how these contributions are convoluted in the V-SFG spectrum. For the silica/water interface, the correlation between V-SFG intensity and bulk ion concentration has been studied experimentally for aqueous sodium chloride solutions between 10^{-4} M and 4 M.[15] The decrease of the V-SFG intensity with increasing electrolyte concentration has mainly been attributed to Debye screening due to the presence of electrolyte. However, a second electrolyte concentration-dependent effect has been proposed, based on theoretical considerations and direct observation by second harmonic scattering[12,96]. At very low electrolyte concentrations, the probing depth can be limited by phase matching of the V-

SFG probe. Hence, as the penetration depth of the DC field exceeds the coherence length, the signal intensity is expected to be increasingly depleted due to destructive interference between contributions from sufficiently spatially separated non-linear active molecules.[12] For particularly large penetration depths, the third order contribution vanishes completely and only the field-independent V-SFG response of the bonded interfacial layer $\left(\chi^{(2)}\right)$ survives.[12] The V-SFG intensity may thus not necessarily increase with the number of molecules affected by the DC field as has been generally assumed [13–15,37,40,91], but decreases if the DC field reaches the magnitude of the coherence length of the probed non-linear process.[12,21]

Here, we provide new insights into the sparsely studied regime of low ionic strength ([NaCl] < 5×10^{-4} M) for which we observe an inverted dependence between ionic strength and the V-SFG signal intensity in accordance with theoretical predictions.[12] We demonstrate experimentally that V-SFG spectroscopy provides interfacial layer sensitivity to the silica/water interface both for pure water and for highly concentrated (>1 M) NaCl solutions. Furthermore, we show that the overall concentration dependence of the V-SFG intensity is similar for monovalent cations of different radii, however they seem to differ in their screening efficiency. Moreover, we observe significant redshifts of the O-H stretch signal for high electrolyte concentration, which can only be rationalized by invoking surface-specific effects. Apparently, salt has a different impact on water molecules close to the surface than on water molecules in the bulk.

3.2 Results and Discussion

The top panel in Figure 21 depicts V-SFG spectra of the silica/water interface within the C-H- / O-H-stretch frequency window for three different NaCl concentrations. The spectra show the typical double peak O-H feature between ~2900 and 3500 cm^{-1}, as discussed in earlier studies of water in contact with silica surfaces.[15,18,32,91] Due to the absence of any C-H vibrational signatures, there is no indication of surface contamination with organic impurities. Compared to pure water and the 1 M NaCl solution, which show similar intensity, the signal from the 5×10^{-4} molar solution is significantly enhanced. The presented spectra in Figure 21 are raw data, not normalized to the spectrum of the IR pulse as we are only interested in relative changes of the O-H-band. The normalized spectra can be found in the chapter 3.5.1. For a dilution series of 20 different NaCl concentrations, we integrate the corresponding spectra between 2800 and 3600 cm^{-1}, and the resulting integrated signals are plotted as a function of the ion concentration in the bottom panel of Figure 21.

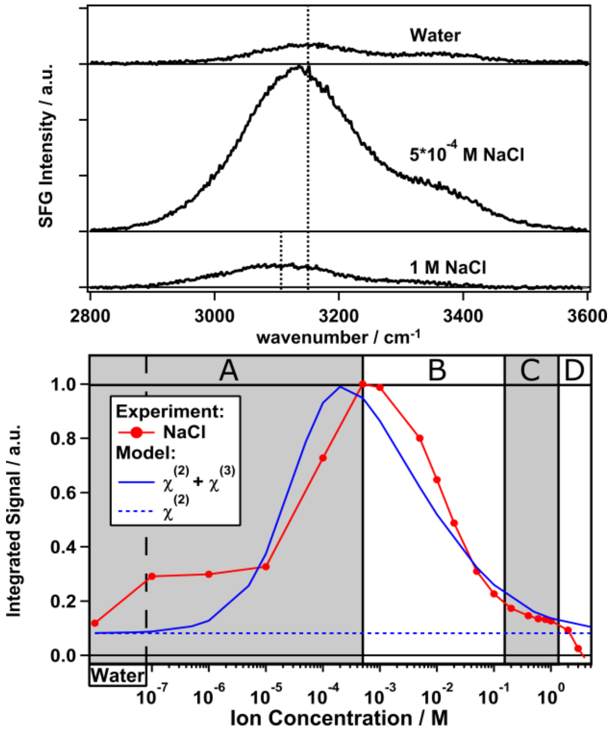

Figure 21: Top panel: Non-normalized OH-stretch V-SFG signal from the silica/water interface for pure water, 5×10^{-4} M and 1 M NaCl solutions. The black dashed lines mark the frequency at peak maximum for pure water and the 1 M NaCl solution. Bottom panel: Integrated V-SFG signal (red) as a function of NaCl concentration and the predicted intensity (blue solid) by invoking modulation by charge screening and interference (equation 35).[12] The blue dashed line represents the considered field-independent, true second-order contribution to the V-SFG response.

As illustrated in Figure 21, the V-SFG intensity of the O-H-stretching band dramatically depends on the bulk ion concentration. Overall, we observe an order of magnitude variation in the V-SFG signal upon the addition of NaCl to pure water. At both low and high concentration, the signal is small, while a maximum in the V-SFG intensity appears at ~5×10^{-4} M NaCl. This decrease of the V-SFG intensity for NaCl concentrations exceeding 5×10^{-4} M has been observed by Jena et al..[15] In that study, four different regimes of ion concentration have been distinguished (A-D). Similarly, we will now discuss our results and provide new insight into the concentration regime below 5×10^{-4} M (A). For the high concentration regimes (B-D), our results agree with the above mentioned observations[15] which we only summarize here.

Regime B: For [NaCl] > 5×10^{-4} M, the V-SFG signal decreases with increasing ion concentration due to increased screening.

Regime C: For high ionic strengths of around 1 M, the intensity is almost constant which indicates that the number of probed molecules and their orientation do not change substantially within this regime. It has been argued before that the signal in this region corresponds mostly to the intrinsic $\chi^{(2)}$ response, providing insight into the Stern layer of the silica/water interface.[15]

Regime D: For concentrations higher than 2 M, the intensity drops more rapidly which suggests either randomization of Stern layer water molecules or replacement by ions directly adsorbing on the silica surface.

Regime A: In contrast to Jena et al.,[15] we find that in this regime where [NaCl]< 5×10^{-4} M, the V-SFG intensity decreases with further decreasing salt concentration. For neat water, we observe a very low V-SFG signal. For avoiding contamination due to the dissolution of silica which is known to affect the V-SFG signal,[40] we flushed the cell with sample solution before starting each measurement. This finding can be rationalized, according to the model in Ref. [[12]], by considering the Debye screening length of pure water to be larger than the coherence length of the V-SFG process in the given experimental geometry (~40 nm) which gives rise to destructive interference and cancellation of the $\chi^{(3)}$ contribution. As the penetration depth of the DC field decreases upon adding salt, phase matching is increasingly fulfilled by approaching the coherence length, which results in a higher V-SFG intensity.

For understanding our data on a quantitative level, we employed the model for predicting the non-linear response as proposed in Ref. [[12]] which uses a Gouy-Chapman description of the EDL and phase matching condition of the non-linear process as given by:

$$I(SFG) \propto \left| E_{VIS} E_{IR} \left(\chi^{(2)} + \chi^{(3)} \int_0^{+\infty} E_{DC}(z) e^{i\Delta k_z z} dz \right) \right|^2 \tag{34}$$

where E_{DC} is the surface DC field, and Δk_z represents the phase mismatch accumulated for different points along the coordinate perpendicular to the silica/water interface z. By performing the integration with $E_{DC}(z) = -\frac{d\phi(z)}{dz}$ and by considering an exponentially decaying potential $\phi(z) = \phi_0(c) * exp(-\kappa(c)z)$ along the z-direction (perpendicular to the silica/water interface), the V-SFG intensity dependence on ionic strength can be formulated as follows:

$$I(SFG) \propto \left| E_{VIS} E_{IR} \left(\chi^{(2)} + \chi^{(3)} \phi_0(c) \frac{\kappa(c)}{\kappa(c) - i\Delta k_z} \right) \right|^2 \qquad (35)$$

Besides the intensity of the involved optical beams and the non-linear susceptibilities of water, the resulting V-SFG intensity is determined by the ionic strength-dependent Debye length, $\kappa(c)$, and surface potential, $\phi_0(c)$, (as described by the Grahame equation) as well as the phase mismatch along the probing depth, Δk_z, whose explicit definitions are given in chapter 3.5.2. As can be seen in equation 36-38, the surface potential is also directly dependent on the surface charge density, σ_0, and the relative permittivity of the aqueous medium, ε_r. For the V-SFG intensity vs. concentration curve generated in Figure 21, we have used $\sigma_0 = -0.05\ C/m^2$ and $\varepsilon_r = 78$ as suggested in Ref. [12]. Through comparison with our experimental data, we infer a $\chi^{(3)}/\chi^{(2)}$ ratio of $17.5\,V^{-1}$. Within the range of reported surface charge densities for fused silica around neutral pH, $-0.06\ C/m^2 < \sigma_0 < -0.02\ C/m^2$,[25,88,90,97,98] we find that comparable intensity curves can be obtained for $-22.25\,V^{-1} < \chi^{(3)}/\chi^{(2)} < -16.50\,V^{-1}$ as reported in chapter 3.5.3. These values for the $\chi^{(3)}/\chi^{(2)}$ ratio seem reasonable compared with previous studies of water at charged surfaces.[13,96] Note that for simplicity we assume that the charge density is constant for all salt concentrations. Small variation with concentration cannot be excluded as the surface charge density of silica ($-0.06\ C/m^2 < \sigma_0 < -0.02\ C/m^2$)[25,88,90,97,98] is typically around the critical surface charge density $(\sigma_{0,crit})$ above which counterion condensation occurs.[99]

We observe that the shape of the V-SFG intensity vs. ion concentration curve generated by the model agrees remarkably well with our experimental data. As predicted, pure water shows similar intensity as NaCl solutions within regime C (Figure 21) while the intensity is enhanced for an intermediate concentration regime with its maximum around [NaCl]=5×10^{-4} M. Based on the employed theoretical framework,[12] this indicates that the $\chi^{(2)}$-contribution (blue dashed line in Figure 21) dominates the pure water response and interfacial layer sensitivity is obtained not only at short but also at very large screening lengths. In contrast, the probing depth amounts to a few tens of nanometers for the maximum at 5×10^{-4} M NaCl. In its current form, the model seems to overestimate the screening contribution of NaCl, reducing the V-SFG intensity in the B-C regime and shifting the maximum to lower concentration than what is observed in the experiment.

While equation 35 discriminates between ions species with different valence, the effect of different ionic radii is ignored. However, ion size not only determines the Stern-layer thickness,[11] but might also be relevant for the screening ability since the ion mobility changes with the hydrated radius. For a negatively charged surface, the properties of the cations are especially important.[24,100] Therefore, we compare two not-too-different alkali ions, Na^+ and Li^+, where however Li^+ shows a lower ion mobility due to a smaller ionic but larger hydrated radius. In the same fashion as presented in Figure 21, we will now discuss the results of two measurement series for both NaCl and LiCl solutions which are shown in Figure 22. Again, the integrated signal is plotted as a function of ion concentration and the curves are each normalized to their maximum.

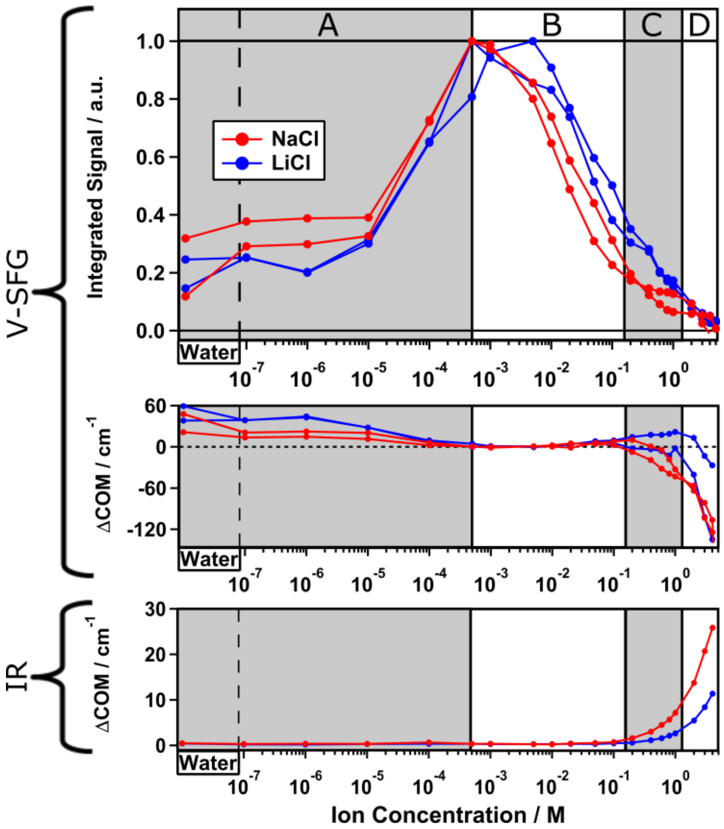

Figure 22: Two experiments for two dilution series of NaCl (red) and LiCl (blue). Top panel: Integrated OH-stretch V-SFG signal. Middle panel: Center of mass frequency shifts of the corresponding signals, each referenced to the maximum signal at 5*10^{-4} M NaCl. Bottom panel: Center of mass frequency shifts of the OH-stretch IR signals.

Overall, the intensity curve shape for LiCl is very similar to that already discussed for NaCl solutions in Figure 21. However, the curves for LiCl are shifted to slightly higher concentrations than those for NaCl. Again, in regime B-D, the intensity decreases with increasing ion concentration while regime A shows inverted concentration dependence. By comparing the two measurement series for NaCl, we find a slightly varying ratio between the maximum intensity and the plateau in regime A and C indicating a small variability of the surface charge on silica, which can likely be traced to slight, unintentional differences in the preparation of the surface.

Besides the shift of the curve toward higher concentration for LiCl compared to NaCl, we observe a steeper intensity increase within regime B-C which suggests that for generating the same screening length, a higher LiCl concentration is required than for NaCl. In other words, Na^+ ions seem to shield surface charges more effectively than Li^+ ions but both are still less efficient than predicted by Equation 35 as shown in Figure 21. Additionally, the intensity plateau within regime C is less pronounced for LiCl than for NaCl. This indicates that the bonded interfacial layer of water gets perturbed and/or replaced more easily by Li^+ than Na^+ ions. In summary, we observe an impact of the ionic radius on the V-SFG intensity curves which seems to be a consequence of a higher screening efficiency for larger cations with equal valence. One explanation may be that alkali ions with larger ionic radii are less hydrated providing higher ion mobility in aqueous media. Consequently, an external field may attract the highly mobile Na^+ ions more easily than Li^+ ions. However, at short distance to the surface, Na^+ seems to show a lower surface propensity than Li^+, as reflected by the OH-stretch V-SFG intensity plateau at high NaCl concentration. Both findings are in line with recent atomic force microscopy studies and molecular dynamics simulations.[89,101]

Second harmonic generation (SHG) spectroscopy has been widely employed for studying the silica/water interface.[14,21–25,92] In contrast to V-SFG, SHG probes a non-linear signal that is not resonantly enhanced and therefore not sensitive to a particular molecule or moiety but may result from any molecular and atomic species present which is in particular relevant for high salt concentrations. Azam et al. have shown that, within regime C, opposed to our V-SFG results, the SHG intensity has inverted concentration dependence for LiCl as compared to NaCl. This observation has been attributed to ion-specific effects on the surface charge.[24] Boamah et al. have demonstrated that for NaCl, the SHG intensity does not drop to zero at high ionic strength and this has been rationalized by assuming either dramatic changes in the surface charge density of silica or in the relative permittivity of water in the diffuse layer.[21] Our data do not show this effect. These comparisons seem to indicate that a direct probe of interfacial molecules or functional groups, as provided with V-SFG, is helpful for understanding the decaying surface potential at charged surfaces in contact with an aqueous solution.

As discussed above, V-SFG seems to provide interfacial layer sensitivity at the silica/water interface for pure water and ~1 M ion concentration. As V-SFG is a resonant probe of vibrational states, here the O-H stretching of interfacial water, the V-SFG spectrum can provide insights into the interfacial interactions through comparison of band frequencies. From the upper panel of Figure 21 it is evident that the O-H stretching band is shifting upon changing the salt concentration. For a quantitative analysis, we calculated the spectral first moment (‘center of mass‘, COM) for the corresponding spectra and compared changes relative to the largest signal (5×10^{-4} and 5×10^{-3} M for NaCl and LiCl, respectively) as depicted in the middle panel of Figure 22.

For all measurement series, we consistently observe an overall red-shifting O-H-stretch V-SFG band upon increasing ion concentration – Figure 22, middle panel. In contrast, corresponding bulk spectra show a blue-shifting O-H-stretch band as illustrated in the lower panel of Figure 22 for IR measurements and reported in Ref. [[102]] for Raman. Therefore, the ion-induced red-shift of the SFG band seems to be a purely surface-related effect. In between these two ionic concentrations at which we measure an SFG response originating purely from the outermost interfacial layer, i.e. pure water and ~1 M electrolyte, we observe a red-shift of about 60 cm^{-1} which suggests that interfacial water in the presence of salt has substantially stronger hydrogen bonds.

3.3 Conclusion

To the best of our knowledge, this work is the first experimental evidence that interference limits the extent to which SFG probes the interface of water in contact with a charged surface such as silica. The maximum SFG signal is generated around millimolar ionic strength which for a 1:1 electrolyte corresponds to a Debye length of tens of nanometers. As a consequence of interference, not only short, but also large Debye lengths, as present for pure water, provide nearly monolayer insight into the interfacial region. The proposed model for the ionic-strength dependent non-linear response from a charged surface, using previously reported surface charge densities for silica and an exponentially decaying surface potential, can be used for describing our SFG data. However, the decay length of the surface potential seems to depend not only on the ion valence: In fact, our data suggest that ions with smaller hydration radii screen surface charges more efficiently, while the Stern layer water is perturbed more easily by ions with larger hydration radii. Irrespective of the ion identity, the O-H stretch SFG band undergoes a redshift with increasing bulk ionic strength as opposed to a blueshift observed for bulk water which indicates that the intermolecular structure of interfacial water at the silica surface changes differently in the presence of salt than what observed in bulk. We interpret the observed red-shift as a strengthening of the interfacial H-bonding structure.

3.4 Further Experimental Details

3.4.1 Spectroscopy

All SFG spectra are recorded in ssp polarization combination (s-polarized SFG, s-polarized visible and p-polarized IR) and at incident angles $\theta_{Vis} \approx 37°$ and $\theta_{IR} \approx 33°$. Each spectrum results from 10-minute accumulation. For normalization, the frequency dependent IR field is measured on an equally prepared silica window, coated with 100 nm chromium-free gold.

The IR data presented in the lower panel of Figure 22 result from ATR measurements accomplished with a Bruker Tensor II (Platinum ATR) and are corrected for the penetration depth in pure water by using the refractive index as reported in Ref. [103].

3.4.2 Sample Preparation

Lithium chloride and sodium chloride, purchased from Sigma Aldrich (≥99.5 %, CAS 7647-14-5) and Roth (≥ 99.5 %, CAS 7447-41-8), respectively, are dissolved in demineralized H_2O, filtered with a Millipore unit (Resistivity = 18 MΩ cm). For removing organic residues, sodium chloride is baked at 650°C for 6 hours. Before each experiment, the (parallel faced) fused silica window (Korth Kristalle GmbH Infrasil® 302, s/d: 60/40) is treated by UV-Ozone cleaning for 30 min. All sample solutions are measured at least one hour after preparation to ensure CO_2-equilibration. Before each measurement, the cell (as detailed in Ref. [40]) is flushed with the sample solution (V_{total} = 100 mL) for 5 minutes (500 mL/min).

3.5 Additional Data

3.5.1 Normalized SFG spectra of water at the silica surface

In the manuscript, we show the raw SFG spectra taken from the silica/water interface. For comparison, Figure 23 presents the same spectra shown in Figure 1, after normalization by the non-resonant signal from a chromium-free gold-coated silica window. The double feature in the O-H stretch region reported previously[91] is reproduced.

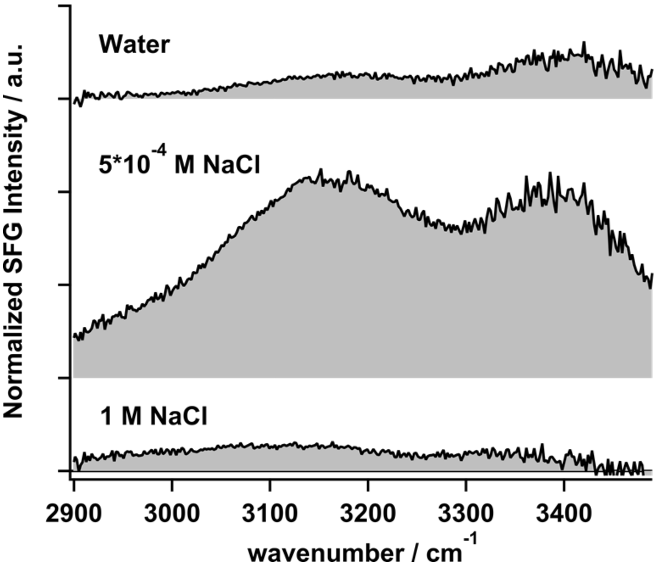

Figure 23: Normalized SFG spectra of the silica/water interface obtained from the raw data shown in Figure 21, normalized by the non-resonant signal from a chromium-free gold-coated silica window

3.5.2 Expression for the potential, Debye length and wave-vector mismatch

Based on the previously reported theoretical model[12], we determined the ratios between the non-linear susceptibilities $\chi^{(3)}/\chi^{(2)}$. For a 1:1 electrolyte solution, the explicit definitions of the surface potential ϕ_0, Debye length κ and wave vector Δk_z are given in equation 36-38.

$$\phi_0(c) = \frac{2k_B T}{e_c}\sinh^{-1}\left(\frac{\sigma_0}{\sqrt{8000 k_B T N_A c \varepsilon_0 \varepsilon_r}}\right) \tag{36}$$

$$\kappa(c) = \sqrt{\frac{2000 e_c^2 N_A c}{\varepsilon_0 \varepsilon_r k_B T}} \tag{37}$$

$$\Delta k_z = \frac{\sqrt{n_{SFG}^2 - \sin^2(\theta_{SFG})}}{\omega_{SFG}} + \frac{\sqrt{n_{VIS}^2 - \sin^2(\theta_{VIS})}}{\omega_{VIS}} + \frac{\sqrt{n_{IR}^2 - \sin^2(\theta_{IR})}}{\omega_{IR}} \tag{38}$$

where k_B is the Boltzmann constant, T the temperature, e_c the elementary charge, σ_0 the surface charge density, N_A Avogadro's number, c the electrolyte concentration, ε_0 the vacuum permittivity, ε_r the relative permittivity of water, n_i the refractive index, ω_i the frequency and θ_i the angle between the beam and the surface normal.

3.5.3 Uncertainty on the non-linear susceptibility ratio

Surface charge densities, σ_0, as reported for silica around neutral pH silica are $-0.06\ C/m^2 < \sigma_0 < -0.02\ C/m^2$.[25,88,90,97,98] Here, we compare the effect of the different values of σ_0 on the shape of the SFG intensity and obtain for the $\chi^{(3)}/\chi^{(2)}$ values ranging from $-22.25\,V^{-1}$ to $-16.50\,V^{-1}$. The resulting curves are shown in Figure 24

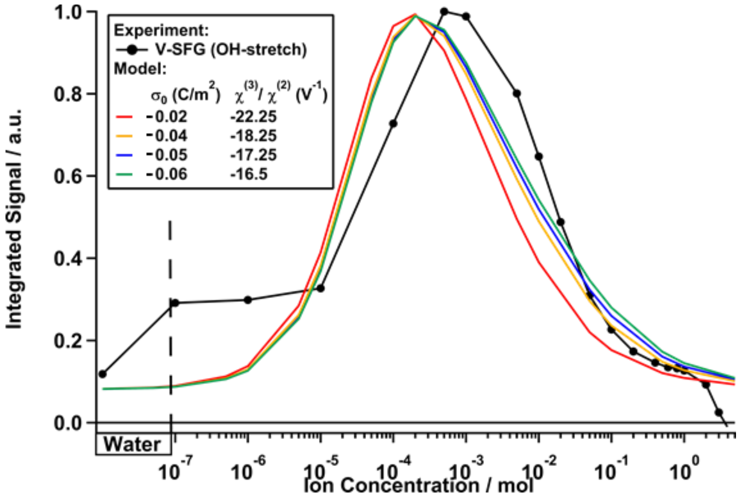

Figure 24: Intensity curves resulting from equation 35, assuming different surface charge densities σ_0 and adjusting the $\chi^{(3)}/\chi^{(2)}$, compared to the experimental data for solutions with varying NaCl concentrations.

4 Understanding dissolution processes from an interfacial perspective

Copyright: This work is based on Jan Schaefer, Ellen H. G. Backus, and Mischa Bonn 2018. Evidence for auto-catalytic mineral dissolution from surface-specific vibrational spectroscopy. *Nature Communications.* 2018 Nature Publishing Group. Open Access as stated under the Creative Commons license: http://creativecommons.org/licenses/by/4.0/

4.1 Introduction

The dissolution of minerals in water is typically studied on macroscopic length- and time-scales, by detecting dissolution products in bulk solution and deducing reaction rates from model assumptions. Here, we report a direct, real-time measurement of silica dissolution, by monitoring how dissolution changes the first few interfacial layers of water in contact with silica, using surface-specific spectroscopy. We obtain direct information on the dissolution kinetics of this geochemically relevant mineral. The interfacial concentration of dissolution products saturates at the level of the solubility limit of silica (~ millimolar) on the surprisingly short timescale of tens of hours. The observed kinetics reveal that the dissolution rate increases substantially with progressing dissolution, suggesting that dissolution is an auto-catalytic process.

Insights into the physicochemical properties of mineral/water interfaces at the molecular level are essential for understanding many of the geological and electrochemical processes on macroscopic scales.[1] For geological questions, it is important to look at these systems under non-equilibrium conditions, as in nature, water is usually not at rest. Typical examples are sea and freshwater dissolving and carrying minerals, which then affects the geology and biology of the environment around it. In this work, we study the dissolution of silica, one of the most abundant minerals on earth, into flowing and resting water.

With bulk experiments,[88,104–106] it has been demonstrated that silica may dissolve up to mM concentration of silica species through hydrolysis reactions with interfacial water, over very long (10’s-100’s of hours) time scales. Very little is known about the dissolution dynamics and how the kinetics affect the structure and composition of the silica/water interface including its physical properties such as the surface charge density, the Debye length, and corresponding surface potential. While silica/water has been studied extensively under static conditions by employing non-linear spectroscopy techniques[5–18], potentiometric titration,[87,88] Atomic Force Microscopy[89], and X-ray Photoelectron Spectroscopy[11,90], non-equilibrium insights are scarce[39,40].

Here, we employ vibrational sum frequency generation (V-SFG) spectroscopy, a sub-μm surface-sensitive, and chemically selective technique. We use the vibrational response associated with the O-H stretching mode of H-bonded water at ~3200 cm^{-1}, to monitor the dissolution kinetics at the silica/water interface. The V-SFG water signal reflects the broken symmetry at the interface: Specifically for water near charged interfaces, the surface charge serves to align the water molecules, thereby breaking the symmetry and making the water molecules SFG active. The z-dependent surface potential itself also breaks the symmetry, giving rise to a potential signal from the near-surface region, corresponding to the Debye length, with z being the coordinate along the surface normal. As such, the V-SFG interfacial water signal reflects both the surface charge and the extent to which that surface charge is screened by counterions at the surface. We find that equilibration of the silica surface in contact with bulk water occurs on a timescale of several tens of hours, resulting in a steady state interfacial concentration of ionic dissolution products corresponding to an ionic strength of ~1-10 mM. The dissolution process appears auto-catalytic.

4.2 Results and Discussion

Dissolution of silica changes the ionic strength of interfacial water since some of its dissolution products are known to be charged. Monosilicic acid, for example, may mainly exist as an over-protonated (i.e., positively charged) species at neutral pH.[106] Therefore, dissolution may cause changes in the surface charge of silica as well as the screening of that charge by nearby ions, i.e., the Debye length. The SFG O-H stretch signal is known to be a sensitive reporter of both, the surface charge and the Debye length, as explained in detail in ref. [16] (chapter 3) and illustrated in Figure 25. In ref [16], it is shown that the SFG intensity variation with ionic strength of NaCl can be accounted for by invoking only screening and assuming $\chi^{(2)}$ as well as the surface charge, primarily determined by the local pH,[25] to be constant.[16] Figure 25 reveals a maximum in the SFG signal as a function of ionic strength (NaCl), around 1 mM. This maximum originates from an interplay between screening effects lowering the signal at higher concentrations (regions ii-iv) and interference effects, lowering the signal at lower concentrations (region i).[16] There are also subtle differences in the spectral shape of the response, discussed in chapter 4.5.1 and in ref. [16], not relevant to the discussion here.

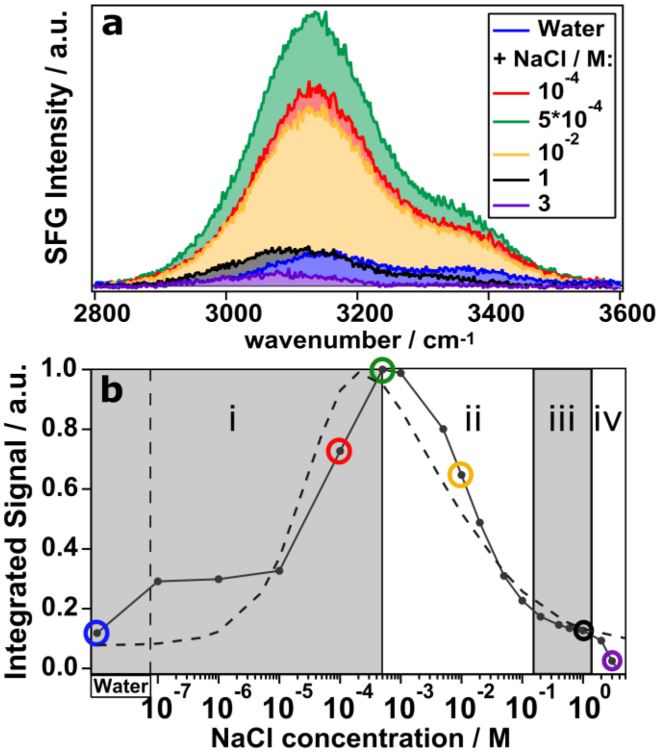

Figure 25: a O-H-stretch SFG-signal for various NaCl solutions (Ref: [16]); b SFG signal intensities, integrated from 2800 to 3600 cm-1 and normalized to the curve maximum. The spectra corresponding to the marked data points are presented in the top panel, with corresponding colors. All spectra are measured under resting conditions, directly after flowing for 5 minutes. Dashed line: The predicted intensity variation by invoking modulation by charge screening and interference, at constant $\chi(2)$ and constant surface charge density, as detailed in ref. [16].

Here, we use the known correlation between the near-surface charge distribution and the SFG signal for studying the dissolution of silica at the silica/water interface. For doing so, we monitor the O-H stretch V-SFG signal as a function of time after bringing the silica surface in contact with water. By applying flow, i.e., replacing the water in the interfacial region by bulk solution, the interfacial ionic strength becomes dominated by the bulk electrolyte concentration. Through comparison of pure water with various NaCl solutions under resting and flowing conditions, we obtain new insights into the dissolution process at the silica/water interface by quantifying the time-dependent dissolution-generated interfacial ionic strength. For quantification, we need to find the concentration above which we do not observe any signal changes upon flow, which means that the ionic strength of dissolved silica matches or is overwhelmed by the bulk NaCl concentration.

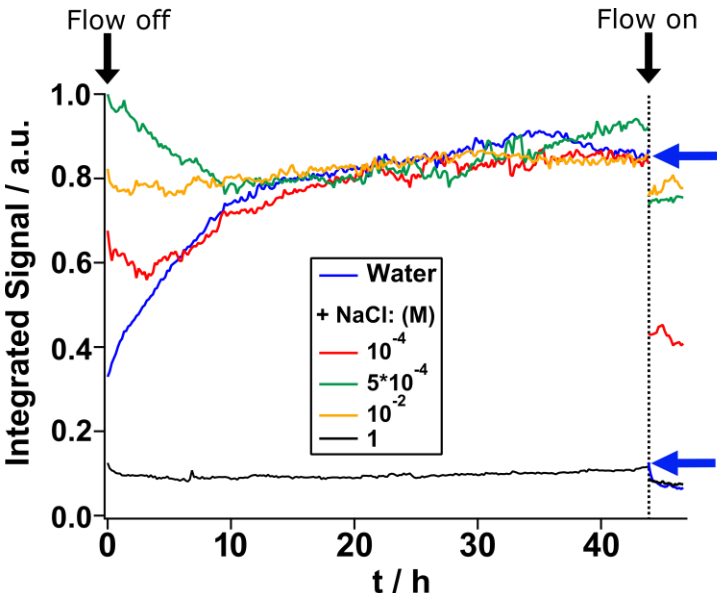

Figure 26: Kinetics of the O-H-stretch SFG-signal from the silica/water interface at different sodium chloride bulk concentrations under resting ("Flow off") and flowing ("Flow on") conditions.

The time-dependent V-SFG responses for pure water, 10^{-4}, $5*10^{-4}$, 10^{-2} and 1 M NaCl aqueous solution are presented in Figure 26. Similar to Figure 25, the V-SFG signals are analyzed by signal area. Overall, we observe that under flow-off conditions, the signal traces for all solutions up to a NaCl concentration of 10 mM converge to the same SFG intensity, which is close to the intensity observed for the 10 mM solution under flow-perturbed conditions. Without invoking any model, this directly indicates that dissolution of silica changes the z-dependent electrostatic potential of the bare silica/water interface to a very similar degree as the addition of approximately 10 mM of NaCl, implying an interfacial concentration of dissolution-released ions of that same order. A spectral analysis of the signals supports the conclusion that the dissolution products in this concentration range screen the surface charge. The spectral shift of the O-H band corresponds quantitatively to that observed previously between pure water and a salt solution (NaCl) in the millimolar concentration range (detailed in chapter 4.5.1).[16] As mentioned above, the associated SFG intensity variation of those NaCl solutions can be accounted for by just invoking a concentration-dependent Debye screening length, keeping $\chi^{(2)}$ and the surface charge density constant (Figure 25, dashed line).[16] This suggests that the intensity change, also along dissolution, primarily results from variation in charge screening. However, we cannot exclude an additional contribution from changes in the surface charge, as indicated in previous work using a different, more surface-specific, experimental geometry.[40]

For silica in contact with pure water, the O-H-stretch SFG-signal rises to the equilibrated level within a timescale of ~ one day (blue trace in Figure 26). Upon turning on the flow at t = 45 h, i.e., by exchanging the interfacial solution with pure water, a rapid (< 10 min) intensity drop of about one order of magnitude is observed (blue arrows in Figure 26). Under resting conditions, dissolving silica generates substantial interfacial ionic strength as reflected by the intensity changes, equivalent to going from the low-concentration (left) end of the trace in Figure25 to the peak of the signal at ~1 mM.

For 10^{-4} and $5*10^{-4}$ M NaCl solutions, the signals initially decrease within the first 5 and 10 hours, respectively. Afterward, both traces follow the kinetics as observed for pure water. Hence, at later times, the ionic strength of the interfacial region is dominated by dissolved silica species whereas the initial decrease can only be ascribed to a process involving NaCl since it does not appear for pure water. One scenario is that at early times (t < 10 h), dissolving silicic acid molecules replace Na^+ and Cl^- ions from the interface. In line with this hypothesis is the previous observation that ions with equal valence but larger hydrated radii (here: silicic acid vs. Na^+ / Cl^- ions) screen surface charges less efficiently.[16] While less screening usually corresponds to a higher SFG signal, solutions with sub-mM ionic strength show opposite behavior as demonstrated in Figure 25. In this concentration regime, a decrease of the SFG response reflects an increase of the penetration depth of the surface electric field as a result of reduced charge screening.[12,16] Upon flow, i.e., mixing the interfacial region with a bulk electrolyte solution, the SFG signals drop according to the bulk ionic strength of the corresponding solution, similar to what is observed for pure water.

For 10^{-2} M and 1 M NaCl, the signal strengths are very different, but in both cases, no substantial intensity change occurs within 45 h of equilibration which means that the screening length, determined by the interfacial ionic strength, in both cases is dominated by the NaCl content in the bulk solution. However, under flow conditions, a small intensity drop can still be observed for both solutions. One explanation could be that application of flow does not only mix interfacial with bulk solution, but may also slightly alter the effective surface charge density of silica.[40]

As summarized in Figure 27, the differences between equilibrium and the flow-perturbed steady states increase with decreasing electrolyte concentration. This observation is consistent with the notion that the intensity rise during equilibration can be ascribed to a local increase of ionic concentration close to the silica surface. Under flow conditions, the local ionic strength at the surface is decreased if the equilibrium concentration of silicic acid exceeds the bulk ionic concentration. For increasing bulk ionic concentration, the removal of dissolved silica is compensated by adsorption of ions provided by the bulk solution, effectively decreasing the difference in signal intensity along equilibration and under flow conditions.

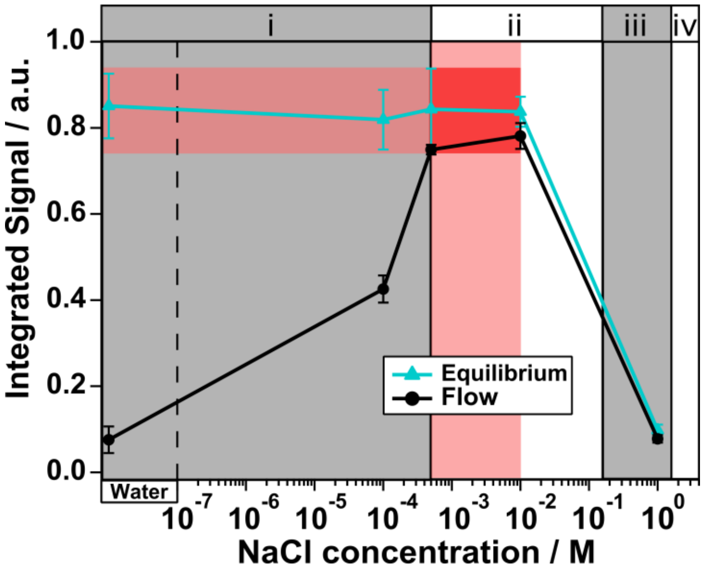

Figure 27: Integrated O-H-stretch SFG signal of the silica/water interface at equilibrium (t > 12 h) and under flow conditions with different bulk sodium chloride concentrations. The error bars represent the 2σ variation from the corresponding average value.

It is apparent from these measurements that the V-SFG intensity of the nominally pure water sample under equilibrated conditions is equal to the intensities observed for the solutions with bulk NaCl concentrations between $5{*}10^{-4}$ and 10^{-2} M which is very similar to the solubility limit of silicic acid.[88,104,106] Apparently, the interfacial ionic strength, generated by silica dissolution, reaches a steady state within this concentration range. In contrast to the bulk solutions of high-surface-area silica, for which it is known to take roughly two weeks to achieve saturation with silicic acid,[106] our results show that the interfacial region is already saturated after one day. This observation suggests that diffusion limits dissolution of silica in contact with resting water.

A quantitative picture of the interfacial kinetics can be obtained by invoking a simple 1D dissolution rate model that considers only one type of silica species, being either bound to the solid or dissolved in water and getting displaced by diffusion with the corresponding overall forward and backward rates k_f, k_b and the diffusion coefficient $\left(D\right)$. Equations 39-40 provide the expressions for the corresponding interfacial and diffusive flux. The interfacial flux $\left(J_{in}\right)$ depends on k_f, k_b and the interfacial concentration of dissolved species

(c). The diffusive flux $\left(J_{diff}\right)$ depends on D and the concentration gradient orthogonal to the surface plane.

$$J_{in} = k_f - k_b c \tag{39}$$

$$J_{diff} = \frac{\partial c}{\partial t} = D\frac{\partial^2 c}{\partial z^2} \tag{40}$$

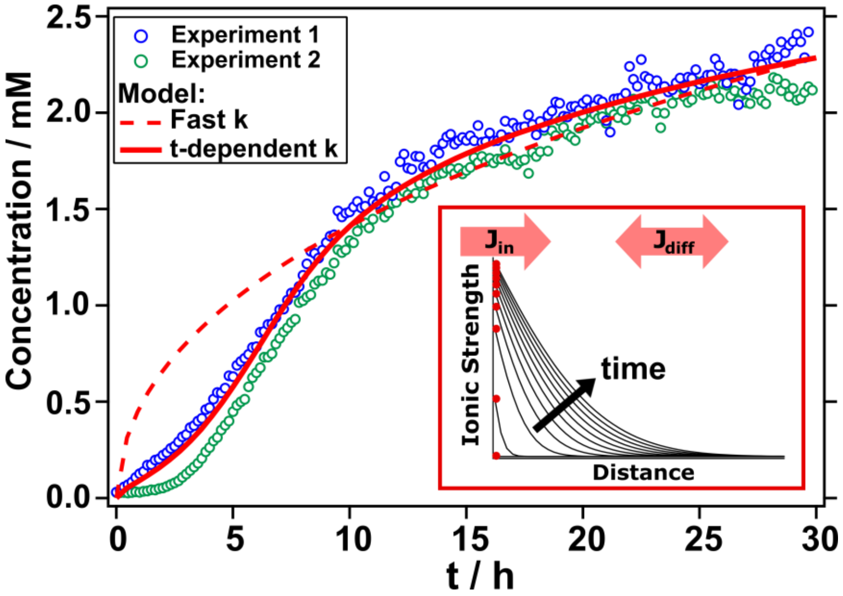

Figure 28: The time trace of the O-H-stretch SFG-signal from the silica/water interface for pure water converted into an interfacial ionic strength (circles) by using the conversion function detailed in Supplementary Figure 26. For comparison, the interfacial ionic strength as predicted by a simple 1D dissolution/diffusion model (red lines). Inset: A schematic plot of the concentration gradient perpendicular to the surface plane resulting from the model, plotted at equally distant times. The red dots represent the evolution of the interfacial ionic strength (average value of the first 1 µm).

The rate model results plotted in Figure 28 present the temporal change of the ionic strength within the first micrometer from the interface and the spatial gradient orthogonal to the surface plane (see inset). The main plot compares the temporal change of the interfacial concentration as resulting from the model (red lines) with two experimental time traces for nominally pure water (blue and green). The experimental concentration is inferred from the integrated O-H stretch V-SFG signal, converted by a function that resembles the low concentration intensity-curve shape (detailed in chapter 4.5.2).

By using rates on the order of magnitude as reported in the literature, $k_f = 2.25*10^{-12}\,mol\ m^{-2}s^{-1}$,[106–109], $k_b = 1.90*10^{-10}\,s^{-1}$,[105], $D = 8.50*10^{-10}\,m^2 s^{-1}$,[110], the model does not result in an interfacial ionic strength on the millimolar range. This demonstrates that these dissolution rates, deduced from bulk experiments, only yield an accurate description of the dissolution process under continuous mixing, while it poorly describes the actual reaction, that is, under resting conditions. For yielding a millimolar concentration on the timescale of a few hours (red dashed line), the rates have to be adjusted substantially, either by accelerating the dissolution ($k_f = 2.40*10^{-10} mol\, m^{-2} s^{-1}$, $k_b = 4.72*10^{-8} s^{-1}$) or by slowing down the diffusion ($D = 9.50*10^{-14} m^2 s^{-1}$). However, neither adjustment yields the correct shape of the experimental traces that show a slow response at early times (t < 5 h), followed by an accelerated concentration increase (5 h < t < 10 h) and saturation at late times (t > 10 h). The observation of a lag time for the interfacial concentration to start changing, unambiguously shows that there is a time-dependent contribution to the dissolution process, which is missed in bulk experiments.[106–109] Potentially, this may arise from a time-dependent diffusion coefficient as detailed in chapter 4.5.3. A physically more compelling interpretation is a time-dependence of the reaction rate, discussed in the following.

The S-type experimental response can be understood by considering a reaction pathway that allows for a self-accelerating dissolution process of silica, namely hydrolysis with hydroxide ions. Hydroxide ions are released during the reaction, and the dissolution rate has previously been reported to increase at elevated pH.[106]

$$\equiv Si-O-Si(OH)_3 + OH^- \rightleftharpoons \equiv Si-O-Si(OH)_2 O^- + H_2O \tag{41}$$

$$\equiv Si-O-Si(OH)_2 O^- + OH^- \rightleftharpoons \equiv Si-O^- + Si(OH)_3 O^- \tag{42}$$

At neutral to slightly acidic pH, dissolved silicic acid mainly exists as an over-protonated species which returns two hydroxides.[106]

$$Si(OH)_3 O^- + 2\, H_2O \rightleftharpoons Si(OH)_4 H^+ + 2\, OH^- \tag{43}$$

Given that (de-)protonation occurs on a much faster timescale than dissolution, the hydrolysis is the rate-limiting step and determines the overall rate. At the same time, protonation of each dissolved silicic acid molecule returns two hydroxides that catalyze dissolution of the subsequent layer. As summarized schematically in Figure 29, the dissolution of silicic acid thus is an auto-catalyzed process that accelerates as the dissolution proceeds. We performed a control experiment with a pH 9 aqueous solution of NaOH (chapter 4.5.4). In line with dissolution being an autocatalytic process, with hydroxyl ions being the key reactant, we observe that the kinetics speed up by over an order of magnitude: from a tens of hours timescale to a 1-2-hour timescale under basic conditions. This observation supports the notion of autocatalytic, hydroxide-driven dissolution of silica.

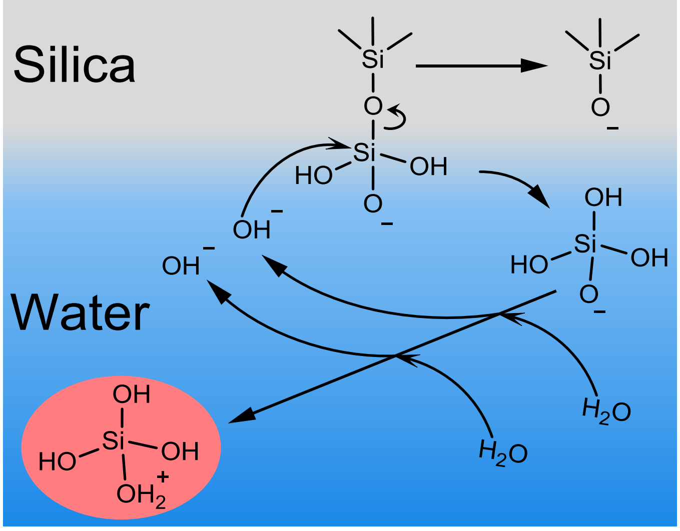

Figure 29: Proposed dissolution mechanism of silica in water considering hydrolysis with hydroxide ions. With each reaction cycle, protonation of the dissolved silicic acid molecule releases two hydroxide ions, close to the surface which are mostly consumed by the hydrolysis reaction, giving rise to an auto-catalytic process.

In this scenario, the overall rate largely depends on where, relative to the surface, the dissolved silicic acid molecules protonate, determining the local concentration of hydroxides, which induce deprotonation and dissolution of the subsequent surface layer. With increasing number of hydroxides present at the surface, the rate will increase. Invoking a linear increase of k_f with time (from $k_{f,0h} = 1.01*10^{-12}$ to $k_{f,8.5h} = 3.69*10^{-10}$, detailed in chapter 4.5.5), the model yields the S-type curve shape (solid red line in Figure 28) as observed experimentally.

4.3 Conclusion

In conclusion, we have experimentally demonstrated that silica equilibrates roughly at a millimolar of ionic strength at the interface with pure water. This interfacial equilibration takes tens of hours, not weeks as concluded from bulk experiments with high surface area silica, suggesting that the overall dissolution process of silica is limited by diffusion. This is supported by the fact that mixing, as often done in those bulk experiments and accomplished here by applying flow, rapidly ($t < 10$ min) yields a steady state in which dissolution products are instantaneously removed from the very first interfacial layers probed in our experiments.

By comparison with a 1D reaction-diffusion model, we show that dissolution rates and a diffusion coefficient reported for bulk dissolution of silica do not yield sufficiently high equilibrium interfacial ionic strength as observed in our experiments, at least within the timescale of hours. The experimentally observed S-shaped kinetic curve directly shows that the dissolution rate of silica increases with time, suggesting an auto-catalyzed mechanism.

4.4 Further Experimental Details

4.4.1 Sum Frequency Generation Spectroscopy

All SFG spectra were measured with ssp polarization combination (s-polarized SFG, s-polarized visible and p-polarized IR). To check laser stability during the experiment, part of the IR beam was split off to monitor its power. A typical time trace is plotted in chapter 4.5.6, showing a variation of less than 5%.

4.4.2 Sample preparation

Sodium chloride, purchased from Sigma Aldrich (Z99.5%, CAS 7647-14-5), was baked at 650 °C for 6 hours to remove organic residues and dissolved in demineralized H_2O, filtered with a Millipore unit (resistivity = 18 MΩ cm). Before each experiment series, the (parallel faced) fused silica window (Korth Kristalle GmbH Infrasil 302, s/d: 60/40) was treated by UV-Ozone cleaning for 30 min. To ensure CO_2-equilibration, all sample solutions were measured at least one hour after preparation. Before each measurement, the cell (introduced in ref. [40]) was flushed with the sample solution (V_{total} = 250 mL) for 5 minutes (500 mL min^{-1}). The same flow rate was used for carrying out the flow-perturbed experiments.

4.4.3 Model

The 1D reaction/diffusion model was implemented by employing the built-in MATLAB (R2017a) scheme *pdepe*.

4.5 Additional Data

4.5.1 Center of mass frequency shift along dissolution

As illustrated in Figure 30, not only the SFG intensity-change along dissolution matches with that of a ~millimolar NaCl solution compared to pure water but also its corresponding frequency shift (blue double arrows). This supports our conclusion that roughly a millimole of ionic strength is generated at the interface due to dissolution of silica.

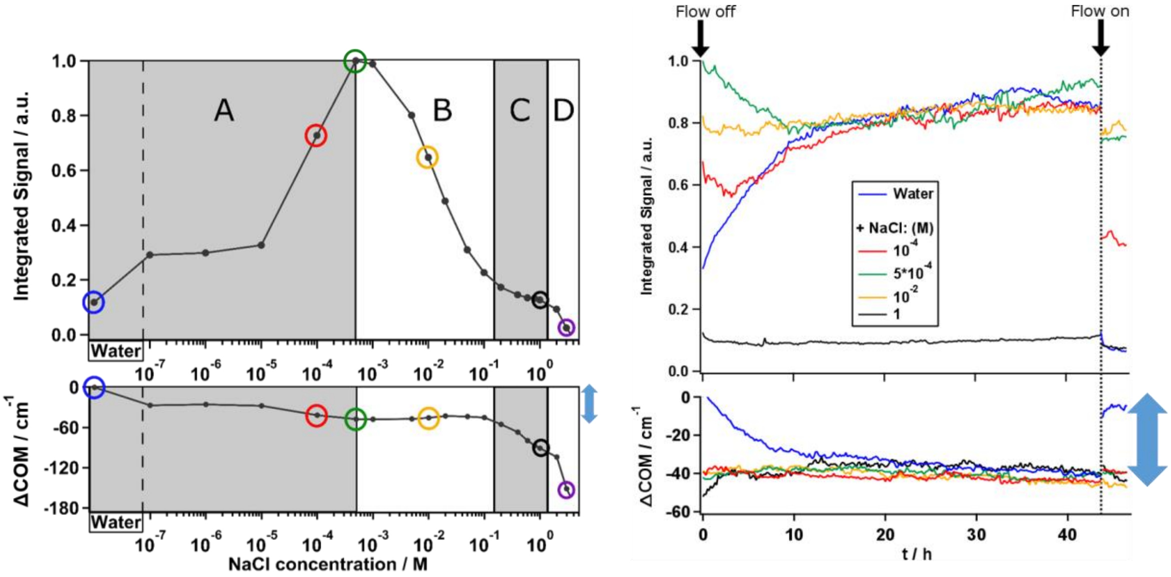

Figure 30: Integrated SFG signal presented in Figure 25 and 26, together with its center of mass frequency shift with respect to the center of mass frequency of pure water at the silica surface. The blue double arrows mark the shifts along dissolution (right) and its corresponding shift resulting from the addition of NaCl to the solution (left)

4.5.2 Conversion function between the SFG signal and interfacial ionic strength

In order to convert the experimental SFG data into an interfacial ionic concentration in Figure 28, we employ the function presented in Figure 31 (green), that is:

$$Signal = \frac{-1}{\log(30 * concentration)} \tag{44}$$

The curvature of the required function (green) is adjusted according to the concentration-dependent SFG intensity curve (black) in Figure 27 and is presented below in Figure 31.

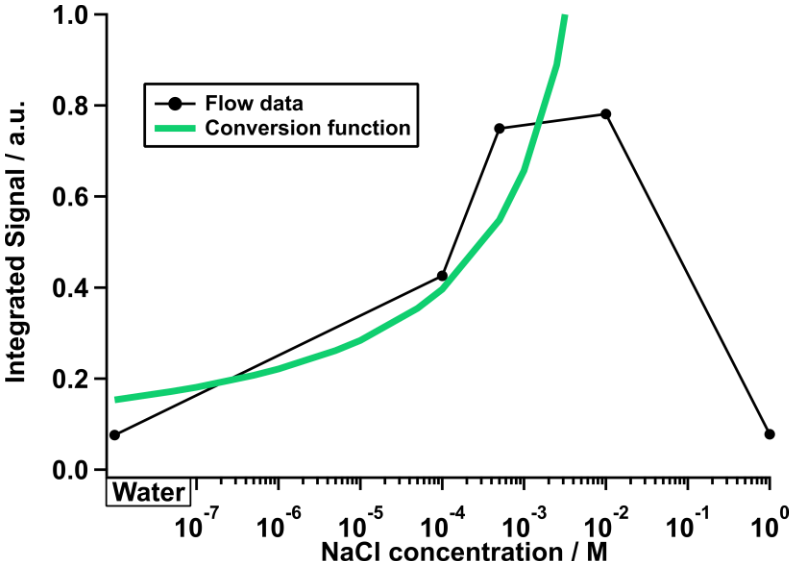

Figure 31: The function employed for conversion of the experimental SFG data into an interfacial concentration (depicted in Figure 28). For comparison, the flow data presented in Figure 27 are plotted as well.

4.5.3 Time-dependent diffusion coefficient

Figure 32 presents the time-dependent diffusion coefficient that gives a very similar match of the dissolution model with the experimental data presented in Figure 28 as the invoked time-dependent dissolution rate.

$$D = 10^{-11} * e^{\left(\frac{-t}{5000}\right)} + 9.5 * 10^{-14} m^2 s^{-1} \tag{45}$$

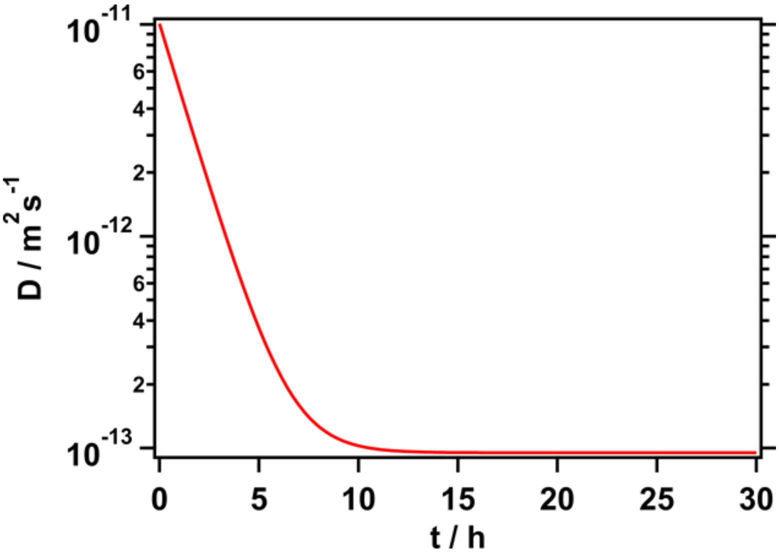

Figure 32: Time-dependent diffusion coefficient vs. time.

4.5.4 Dissolution kinetics at pH 9

To confirm the autocatalytic mechanism of silica dissolution, mediated by hydroxide, Figure 33 shows the dissolution experiment for a pH 9 aqueous solution of NaOH. We observe that the kinetics speed up by over an order of magnitude compared to the experiment at neutral pH: from a tens of hours timescale to a 1-2-hour timescale under basic conditions.

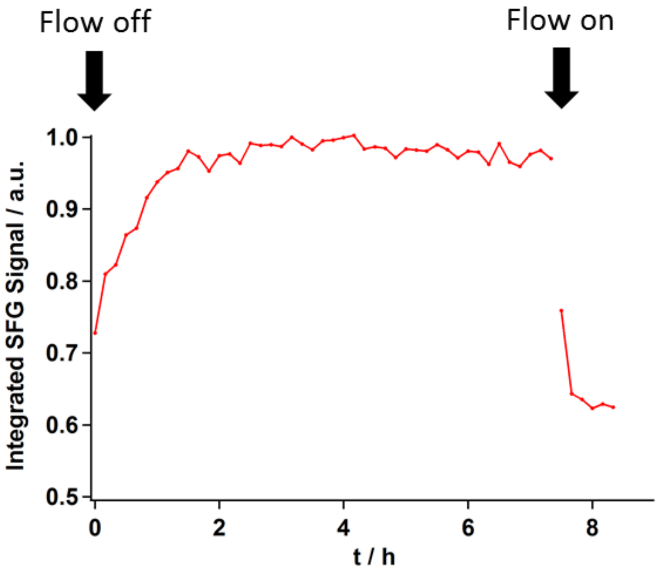

Figure 33: Integrated SFG signal of the silica / water interface as a function of time for a pH 9 aqueous NaOH solution

4.5.5 Time-dependent dissolution rate

For the time-dependent dissolution rate invoked in Figure 28 (red solid line), the following functional is used:

$$k^{-1} = 8.82 * 10^{-8} s^{-1} \tag{46}$$

$$k = \begin{cases} t * 1.20 * 10^{-14} + 10^{-12} mol m^{-2} s^{-1}, t < 8.5h \\ 30600 * 1.20 * 10^{-14} + 10^{-12} mol m^{-2} s^{-1}, t > 8.5h \end{cases} \tag{47}$$

A graphical illustration is depicted in Figure 34.

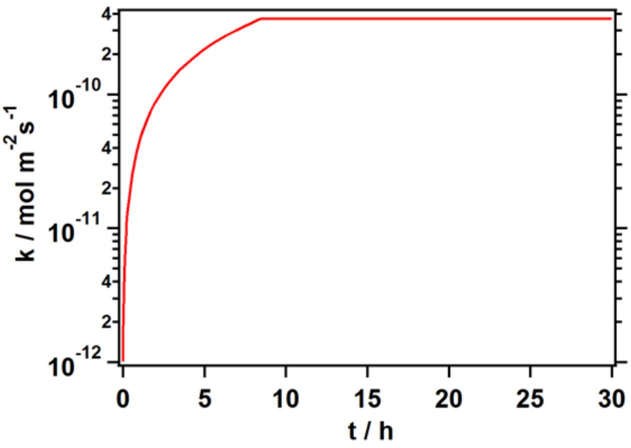

Figure 34: Time-dependent forward rate vs time.

4.5.6 Stability of the IR power

As introduced in the main text, part of the IR beam was separated for monitoring its stability. In Figure 35, a typical time trace (bottom panel) is plotted together with the time trace for the experiment with pure water presented in Figure 26 (top panel). The plot shows IR power variation of less than 5% along the experiment.

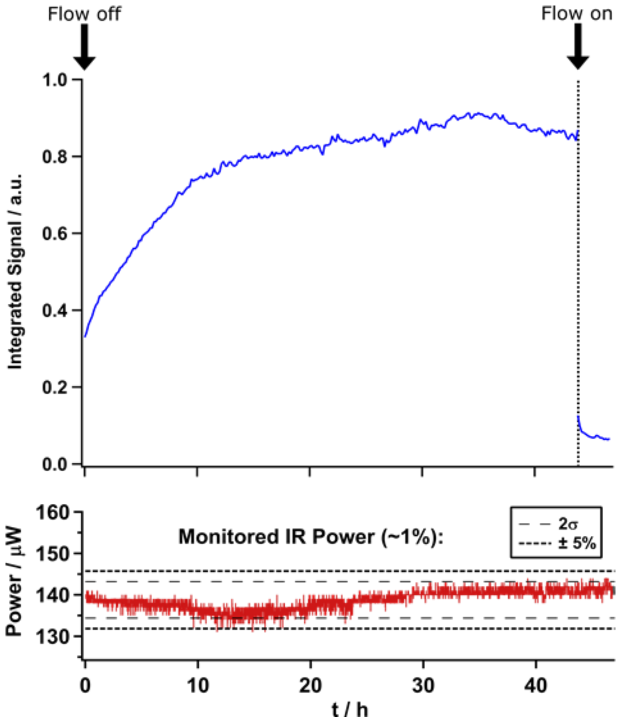

Figure 35: IR Power stability during experimental conditions. Top: The experiment with pure water presented in Figure 26. Bottom: The corresponding IR Power stability along this experiment.

5 Specific ion-dependent crowding at a charged mineral/water interface

Acknowledgment: Dr. Johannes Hunger's contribution was the elaboration and analysis of the modified Poisson-Boltzmann calculations. The Gouy-Chapman-based SFG model was developed by Dr. Grazia Gonella. Leon Prädel and Patrick Ober performed some of the SFG measurements. My contribution to this work was the acquisition of the SFG spectra and the analysis thereof.

5.1 Introduction

The collective behavior of dissolved ions with respect to a charged surface is a fundamental problem for understanding solid/liquid interfaces in a geological or electrochemical context. It is well understood that charged surfaces when being in contact with an electrolyte solution get screened by the ions, in particular by counterions that accumulate close to the surface. As a consequence, the surface potential associated with the surface charge decays along the surface normal. Commonly, the ion-enriched near-surface region is referred to as the so-called Electric Double Layer (EDL) that is often described by versions of the Gouy-Chapman model. This model assumes a Poisson-Boltzmann distribution of ions described as point charges. By employing vibrational SFG spectroscopy, we demonstrate that, for alkali halides at the silica/water interface, the decay of the surface potential is strongly affected by the cation size. Comparison with a modified Poisson-Boltzmann calculation employing polarizable ions, further indicates that the ion-size-dependence is related to the interfacial ion distributions arising from different net hydration radii.

The silica/water interface has been studied extensively as a prototypical mineral interface with surface specific spectroscopic techniques such as X-ray photoelectron spectroscopy (XPS)[11,90,100] and non-linear spectroscopy like Second Harmonic Generation (SHG),[14,21–25] and Sum Frequency Generation (SFG)[16–18,20,26–29,31] spectroscopy. Both methods have provided detailed insights into the microscopic nature of that interface. For example, pH-dependent studies have revealed that the negative surface charge of silica results from deprotonation of 2-3 types of silanol groups with different acidity. Additionally, it has been demonstrated that the total acidity of the surface depends on the cation as well as the anion species and the concentration of the background electrolyte.[22–25] Phase-resolved SFG studies have indicated that the EDL is composed of differently net oriented water species.[20,27] For neutral pH, it has been shown that the 2nd order non-linear response of water at the silica surface is highly dependent on the ionic strength of the solution.[15–18,21] Qualitatively, this dependence has been rationalized with the Gouy-Chapman description of the surface potential decay within the EDL.[12,16,21] However, dramatic changes of the interfacial permittivity had to be invoked to yield quantitative agreement with that model.[21] Previous work has indicated that not only the topmost layers,[19,20,27] but also the overall screening efficiency of electrolytes in contact with silica is dependent on the ion size.[16] Here, we present a systematic study on how the different sized ions alter the EDL composition and the decaying surface potential associated with it. By interrogating the concentration-dependence in the SFG response for different alkali halides, we demonstrate that the ion-specific surface propensity has implications for the entire EDL, with a seeming effect on length scales that are commonly considered to be ion-unspecific.

5.2 Results and Discussion

In general, the total SFG response of water in front of a charged surface can be disentangled into $\chi^{(2)}$ and $\chi^{(3)}$ contributions,[13,14,96] which essentially report on the Stern (SL) and Diffuse (DL) layers, respectively. Roughly speaking, the DL contribution becomes more important with decreasing salt concentration since the surface charges get decreasingly screened which results in larger decaying lengths of the surface electric field (E_{DC}). The SFG intensity can be approximated as a sum of contributions from the Stern and Diffuse layers:

$$I\left(SFG\right) \propto \left| E_{VIS} E_{IR} \chi^{(2)} + \int_{0}^{+\infty} E_{VIS} E_{IR} E_{DC}\left(z\right) \chi^{(3)} dz \right|^{2} \tag{48}$$

Figure 36 shows the integrated O-H stretch SFG response of H-bonded water in front of a silica surface for a dilution series of lithium, sodium, potassium and cesium chlorides. In line with previous work,[16] we observe an increase of the SFG signal with increasing salt content at low concentration and an inverse behavior at high concentration, giving rise to a maximum SFG signal in the millimolar range. While the trend at high ion concentration has been rationalized by only invoking Debye charge screening, the low concentration part of the intensity curve has been shown to result from a convolution of screening and optical interference.[12,16] Here, we observe that with increasing the ionic radius of the electrolyte, i.e., $Li^+ < Na^+ < K^+ < Cs^+$, the maximum of the SFG intensity curve shifts towards lower concentration (from 5 mM to 0.5 mM). Also, the magnitude of that SFG intensity maximum decreases along this series by a factor of two. Without invoking any model, this finding indicates that ions with larger ionic radii screen the surface charges more efficiently, i.e., Cs^+ has the highest screening efficiency within this series. Since these ions are equally charged, this implies an ion-size dependent interfacial ion distribution with Cs^+ having the highest surface propensity within this series.

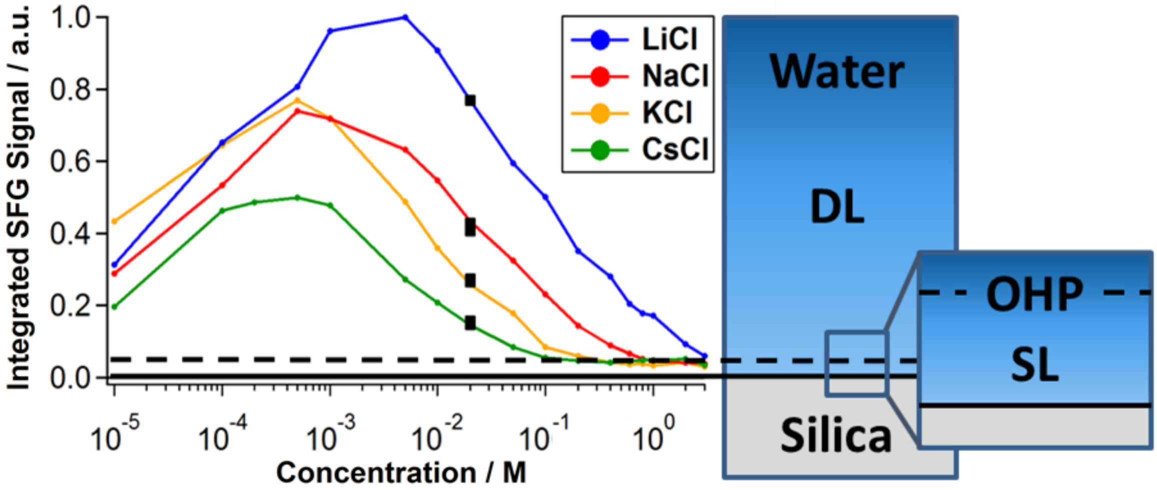

Figure 36: Integrated (ssp) SFG response of the H-bonded O-H-stretch vibration at the silica/water interface with varying salt concentration using different alkali chlorides: LiCl (blue), NaCl (red), KCl (orange) and CsCl (green). The black squares represent the intensity calibration of the curves. The dashed line marks the plateau at high concentration, interpreted to report mostly on the Stern Layer response.

It has previously been reported that at very high concentration (molar regime), the SFG intensity becomes insensitive to varying the ion concentration which gives rise to a plateau in the SFG intensity curve.[16] The plateau has been assigned to be dominated by the neat $\chi^{(2)}$ response reporting mostly on the SL as opposed to the $\chi^{(3)}$-dominated regime at lower concentration which reflect the DL contributions.[16] This has been rationalized with the notion that at this high concentration, the interface is saturated with counterions, which gives rise to a vanishing DL. Here, we observe that the magnitude of the SL response, marked as a dashed line in Figure 36, is very similar for the different alkali salts and thus seems to be independent of the cation size. This suggests that the combination of net orientation and number of water molecules in the SL is independent of the cation species that are condensed on the Outer Helmholtz Plane (OHP, the border between SL and DL). However, the concentration range along which this plateau appears differs substantially for these alkali ions. While the neat SL response is reached for LiCl only at 3 M, it extends to about

1 M for NaCl and even 0.1 M for CsCl. This means that with increasing ion size, lower bulk electrolyte concentration is required to screen the surface potential within the SL. In other words, at equal bulk concentration, larger ions such as Cs^+ seem to yield a higher local concentration at the OHP than smaller ions (e.g., Li^+). As a consequence, the interfacial ion concentration seems to be determined not only by the bulk ion concentration and the net charge (surface charge + dissolved ions) but also critically depends on the ion size as this is what seems to limit the ion distribution in the Stern Layer region.

pH-dependent SHG measurements of the same system, have suggested that at high background electrolyte concentration ($c \geq 100$ mM), the anion species has a more dramatic impact on the silica surface charge distribution than the cation species.[23,24] As presented in Figure 37, we find that the concentration-dependent SFG curve for NaCl is invariant to increasing the anion size from chloride to iodide. In line with our notion presented above, this suggests that screening of the negatively charged silica surface is dominated by the cation properties. Another pH-dependent SFG study of solutions with high electrolyte concentration has suggested that the O-H stretch response is a direct reporter on the surface charge when probed under pss polarization combination due to a much higher surface-specificity than for ssp.[28,29] Here, we find for NaCl that employing pss instead of ssp gives rise to a 3-times lower response over the whole concentration range. The shape of the SFG curve is however not affected by changing the polarization combination. We conclude that for dilute solutions, pss is not more surface-specific than ssp. Additionally, this finding suggests that the concentration-dependent SFG response is not arising from orientational effects of water, at least in case of NaCl.

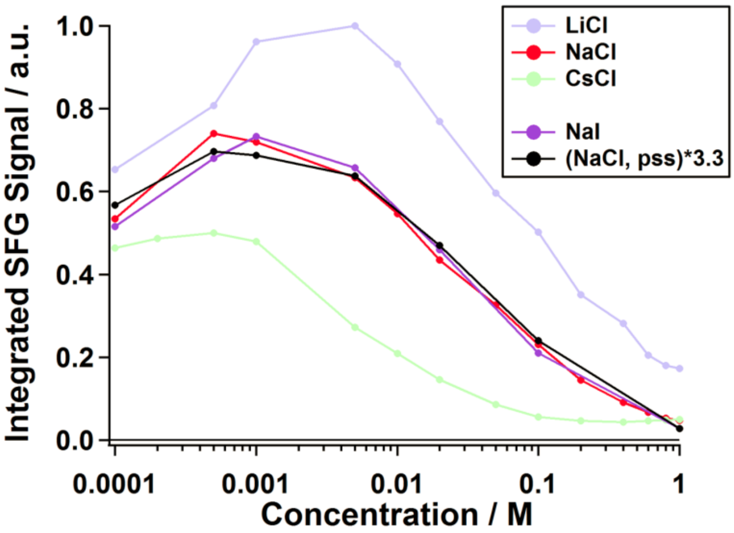

Figure 37: Integrated SFG response of the H-bonded O-H-stretch vibration at the silica/water interface with varying salt concentration with a different anion species (NaI, ssp; purple) or measured under different polarization combination (NaCl, pss; black). The pss data are scaled by a factor of 3.3. As reference, the (ssp) results for LiCl (pale blue), NaCl (red)and CsCl (pale green) from Figure 36 are plotted as well.

To understand the ion-specific impact on the Stern and Diffuse Layer on a more quantitative level, we will now employ the previously proposed Gouy-Chapman-based model to predict the non-linear response of charged interfaces.[12] This model invokes an intrinsic $\chi^{(2)}$ response of the interface and also a $\chi^{(3)}$ response that accounts for the electric-field-dependent contribution of the more outer layers. A detailed introduction is provided in chapter 1.

$$I(SFG) \propto \left| E_{VIS} E_{IR} \left(\chi^{(2)} + \chi^{(3)} \int_{0}^{+\infty} E_{DC}(z) e^{i\Delta k_z z} dz \right) \right|^2 \tag{49}$$

$$I(SFG) \propto \left| E_{VIS} E_{IR} \left(\chi^{(2)} + \chi^{(3)} \phi_d(c) \frac{\kappa(c)}{\kappa(c) - i\Delta k_z} \right) \right|^2 \tag{50}$$

As resulting from equation 48-50, the SFG signal can theoretically be disentangled into the intrinsic and field-dependent contributions that, roughly speaking, reflect the SL and DL, respectively. The SFG response can, therefore, in principle be used to access the entire EDL by tuning the ion concentration: From the interfacial water structure reflected by $\chi^{(2)}$ to the SL potential ϕ_d and the Debye screening length κ^{-1} of that potential, both contained in the $\chi^{(3)}$ term. Additionally, this 3rd order contribution includes an interference term, which accounts for the coherence length of the generated SFG light $\left(i\Delta k_z\right)$ and may be used as an internal standard for the Debye length.

For deducing physically relevant properties from the experimentally observed SFG intensity curves, we employed the above-mentioned theoretical framework, to describe the two most different curves (i.e., LiCl vs. CsCl) as presented in Figure 38. For illustrative purpose, we used one fixed pair of $\chi^{(2)}$ and $\chi^{(3)}$ for both salts, since the $\chi^{(2)}$ plateau inferred from Figure 36 is very similar for the different salts and, in the model, $\chi^{(3)}$ just acts as a scaling factor on the Stern potential. Keeping $\chi^{(2)}$ and $\chi^{(3)}$ constant, we adjust the Stern Layer charge (SL charge) and the Debye screening length to describe the SFG intensity variation from CsCl to LiCl. We find that, to change the model curve from CsCl to match that of LiCl, a 10 times larger SL charge density has to be employed in conjunction with a roughly 2.3 times larger effective Debye length. Changing the SL charge density gives rise to a roughly 5 times higher curve maximum as evident when comparing panels (a) and (b) in Figure 38; the change in Debye length is required to shift the maximum in SFG intensity to higher concentration. Hence, this model suggests dramatic – essentially unphysical –increases of not only the SL potential but also the Debye length with decreasing the ion size (Cs^+ to Li^+) which indicates that finite ion sizes have to be accounted for in a direct manner instead of empirically changing the original model.

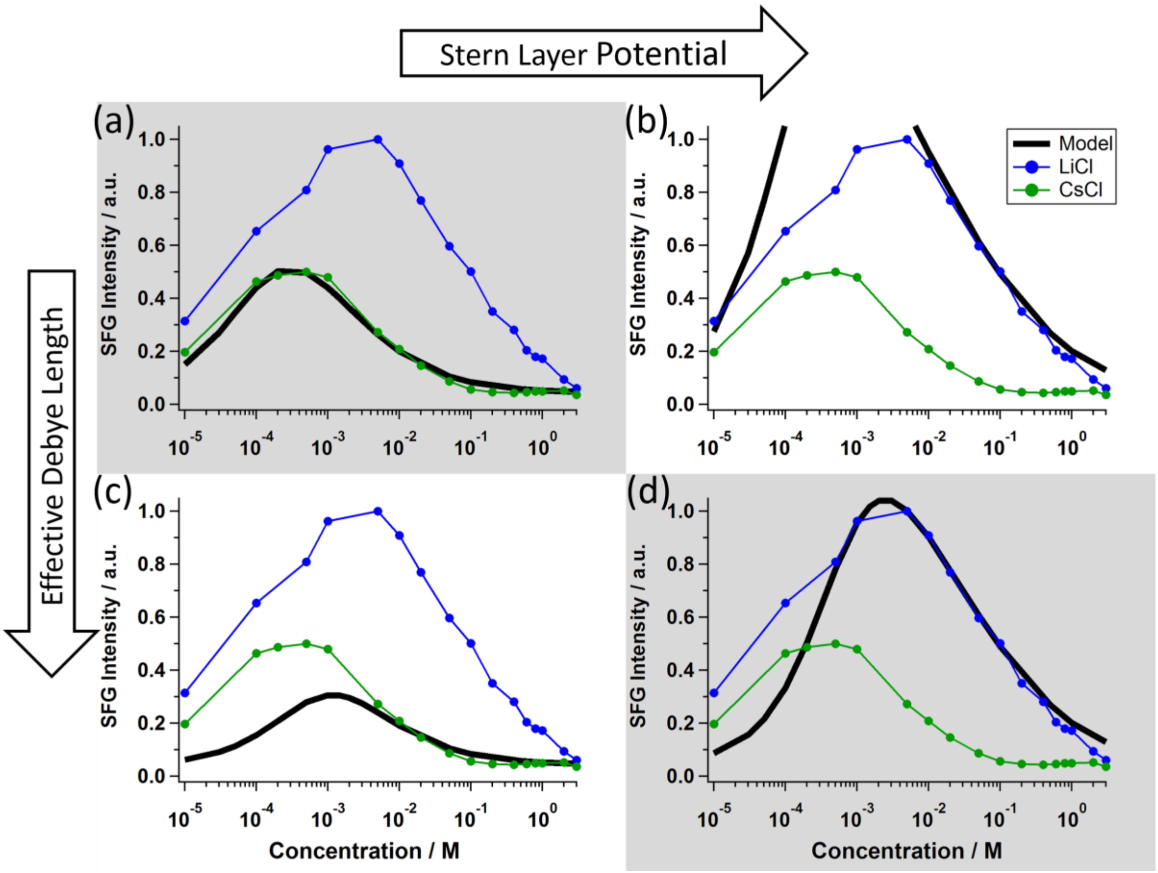

Figure 38: Model employed to fit both, the LiCl and the CsCl SFG curve by varying the effective Debye screening length and the effective surface charge. (a) and (d) are the best fits for CsCl and LiCl, respectively; (b) and (c) show how the fit curve changes if only one of the two parameters is altered.

Therefore we employed a modified Poisson-Boltzmann description of the EDL that accounts for ion size effects and the dielectric properties of ions[111]. This model allows calculating the interfacial ion concentration profiles and the corresponding surface electric fields for the different electrolytes at various concentrations. Based on the integrated electric fields and interfacial water concentration profiles, the field-dependent SFG response is calculated. Together with the experimental SFG curves from Figure 36, the theoretical results are presented in Figure 39. When invoking the hydrated ion radii and a dielectric permittivity of 30 for the hydrated ions,[111,112] we find semi-quantitative agreement for the relative SFG intensities with the different ions at sub-molar ionic strength. Additionally, the model predicts an increase of the slope in the SFG curve with increasing hydration radius, i.e. in the series $Cs^+ < K^+ < Na^+ < Li^+$, which is also in line with the experiment.

In contrast, we found less agreement with the model when (a) employing bare ionic radii, (b) omitting the contribution of hydration water or (c) assuming higher dielectric permittivity for the ions, respectively (illustrated in chapter 5.4). With employing bare ionic radii, the SFG curves for the alkali cations are very similar to one another, which indicates that the interfacial distribution of ions is determined by the hydrated radius. If we subtract the hydration water from the water concentration profiles, the ion-specific trend reverses, and the differences between the curves get smaller. This suggests that in the experiment, hydration water contributes to the net SFG response. For yielding a relative agreement with the experimental curves, an ion permittivity of 30 has to be invoked which is substantially lower than that of water (~78). If assuming an ion permittivity closer to that of water, the ion-specific trend vanishes.

Based on these considerations, the observed differences in the experimental SFG curves can be related to a cation-specific interfacial ion distribution that generates differences in the magnitude and decay of the surface electric field, only if hydrated, polarizable ions are employed.

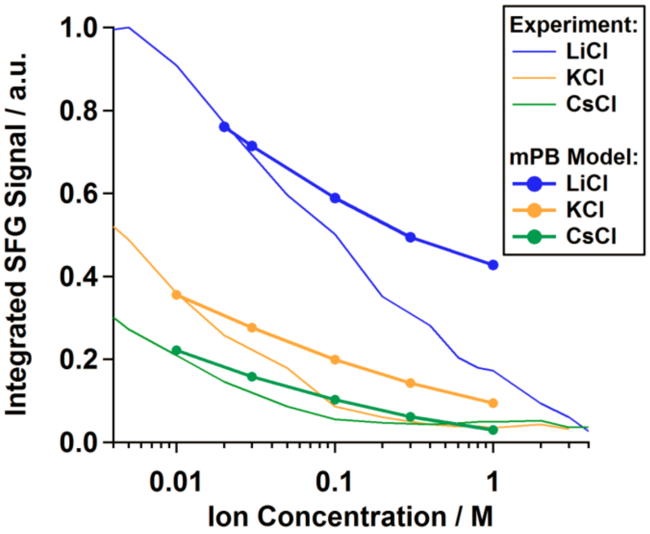

Figure 39: O-H stretch SFG curves for silica/water with solutions of LiCl (blue), KCl (orange) and CsCl (green) as presented in Figure 36. In comparison, the squared integrated surface electric fields calculated from a modified Poisson-Boltzmann model of polarizable ions,[111] using hydrated ion radii: 5.3 Å, 3.9 Å and 2.5 Å for Li^+, K^+ and Cs^+, respectively (reported in ref. [112]).

5.3 Conclusion

In conclusion, we found that alkali salts with larger but less hydrated cations as Cs^+ screen surface charges better than those with smaller but highly hydrated cations as Li^+. Our results indicate that for a negatively charged surface like silica, the cation species determines the screening behavior of the electrolyte. By comparing our SFG results with the previously proposed Gouy-Chapman-based SFG model and modified Poisson-Boltzmann calculations, we conclude that this relates to an ion-specific surface propensity, that increases with decreasing hydration radius.

5.4 Additional Data

5.4.1 Modified Poisson-Boltzmann model and SFG

The modified Poisson-Boltzmann calculations presented in Figure 39 are based on the framework reported in ref. [111]. The predicted SFG response results from the square of the integrated surface electric field, accounting for the effective interfacial water concentration. Form comparison of our experimental results with that model, we have concluded that the ion-specific screening properties of alkali ions can be related to the hydration radii which gives rise to different surface propensities. This section shows additional results from that model which support our conclusion.

5.4.1.1 Ionic vs. Hydration radii

Figure 40 presents the predicted SFG response using different versions of the model.

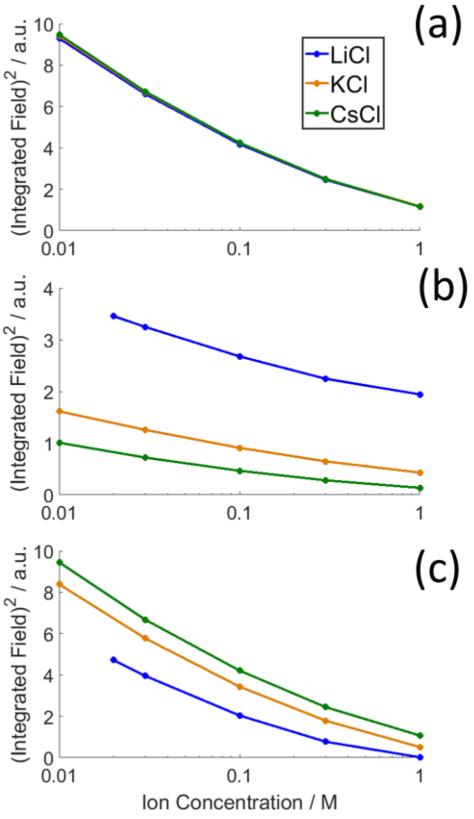

Figure 40: Predicted SFG response calculated from the squared integrated electric field invoking (a) ionic radii of r(Li$^+$) = 0.8 Å, r(K$^+$) = 1.6 Å and r(Cs$^+$) = 2.1 Å (b) hydrated radii of r(Li$^+$) = 5.3 Å, r(K$^+$) = 3.9 Å

and r(Cs^+) = 2.5 Å. All radii are reported in ref. [112]. In (c) the hydrated radii with hydration water considered as SFG inactive.

In Figure 40a and b, we compare model versions that employ (a) the ionic radii and (b) the hydrated radii. As can be inferred, only when invoking the hydrated radii, the model predicts an ion-specific result. In Figure 40c the hydration water is regarded as SFG inactive which gives rise to a smaller and reversed ion-specific trend compared to Figure 40b. By comparison with our SFG results, this indicates that hydration water is SFG active in the experiment.

The calculated interfacial cation concentration and resulting surface electric field that give rise to the predicted SFG signals in Figure 40a and b are presented in Figure 41. The results based on the ionic radii are presented in Figure 41a and b, those based on the hydrated radii are depicted in Figure 41c and d. It shows that only the hydrated radii give rise to an ion-specific interfacial concentration and surface electric field.

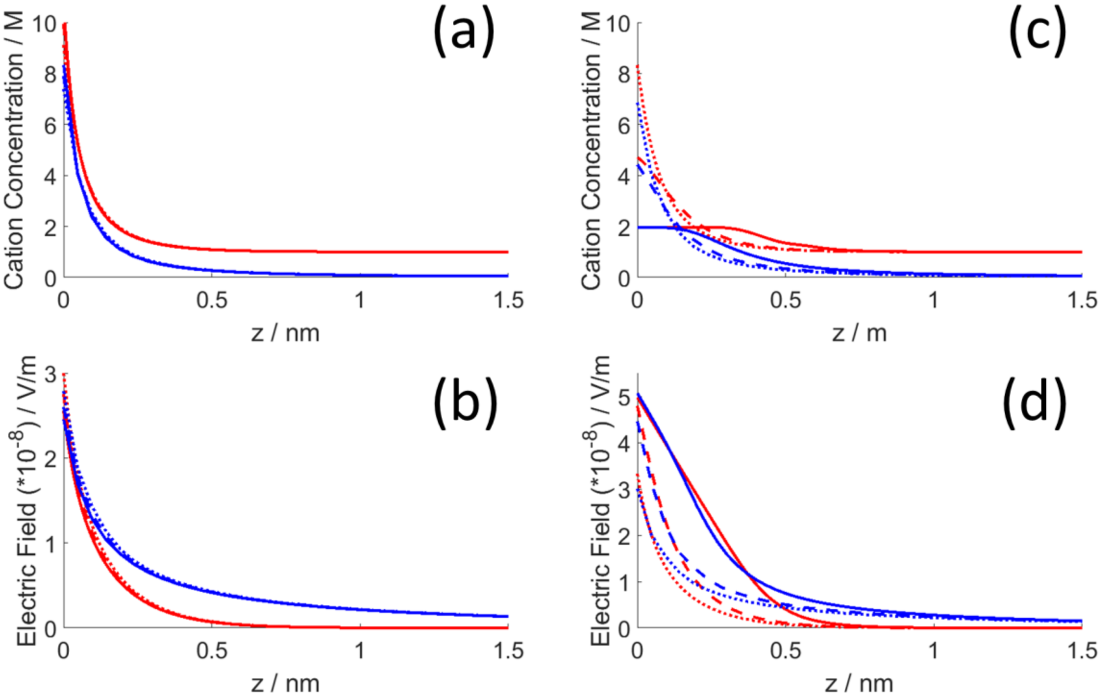

Figure 41: Calculated interfacial cation concentration and resulting surface electric field, employing ionic (a and b) and hydrated radii (c and d), respectively. Solid: LiCl, dashed: KCl, dotted: CsCl. Red lines: 1 M, blue lines: 0.03 M ion concentration.

5.4.1.2 Ion permittivity and the effect on the SFG response

In the main text, it has been argued that in order to yield a relative agreement between the model and the experimental curves, an ion permittivity of 30 has to be invoked. Figure 42 illustrates that especially the curve predicted for Li$^+$, the ion with the largest effective volume, is sensitive for variation of the permittivity. For a permittivity closer to that of water (~78), the curves are more similar to one another, indicating that the ion permittivity is relevant for understanding the ion-specific SFG response.

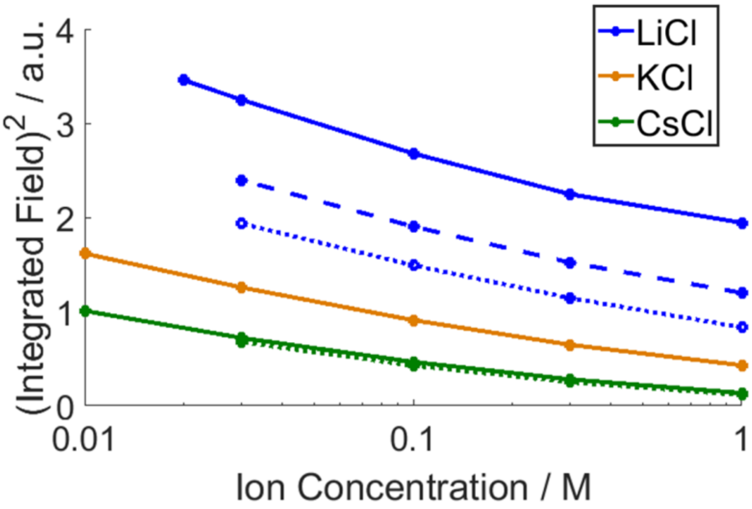

Figure 42: Predicted SFG response calculated as in Figure 40b with different ion permittivity (ε): Solid: ε = 30, dashed: ε = 45, dotted: ε = 60.

5.4.2 The Gouy Chapman-based SFG model

The concentration dependence of the Stern layer potential and the Debye length as employed for the model results for CsCl and LiCl (in Figure 38) are summarized in Figure 43. Figure 43(a) shows the calculated Stern layer potential as a function of ion concentration using different effective charge densities for LiCl and CsCl, respectively.

$$\phi_d = \frac{2k_B T}{e_c}\sinh^{-1}\left(\frac{\sigma_d}{\sqrt{8000 k_B T N_A c \varepsilon_0 \varepsilon_r}}\right) \tag{51}$$

As can be inferred, a higher effective charge density gives rise to an offset in the Stern layer-potential between these two salts which is in qualitative agreement with previous XPS studies of the same system.[11] Figure 43(b) plots the effective Debye lengths and the resulting interference terms, both against the salt concentration. The original Debye length (κ_{ref}^{-1}) can be calculated from

$$\kappa_{ref}^{-1} = \sqrt{\frac{\varepsilon_0 \varepsilon_r k_B T}{2000 e_c^2 N_A c}} \tag{52}$$

and is scaled by *a*, an empirically determined factor to match the corresponding experimental SFG curve.

$$\kappa_{eff}^{-1} = a * \kappa_{ref}^{-1} \tag{53}$$

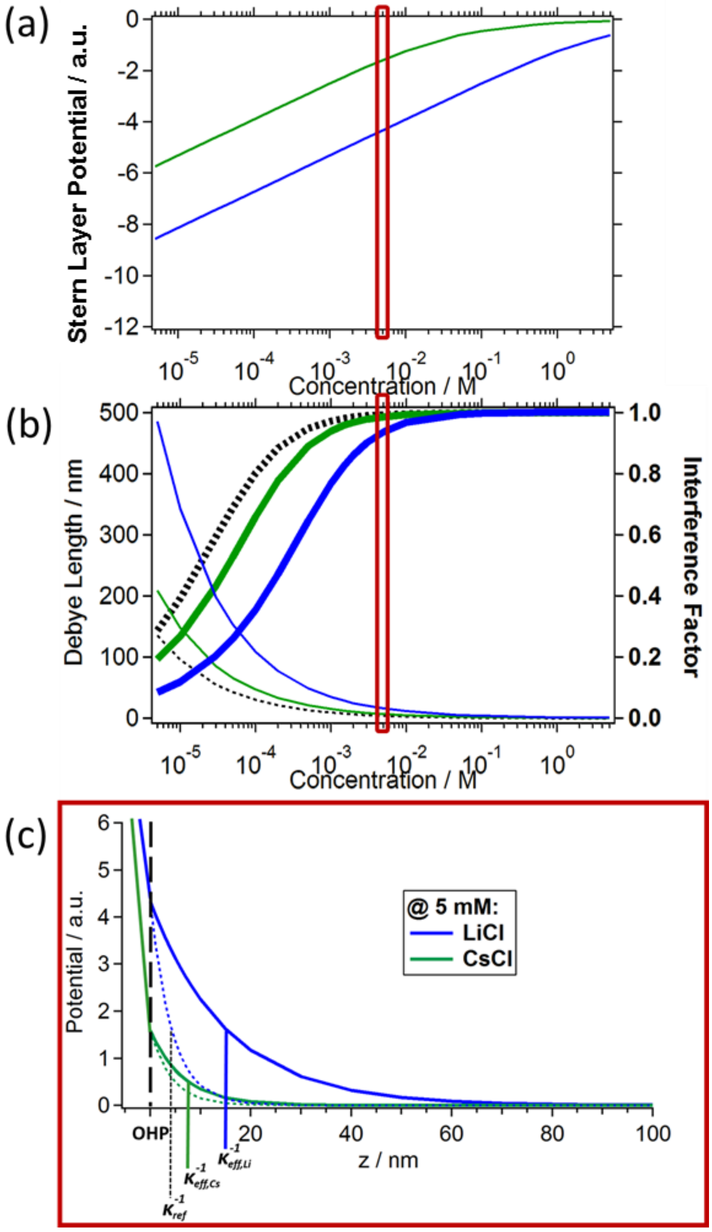

Figure 43: Summary of the employed functions ((a), (b)) and the physical picture for the EDL ((c)) of the silica/water interface, resulting from the model comparing aqueous solutions of LiCl (blue), CsCl (green) and point charges (dashed lines) as screening agents.

The 2.3 times larger screening length invoked for LiCl compared to CsCl gives rise to a shift of the interference curve by roughly one order of magnitude towards higher concentration. As a consequence, the SFG intensity curve shifts by the same degree as discussed with Figure 38. In both cases, the effective Debye length is substantially larger than the calculated on assuming point charges. Please note that the ionic species that deviates most from point charge behavior is the smallest but most hydrated one, i.e., Lithium. Based on the employed model, we find a roughly 3.6 times larger screening length for Lithium compared to point charge screening (κ_{ref}^{-1} , dashed lines in Figure 43. This supports our notion that the critical parameter for understanding ion specific charge screening in the aqueous medium is not the ionic radius but the resulting hydrated radius or the hydration number.

Based on the model parameters presented in Figure 43(a) and (b) for LiCl and CsCl, Figure 43(c) illustrates the surface potential decay throughout the EDL at the example of a 5 mM electrolyte solution, given by:

$$\phi(z) = \phi_d e^{-\kappa z} \tag{54}$$

Summary

In this thesis, we have studied interfacial water and its impact on the physical and chemical properties of a mineral/water interface. We employed Vibrational Sum Frequency Generation (V-SFG) Spectroscopy, a non-linear, surface-sensitive and chemically selective spectroscopy technique to study water in contact with silica, an abundant and prototypical mineral.

O-H stretch vibrations in H-bonding environments are often coupled which is the case not only for bulk water but also the air/water and the silica/water interface. In chapter 2, we have presented a work in which we demonstrate the presence of vibrational coupling in interfacial and bulk water, and disentangle intra- from intermolecular contributions to the corresponding vibrational spectra.

The surface-sensitivity of SFG at charged interfaces varies substantially depending on the charge distribution in the near-surface region. In chapter 3, we have shown that for silica/water, it can vary between almost monolayer sensitivity at very high and very low electrolyte concentration, and roughly 100 nm of water layers in the intermediate concentration regime (~mM).

In chapter 4, we have used this correlation to study the dissolution kinetics of silica in water from an interfacial perspective. We found that silica dissolves through an autocatalytic mechanism and generates roughly a millimole of charged dissolution products in the near-surface region within a timescale of a day. Comparing our results to corresponding bulk studies has revealed that the dissolution process is diffusion-limited.

In the last part of this thesis, we have studied the ion-specificity of the interfacial charge distribution at the silica/water interface and the associated electrochemical properties such as the surface potential. Our results indicate that surface charges are screened more efficiently by larger, less hydrated, ions which has implications for the validity of traditionally used electric double layer models that assume point charges.

Zusammenfassung

In dieser Doktorarbeit haben wir Wasser und dessen Einfluss auf die physikalischen und chemischen Eigenschaften einer Mineral/Wasser Grenzfläche untersucht. Wir nutzten Vibrations-Summenfrequenz-Spektroskopie (V-SFG), eine nicht-lineare, oberflächen-sensitive und chemisch-selektive Spektroskopie Technik, um Wasser in Kontakt mit Silica, einem prototypischen Mineral, zu betrachten.

O-H Streckschwingungen in Wasserstoffbrücken-gebundener Umgebung sind oft gekoppelt, und zwar nicht nur in kondensierter Phase, sondern auch an der Luft/Wasser und Silica/Wasser Grenzfläche. In Kapitel 2 haben wir eine Arbeit präsentiert, in der wir zeigen, dass solche Schwingungen sowohl über intra- als auch intermolekulare Mechanismen gekoppelt sind.

An geladenen Grenzflächen variiert die Oberflächensensitivität von SFG erheblich in Abhängigkeit von der Ladungsverteilung Nahe der Oberfläche. In Kapitel 3 haben wir für Silica/Wasser gezeigt, dass die Probentiefe in Abhängigkeit von der Elektrolytkonzentration zwischen einer Monolage und einer 100 nm dicken Wasserschicht variieren kann.

In Kapitel 4 haben wir diese Korrelation zwischen Elektrolytkonzentration und Probentiefe genutzt, um den Lösevorgang von Silica an der Grenzfläche mit Wasser zu untersuchen. Wir konnten zeigen, dass sich Silica in Wasser über einen autokatalytischen Mechanismus löst und innerhalb eines Tages etwa ein Millimol geladener Lösungsprodukte nahe der Oberfläche generiert. Der Vergleich mit Studien an Silica Suspensionen konnte zeigen, dass dieser Lösungsvorgang diffusions-limitiert ist.

Im letzten Teil dieser Arbeit haben wir die ionen-spezifische Ladungsverteilung an der Silica/Wasser Grenzfläche und die daraus resultierenden elektrochemischen Eigenschaften, wie das Oberflächenpotential, untersucht. Unsere Ergebnisse konnten zeigen, dass größere Ionen, mit geringerem Hydratationsradius, Oberflächenladungen effizienter abschirmen können als kleinere, stärker hydratisierte, Ionen. Daraus ergaben sich neue Erkenntnisse für die Anwendbarkeit traditionell genutzter Grenzflächenmodelle, die auf Punktladungen basieren.

Acknowledgments

Bibliography

1. Putnis, A. Why mineral interfaces matter. *Science* **343,** 1441–1442 (2014).
2. Wang, H.-F., Gan, W., Lu, R., Rao, Y. & Wu, B.-H. Quantitative spectral and orientational analysis in surface sum frequency generation vibrational spectroscopy (SFG-VS). *Int. Rev. Phys. Chem.* **24,** 191–256 (2005).
3. Lambert, A. G., Davies, P. B. & Neivandt, D. J. Implementing the theory of sum frequency generation vibrational spectroscopy: a tutorial review. *Appl. Spectrosc. Rev.* **40,** 103–145 (2005).
4. Mizrahi, V. & Sipe, J. E. Phenomenological treatment of surface second-harmonic generation. *J. Opt. Soc. Am. B* **5,** 660–667 (1988).
5. Zhuang, X., Miranda, P. B., Kim, D. & Shen, Y. R. Mapping molecular orientation and conformation at interfaces by surface nonlinear optics. *Phys. Rev. B* **59,** 12632 (1999).
6. Feng, R., Guo, Y., Lü, R., Velarde, L. & Wang, H. Consistency in the sum frequency generation intensity and phase vibrational spectra of the air/neat water interface. *J. Phys. Chem. A* **115,** 6015–6027 (2011).
7. Backus, E. H. G., Garcia-Araez, N., Bonn, M. & Bakker, H. J. On the Role of Fresnel Factors in Sum-Frequency Generation Spectroscopy of Metal − Water and Metal-Oxide − Water Interfaces. *J. Phys. Chem. C* **116,** 23351 (2012).
8. Tian, C. S. & Shen, Y. R. Recent progress on sum-frequency spectroscopy. *Surf. Sci. Rep.* **69,** 105–131 (2014).
9. Gan, W., Wu, B., Chen, H., Guo, Y. & Wang, H. Accuracy and sensitivity of determining molecular orientation at interfaces using sum frequency generation vibrational spectroscopy. *Chem. Phys. Lett.* **406,** 467–473 (2005).
10. Ji, N., Ostroverkhov, V., Chen, C.-Y. & Shen, Y.-R. Phase-sensitive sum-frequency vibrational spectroscopy and its application to studies of interfacial alkyl chains. *J. Am. Chem. Soc.* **129,** 10056–10057 (2007).
11. Brown, M. A. *et al.* Determination of Surface Potential and Electrical Double-Layer Structure at the Aqueous Electrolyte-Nanoparticle Interface. *Phys. Rev. X* **6,** 11007 (2016).

12. Gonella, G., Lütgebaucks, C., de Beer, A. G. F. & Roke, S. Second Harmonic and Sum-Frequency Generation from Aqueous Interfaces Is Modulated by Interference. *J. Phys. Chem. C* **120,** 9165–9173 (2016).

13. Wen, Y.-C. *et al.* Unveiling Microscopic Structures of Charged Water Interfaces by Surface-Specific Vibrational Spectroscopy. *Phys. Rev. Lett.* **116,** 16101 (2016).

14. Ong, S., Zhao, X. & Eisenthal, K. B. Polarization of water molecules at a charged interface: second harmonic studies of the silica/water interface. *Chem. Phys. Lett.* **191,** 327–335 (1992).

15. Jena, K. C., Covert, P. A. & Hore, D. K. The effect of salt on the water structure at a charged solid surface: differentiating second-and third-order nonlinear contributions. *J. Phys. Chem. Lett.* **2,** 1056–1061 (2011).

16. Schaefer, J., Gonella, G., Bonn, M. & Backus, E. H. G. Surface-specific vibrational spectroscopy of the water/silica interface: screening and interference. *Phys. Chem. Chem. Phys.* **19,** 16875–16880 (2017).

17. Yang, Z., Li, Q. & Chou, K. C. Structures of water molecules at the interfaces of aqueous salt solutions and silica: Cation effects. *J. Phys. Chem. C* **113,** 8201–8205 (2009).

18. Jena, K. C. & Hore, D. K. Variation of ionic strength reveals the interfacial water structure at a charged mineral surface. *J. Phys. Chem. C* **113,** 15364–15372 (2009).

19. Lovering, K. A., Bertram, A. K. & Chou, K. C. New Information on the Ion-Identity Dependent Structure of Stern Layer Revealed by Sum Frequency Generation Vibrational Spectroscopy. *J. Phys. Chem. C* (2016).

20. Urashima, S., Myalitsin, A., Nihonyanagi, S. & Tahara, T. The Topmost Water Structure at a Charged Silica/Aqueous Interface Revealed by Heterodyne-Detected Vibrational Sum Frequency Generation Spectroscopy. *J. Phys. Chem. Lett.* **9,** 4109–4114 (2018).

21. Boamah, M. D., Ohno, P. E., Geiger, F. M. & Eisenthal, K. B. Relative permittivity in the electrical double layer from nonlinear optics. *J. Chem. Phys* **148,** 222808 (2018).

22. Azam, M. S., Weeraman, C. N. & Gibbs-Davis, J. M. Specific cation effects on the bimodal acid–base behavior of the silica/water interface. *J. Phys. Chem. Lett.* **3,** 1269–1274 (2012).

23. Azam, M. S., Weeraman, C. N. & Gibbs-Davis, J. M. Halide-induced cooperative acid–base behavior at a negatively charged interface. *J. Phys. Chem. C* **117,** 8840–8850 (2013).

24. Azam, M. S., Darlington, A. & Gibbs-Davis, J. M. The influence of concentration on specific ion effects at the silica/water interface. *J. Phys.-Condens. Mat.* **26,** 244107 (2014).

25. Darlington, A. M. & Gibbs-Davis, J. M. Bimodal or trimodal? The influence of starting pH on site identity and distribution at the low salt aqueous/silica interface. *J. Phys. Chem. C* **119,** 16560–16567 (2015).

26. Dewan, S., Yeganeh, M. S. & Borguet, E. Experimental correlation between interfacial water structure and mineral reactivity. *J. Phys. Chem. Lett.* **4,** 1977–1982 (2013).

27. Myalitsin, A., Urashima, S. H., Nihonyanagi, S., Yamaguchi, S. & Tahara, T. Water structure at the buried silica/aqueous interface studied by heterodyne-detected vibrational sum-frequency generation. *J. Phys. Chem. C* **120,** 9357–9363 (2016).

28. Darlington, A. M. *et al.* Separating the pH-Dependent Behavior of Water in the Stern and Diffuse Layers with Varying Salt Concentration. *J. Phys. Chem. C* **121,** 20229–20241 (2017).

29. DeWalt-Kerian, E. L. *et al.* pH-Dependent Inversion of Hofmeister Trends in the Water Structure of the Electrical Double Layer. *J. Phys. Chem. Lett.* **8,** 2855–2861 (2017).

30. Du, Q., Freysz, E. & Shen, Y. R. Vibrational spectra of water molecules at quartz/water interfaces. *Phys. Rev. Lett.* **72,** 238 (1994).

31. Ostroverkhov, V., Waychunas, G. A. & Shen, Y. R. Vibrational spectra of water at water/α-quartz (0001) interface. *Chem. Phys. Lett.* **386,** 144–148 (2004).

32. Ostroverkhov, V., Waychunas, G. A. & Shen, Y. R. New information on water interfacial structure revealed by phase-sensitive surface spectroscopy. *Phys. Rev. Lett.* **94,** 46102 (2005).

33. Dalstein, L., Potapova, E. & Tyrode, E. The elusive silica/water interface: isolated silanols under water as revealed by vibrational sum frequency spectroscopy. *Phys. Chem. Chem. Phys.* **19,** 10343–10349 (2017).

34. Cyran, J. D. *et al.* Molecular Hydrophobicity at a Macroscopically Hydrophilic Surface. *submitted* (2018).

35. Bertie, J. E. & Lan, Z. Infrared Intensities of Liquids XX: The Intensity of the OH Stretching Band of Liquid Water Revisited, and the Best Current Values of the Optical Constants of H_2O (l) at 25° C between 15,000 and 1 cm^{-1}. *Appl. Spectrosc.* **50,** 1047–1057 (1996).

36. Du, Q., Superfine, R., Freysz, E. & Shen, Y. R. Vibrational spectroscopy of water at the vapor/water interface. *Phys. Rev. Lett.* **70,** 2313 (1993).

37. Covert, P. A., Jena, K. C. & Hore, D. K. Throwing salt into the mix: Altering interfacial water structure by electrolyte addition. *J. Phys. Chem. Lett.* **5,** 143–148 (2013).

38. DeWalt-Kerian, E. L. *et al.* Correction to “pH-Dependent Inversion of Hofmeister Trends in the Water Structure of the Electrical Double Layer”. *J. Phys. Chem. Lett.* **8,** 4793–4793 (2017).

39. Gibbs-Davis, J. M., Kruk, J. J., Konek, C. T., Scheidt, K. A. & Geiger, F. M. Jammed acid-base reactions at interfaces. *J. Am. Chem. Soc.* **130,** 15444–15447 (2008).

40. Lis, D., Backus, E. H. G., Hunger, J., Parekh, S. H. & Bonn, M. Liquid flow along a solid surface reversibly alters interfacial chemistry. *Science* **344,** 1138–1142 (2014).

41. Bakker, H. J. & Skinner, J. L. Vibrational spectroscopy as a probe of structure and dynamics in liquid water. *Chem. Rev.* **110,** 1498–1517 (2009).

42. Perakis, F. *et al.* Vibrational Spectroscopy and Dynamics of Water. *Chem. Rev.* **116,** 7590–7607 (2016).

43. Kim, H. & Cho, M. Infrared probes for studying the structure and dynamics of biomolecules. *Chem. Rev.* **113,** 5817–5847 (2013).

44. Auer, B. M. & Skinner, J. L. IR and Raman spectra of liquid water: Theory and interpretation. *J. Chem. Phys.* **128,** 224511 (2008).

45. Heyden, M. *et al.* Dissecting the THz spectrum of liquid water from first principles via correlations in time and space. *Proc. Natl. Acad. Sci. USA* **107,** 12068–12073 (2010).

46. Kühne, T. D. & Khaliullin, R. Z. Electronic signature of the instantaneous asymmetry in the first coordination shell of liquid water. *Nat. Commun.* **4,** 1450 (2013).

47. Choi, J.-H. H. & Cho, M. Computational IR spectroscopy of water: OH stretch

frequencies, transition dipoles, and intermolecular vibrational coupling constants. *J. Chem. Phys.* **138,** 174108 (2013).

48. Liu, H., Wang, Y. & Bowman, J. M. Quantum Local Monomer IR Spectrum of Liquid D_2O at 300 K from 0 to 4000 cm^{-1} Is in Near-Quantitative Agreement with Experiment. *J. Phys. Chem. B* **120,** 2824–2828 (2016).

49. Ramasesha, K., De Marco, L., Mandal, A. & Tokmakoff, A. Water vibrations have strongly mixed intra-and intermolecular character. *Nat. Chem.* **5,** 935–940 (2013).

50. Woutersen, S. & Bakker, H. J. Resonant intermolecular transfer of vibrational energy in liquid water. *Nature* **402,** 597 (1999).

51. De Marco, L. *et al.* Differences in the Vibrational Dynamics of H_2O and D_2O: Observation of Symmetric and Antisymmetric Stretching Vibrations in Heavy Water. *J. Phys. Chem. Lett.* **7,** 1769–1774 (2016).

52. Nagata, Y., Yoshimune, S., Hsieh, C.-S., Hunger, J. & Bonn, M. Ultrafast vibrational dynamics of water disentangled by reverse nonequilibrium ab initio molecular dynamics simulations. *Phys. Rev. X* **5,** 21002 (2015).

53. Henri-Rousseau, O., Blaise, P. & Chamma, D. Infrared lineshapes of weak hydrogen bonds: Recent quantum developments. *Adv. Chem. Phys.* **121,** 241–310 (2002).

54. Ashihara, S., Huse, N., Espagne, A., Nibbering, E. T. J. & Elsaesser, T. Vibrational couplings and ultrafast relaxation of the O-H bending mode in liquid H_2O. *Chem. Phys. Lett.* **424,** 66–70 (2006).

55. De Marco, L., Ramasesha, K. & Tokmakoff, A. Experimental evidence of fermi resonances in isotopically dilute water from ultrafast broadband IR spectroscopy. *J. Phys. Chem. B* **117,** 15319–15327 (2013).

56. Rey, R., Møller, K. B. & Hynes, J. T. Hydrogen bond dynamics in water and ultrafast infrared spectroscopy. *J. Phys. Chem. A* **106,** 11993–11996 (2002).

57. van der Post, S. T. *et al.* Strong frequency dependence of vibrational relaxation in bulk and surface water reveals sub-picosecond structural heterogeneity. *Nat. Commun.* **6,** 1–7 (2015).

58. Cowan, M. L. *et al.* Ultrafast memory loss and energy redistribution in the hydrogen bond network of liquid H_2O. *Nature* **434,** 199 (2005).

59. Tian, C. S. & Shen, Y. R. Sum-frequency vibrational spectroscopic studies of water/vapor interfaces. *Chem. Phys. Lett.* **470,** 1–6 (2009).

60. Nihonyanagi, S. *et al.* Unified molecular view of the air/water interface based on experimental and theoretical $\chi^{(2)}$ spectra of an isotopically diluted water surface. *J. Am. Chem. Soc.* **133,** 16875–16880 (2011).

61. Stiopkin, I. V. *et al.* Hydrogen bonding at the water surface revealed by isotopic dilution spectroscopy. *Nature* **474,** 192–195 (2011).

62. Inoue, K. I. *et al.* Efficient Spectral Diffusion at the Air/Water Interface Revealed by Femtosecond Time-Resolved Heterodyne-Detected Vibrational Sum Frequency Generation Spectroscopy. *J. Phys. Chem. Lett.* **7,** 1811–1815 (2016).

63. Raymond, E. A., Tarbuck, T. L. & Richmond, G. L. Isotopic dilution studies of the vapor/water interface as investigated by vibrational sum-frequency spectroscopy. *J. Phys. Chem. B* **106,** 2817–2820 (2002).

64. Sovago, M. *et al.* Vibrational response of hydrogen-bonded interfacial water is dominated by intramolecular coupling. *Phys. Rev. Lett.* **100,** 173901 (2008).

65. Nagata, Y. & Mukamel, S. Vibrational sum-frequency generation spectroscopy at the water/lipid interface: molecular dynamics simulation study. *J. Am. Chem. Soc.* **132,** 6434–6442 (2010).

66. Ohto, T., Usui, K., Hasegawa, T., Bonn, M. & Nagata, Y. Toward ab initio molecular dynamics modeling for sum-frequency generation spectra; an efficient algorithm based on surface-specific velocity-velocity correlation function. *J. Chem. Phys.* **143,** 124702 (2015).

67. Pieniazek, P. A., Tainter, C. J. & Skinner, J. L. Surface of liquid water: Three-body interactions and vibrational sum-frequency spectroscopy. *J. Am. Chem. Soc.* **133,** 10360–10363 (2011).

68. Nagata, Y. *et al.* The surface roughness, but not the water molecular orientation varies with temperature at the water-air interface. *Phys. Chem. Chem. Phys.* **17,** 23559–23564 (2015).

69. Bertie, J. E. & Zhang, S. L. Infrared intensities of liquids XXI: Integrated absorption intensities of CH_3OH, CH_3OD, CD_3OH and CD_3OD and dipole moment derivatives of methanol. *J. Mol. Struct.* **413,** 333–363 (1997).

70. Hasegawa, T. & Tanimura, Y. A polarizable water model for intramolecular and intermolecular vibrational spectroscopies. *J. Phys. Chem. B* **115,** 5545–5553 (2011).

71. Morita, A. & Hynes, J. T. A theoretical analysis of the sum frequency generation spectrum of the water surface. II. Time-dependent approach. *J. Phys. Chem. B* **106,** 673–685 (2002).

72. Ma, G. & Allen, H. C. Surface Studies of Aqueous Methanol Solutions by Vibrational Broad Bandwidth Sum Frequency Generation Spectroscopy. *J. Phys. Chem. B* **107,** 6343–6349 (2003).

73. Buck, M. & Himmelhaus, M. Vibrational spectroscopy of interfaces by infrared–visible sum frequency generation. *J. Vac. Sci. Technol. A* **19,** 2717–2736 (2001).

74. Gan, W., Wu, D., Zhang, Z., Feng, R. R. & Wang, H. F. Polarization and experimental configuration analyses of sum frequency generation vibrational spectra, structure, and orientational motion of the air/water interface. *J. Chem. Phys.* **124,** 114705 (2006).

75. Lu, R. *et al.* CH stretching vibrations of methyl, methylene and methine groups at the vapor/alcohol (n= 1-8) interfaces. *J. Phys. Chem. B* **109,** 14118–14129 (2005).

76. Wei, X., Hong, S.-C., Zhuang, X., Goto, T. & Shen, Y. R. Nonlinear optical studies of liquid crystal alignment on a rubbed polyvinyl alcohol surface. *Phys. Rev. E* **62,** 5160 (2000).

77. Bodis, P., Larsen, O. F. A. & Woutersen, S. Vibrational relaxation of the bending mode of HDO in liquid D_2O. *J. Phys. Chem. A* **109,** 5303–5306 (2005).

78. Tian, C.-S. & Shen, Y. R. Isotopic dilution study of the water/vapor interface by phase-sensitive sum-frequency vibrational spectroscopy. *J. Am. Chem. Soc.* **131,** 2790–2791 (2009).

79. Ohto, T. *et al.* Unveiling the Amphiphilic Nature of TMAO by Vibrational Sum Frequency Generation Spectroscopy. *J. Phys. Chem. C* **120,** 17435–17443 (2016).

80. Yamaguchi, S. Comment on “Phase reference in phase-sensitive sum-frequency vibrational spectroscopy” [J. Chem. Phys. 144, 244711 (2016)]. *J. Chem. Phys.* **145,** 167101 (2016).

81. Sun, S. *et al.* Response to ‘comment on 'Phase reference in phase-sensitive sum-frequency vibrational spectroscopy’’ [J. Chem. Phys. 145, 167101 (2016)]. *Journal of*

Chemical Physics **145,** 167102 (2016).

82. Gan, W., Wu, B., Zhang, Z., Yuan, G. & Wang, H. Vibrational Spectra and Molecular Orientation with Experimental Configuration Analysis in Surface Sum Frequency Generation (SFG). *J. Phys. Chem. C* **111,** 8716–8725 (2007).

83. Nagata, Y. *et al.* Water Bending Mode at the Water-Vapor Interface Probed by Sum-Frequency Generation Spectroscopy: A Combined Molecular Dynamics Simulation and Experimental Study. *J Phys Chem Lett* **4,** 1872–1877 (2013).

84. Ivanov, S. D., Witt, A., Shiga, M. & Marx, D. Communications: On artificial frequency shifts in infrared spectra obtained from centroid molecular dynamics: Quantum liquid water. *J. Chem. Phys.* **132,** 31101 (2010).

85. Ishiyama, T., Sokolov, V. V., Akihiro, M., Morita, A. & Akihiro, M. Molecular dynamics simulation of liquid methanol. II. Unified assignment of infrared, raman, and sum frequency generation vibrational spectra in methyl C–H stretching region. *J. Chem. Phys.* **134,** 024510 (2011).

86. Wei Gan, Zhang, Z., Feng, R. & Wang, H. Spectral interference and molecular conformation at liquid interface with sum frequency generation vibrational spectroscopy (SFG-VS). *J. Phys. Chem. C* **111,** 8726–8738 (2007).

87. Dove, P. M. & Craven, C. M. Surface charge density on silica in alkali and alkaline earth chloride electrolyte solutions. *Geochim. Cosmochim. Acta* **69,** 4963–4970 (2005).

88. Karlsson, M., Craven, C., Dove, P. M. & Casey, W. H. Surface charge concentrations on silica in different 1.0 M metal-chloride background electrolytes and implications for dissolution rates. *Aquat. Geochem.* **7,** 13–32 (2001).

89. Morag, J., Dishon, M. & Sivan, U. The governing role of surface hydration in ion specific adsorption to silica: An AFM-based account of the hofmeister universality and its reversal. *Langmuir* **29,** 6317–6322 (2013).

90. Brown, M. A., Goel, A. & Abbas, Z. Effect of electrolyte concentration on the stern layer thickness at a charged interface. *Angew. Chem. Int. Ed.* **55,** 3790–3794 (2016).

91. Ostroverkhov, V., Waychunas, G. A. & Shen, Y. R. Vibrational spectra of water at water/α-quartz (0001) interface. *Chem. Phys. Lett.* **386,** 144–148 (2004).

92. Ohno, P. E., Saslow, S. A., Wang, H., Geiger, F. M. & Eisenthal, K. B. Phase-

referenced nonlinear spectroscopy of the α-quartz/water interface. *Nat. Commun.* **7,** (2016).

93. Gragson, D. E. & Richmond, G. L. Investigations of the Structure and Hydrogen Bonding of Water Molecules at Liquid Surfaces by Vibrational Sum Frequency Spectroscopy. *J. Phys. Chem. B* **102,** 3847–3861 (1998).
94. Eftekhari-Bafrooei, A. & Borguet, E. Effect of surface charge on the vibrational dynamics of interfacial water. *J. Am. Chem. Soc.* **131,** 12034–12035 (2009).
95. Levine, B. F. & Bethea, C. G. Second and third order hyperpolarizabilities of organic molecules. *J. Chem. Phys.* **63,** 2666–2682 (1975).
96. Lütgebaucks, C., Gonella, G. & Roke, S. Optical label-free and model-free probe of the surface potential of nanoscale and microscopic objects in aqueous solution. *Phys. Rev. B* **94,** 195410 (2016).
97. Behrens, S. H. & Grier, D. G. The charge of glass and silica surfaces. *J. Chem. Phys.* **115,** 6716–6721 (2001).
98. Wang, M. & Revil, A. Electrochemical charge of silica surfaces at high ionic strength in narrow channels. *J. Coll. Interface Sci.* **343,** 381–386 (2010).
99. Manning, G. S. Counterion condensation theory of attraction between like charges in the absence of multivalent counterions. *Eur. Phys. J. E* **34,** 1–18 (2011).
100. Gmür, T. A., Goel, A. & Brown, M. A. Quantifying Specific Ion Effects on the Surface Potential and Charge Density at Silica Nanoparticle–Aqueous Electrolyte Interfaces. *J. Phys. Chem. C* **120,** 16617–16625 (2016).
101. Hocine, S. *et al.* How Ion Condensation Occurs at a Charged Surface: A Molecular Dynamics Investigation of the Stern Layer for Water–Silica Interfaces. *J. Phys. Chem. C* **120,** 963–973 (2016).
102. Wu, X., Lu, W., Ou, W., Caumon, M. & Dubessy, J. Temperature and salinity effects on the Raman scattering cross section of the water OH-stretching vibration band in NaCl aqueous solutions from 0 to 300° C. *J. Raman Spectrosc.* (2016).
103. Bertie, J. E. *et al.* Infrared Intensities of Liquids XX: The Intensity of the OH Stretching Band of Liquid Water Revisited, and the Best Current Values of the Optical Constants of H_2O (l) at 25° C between 15,000 and 1 cm^{-1}. *Meas. Sci. Technol.* **50,** 1047–1057 (1996).

104. Hamrouni, B. & Dhahbi, M. Analytical aspects of silica in saline water—application to desalination of brackish waters. *Desalination* **136,** 225–232 (2001).

105. Rimstidt, J. D. & Barnes, H. L. The kinetics of silica-water reactions. *Geochim. Cosmochim. Acta* **44,** 1683–1699 (1980).

106. Seidel, A., Löbbus, M., Vogelsberger, W. & Sonnefeld, J. The kinetics of dissolution of silica 'Monospher' into water at different concentrations of background electrolyte. *Solid State Ionics* **101,** 713–719 (1997).

107. Plettinck, S., Chou, L. & Wollast, R. Kinetics and mechanisms of dissolution of silica at room temperature and pressure. *Mineral. Mag. A* **58,** 728–729 (1994).

108. Icenhower, J. P. & Dove, P. M. The dissolution kinetics of amorphous silica into sodium chloride solutions : Effects of temperature and ionic strength. *Geochim. Cosmochim. Acta* **64,** 4193–4203 (2000).

109. Dove, P. M. & Nix, C. J. The influence of the alkaline earth cations, magnesium, calcium, and barium on the dissolution kinetics of quartz. *Geochim. Cosmochim. Acta* **61,** 3329–3340 (1997).

110. Wollast, R. & Garrels, R. M. Diffusion coefficient of silica in seawater. *Nature* **229,** 94 (1971).

111. Lopez-Garcia, J. J., Horno, J. & Grosse, C. Poisson-Boltzmann description of the electrical double layer including ion size effects. *Langmuir* **27,** 13970–13974 (2011).

112. Kielland, J. Individual Activity Coefficients of Ions in Aqueous Solutions. *J. Am. Chem. Soc.* **59,** 1675–1678 (1937).